学位論文

# Photoemission Study of the High-Temperature Superconductor $La_{2-y}Sr_yCuO_4$

高温超伝導体 $La_{2-y}Sr_yCuO_4$ の光電子分光

平成10年12月博士（理学）申請

東京大学大学院理学系研究科物理学専攻

井野明洋

学位論文

# Photoemission Study of the High-Temperature Superconductor $La_{2-x}Sr_xCuO_4$

高温超伝導体 $La_{2-x}Sr_xCuO_4$ の光電子分光

平成１０年１２月博士（理学）申請

東京大学大学院理学系研究科物理学専攻

井野明洋

# 論文の内容の要旨

論文題目　Photoemission Study
of the High-Temperature Superconductor $La_{2-x}Sr_xCuO_4$

（高温超伝導体 $La_{2-x}Sr_xCuO_4$の光電子分光）

氏　名　井野明洋

銅酸化物系における高温超伝導機構の解明は現代物性物理学における最も重要な問題の一つである。銅酸化物系は、$CuO_2$面にホールをドープすると反強磁性モット絶縁体から超伝導体、そして常伝導金属へと大きく物性が変わるため、その背後にある電子構造がホール・ドープとともにどのように変化していくのかが、この系の本質を理解する鍵となるだろう。実際に、超伝導体に関しては$Bi_2Sr_2CaCu_2O_{8+y}$系で、ドープされていない反強磁性絶縁体に関しては$Sr_2CuO_2Cl_2$で、バンド分散などが光電子分光で研究されているが、一番興味深い所、つまり反強磁性絶縁体と超伝導体の間や、超伝導体と常伝導金属の間で、電子構造がどう変化しているのかについての直接的な情報はまだ得られていない。一方、近年、低ドープ領域の銅酸化物が、超伝導転移点より少し上の温度でギャップ的な振舞い（スピンギャップ、常伝導ギャップなど）を示すこと、また超伝導転移点より数倍高い温度で帯磁率やホール係数に異常があらわれることなどがわかってきた。これらの現象と、電子構造のホール濃度依存性との関係も重要な問題である。ホール濃度依存性の研究には、数ある銅酸化物系の中でも$La_{2-x}Sr_xCuO_4$系が適している。というのも、$La_{2-x}Sr_xCuO_4$を用いれば反強磁性絶縁体、超伝導体、常伝導金属のすべてを連続的にホール濃度を変えて研究できるからだ。また、最近、$La_{2-x}Sr_xCuO_4$系ではストライプ型のスピン・電荷整列への揺らぎが強いと言われており、他の系と比較すればストライプ揺らぎと超伝導の関係も調べられるだろう。しかし光電子分光では、$La_{2-x}Sr_xCuO_4$の測

定は劈開性や表面の安定性などの面で他の系より難しく今まで後回しにされてきた。従って本研究では、$La_{2-x}Sr_xCuO_4$系に注目し、化学ポテンシャル（フェルミ準位）、運動量について積分した電子状態密度、フェルミ面、エネルギーギャップ、バンド分散などの電子構造のホール濃度依存性を、角度積分型・分解型光電子分光法および逆光電子分光法を用いて徹底的に調べた。

銅酸化物のモット絶縁体にホールをドープしたとき化学ポテンシャルがどのようにシフトするのかは、今まで大きな争点となってきた。化学ポテンシャルのシフトはフェルミ流体論では有効質量の逆数に比例する。チタン酸化物などの通常のモット転移系では金属−絶縁体転移近傍で有効質量が発散するのに対し、$La_{2-x}Sr_xCuO_4$では電子比熱係数の測定から転移点近傍に向かって有効質量が減少することが示されている。光電子分光を用いると、内殻準位のスペクトルのシフトから化学ポテンシャルのシフトを見積もることができる。X線光電子分光スペクトルを測定・解析した結果、化学ポテンシャルのホール・ドープによるシフトは、図1のように、高ドープ領域（$x > 0.15$）では $\partial\mu/\partial x \sim -1.5$ eV であるが、低ドープ領域（$x < 0.15$）では非常に遅くなっている（$|\partial\mu/\partial x| < 0.2$ eV）ことがわかった。高ドープ領域においては、化学ポテンシャルのシフトと比熱係数の振る舞いは、ランダウパラメーターが $F^0_s \sim 7 \pm 2$ 程度の電子間相互作用の強いフェルミ流体のものとして解釈できるが、低ドープ領域では同様のフェルミ流体的解釈は破綻する。ホール濃度 $x$ が減るにつれて化学ポテンシャルのシフトと比熱係数が同時に抑えられる（$x \to 0$ のとき $\partial\mu/\partial x \to 0$ かつ $\gamma \to 0$）という非フェルミ流体的な現象は、化学ポテンシャルの近傍でギャップが開いているとすれば可能であると考えた。低ドープ領域で化学ポテンシャルがシフトしない理由としては、近年盛んに議論されているように、ホールが動的な揺らぎとしてストライプ状に反強磁性領域から分離している可能性が考えられる。

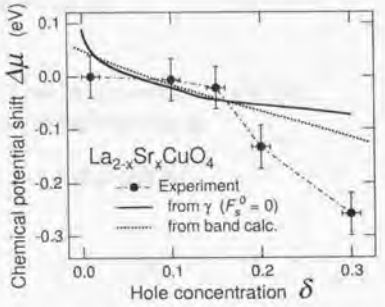


図1　$La_{2-x}Sr_xCuO_4$ の化学ポテンシャルのホール濃度依存性

高分解能光電子分光と逆光電子分光を用いて、$La_{2-x}Sr_xCuO_4$の角度積分型スペクトルを、ホールを多くドープした常伝導金属（$x = 0.30$）から反強磁性絶縁体（$x = 0$）まで測定した。電荷移動ギャップ（～1.5 eV）程度のエネルギー・スケールでは、ホールをドープすることによってスペクトルの重みが上部ハバード・バンドから、+1 eV を中心として電荷移動ギャップ全体の領域に移動することがわかった。図2に示すように、フェルミ準位近傍では ～0.1 eV のエネルギー・スケールでスペクトルの強度が擬ギャップ的に抑えられている。これを「高エネルギー擬ギャップ」または「弱い擬ギャップ」と呼ぶ。金属−絶縁体転移に向かってホール濃度 $x$ が減ると、フェルミ準位上でのスペクトル状態密度が徐々に減少するが、そのホール濃度依存性は電子比熱係数のホール濃度依存性とよく合うことがわかった。また、擬ギャップのエネルギー幅 $\Delta_{PG}$ は $x$ が減るにつれて大きくなり、帯磁率やホール係数に見られる特徴的な温度が反強磁性絶縁体（$x = 0$）に向かって大きくなるのとよく似たホール濃度依存性を示す。擬ギャップ的なスペクトルはコヒーレンス温度が低いことも示唆しており、低ドープ領域での伝導特性はインコヒーレントな金属のものと考えられうることを提唱する。角度積分型スペクトルで観測される擬ギャップは、その大きさ（～0.1 eV）やホール濃度依存性から、銅スピン間の反強磁性相関に由来することが示唆される。

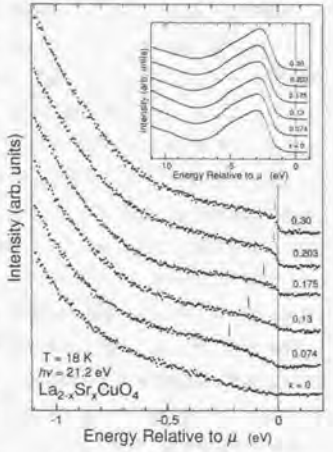


図2　$La_{2-x}Sr_xCuO_4$ の光電子分光スペクトルにおける擬ギャップ

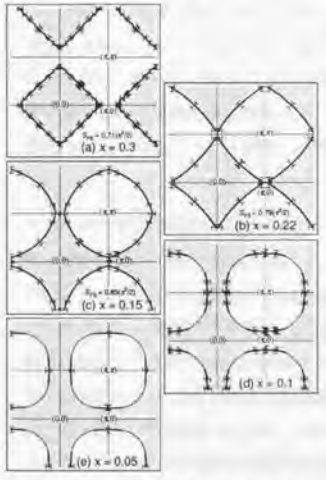


図3　$La_{2-x}Sr_xCuO_4$ のフェルミ面のホール濃度依存性

角度分解型光電子分光を用いて、$La_{2-x}Sr_xCuO_4$のフェルミ面、フェルミ面上のエネルギーギャップ、フェルミ準位近傍の占有状態のバンドの分散、およびそれらのドーピング依存性を $0.03 \leq x \leq 0.30$ という広いホール濃度領域で調べた。その結果、図3に示すように、最適および低ドープ領域（$x \leq 0.15$）では、他の銅酸化物と同様に $\mathbf{k} = (\pi,\pi)$ を中心とするホール型のフェルミ面となっているが、多くのホールをドープすると（$x = 0.30$）、$\mathbf{k} = (0,0)$ を中心とする電子型のフェルミ面へと変化することがわかった。一方、ホール濃度が減るにつれて、11 K での超伝導ギャップ（$x = 0.15$ で $2\Delta_{SC} = 18 \pm 6$ meV）は一様に大きくなり続け、$x = 0.05$ で観測された常伝導ギャップ（$2\Delta_{NG} = 48 \pm 9$ meV、「低エネルギー擬ギャップ」または「強い擬ギャップ」とも呼ぶ）へと連続的に発展しているように見える。驚くべきことには、最適ドープ領域（$x = 0.15$）から

低ドープ領域 ($x$ = 0.10) に行くと、運動量空間でブリルアン域の斜め方向〔(0,0)−(π,π)方向〕の準粒子バンドおよびフェルミ面やが消えてしまう。これは、斜め方向で鋭い準粒子ピークが見られる $Bi_2Sr_2CaCu_2O_{8+y}$系のスペクトルと極めて対照的である。さらに、超伝導−絶縁体転移近傍 ($x$~0.05) では、図4に示すように角度分解スペクトルに二つの構造が共存しており、ホール・ドープによって二つの構造の間でスペクトルの重みが移動するという現象を見い出した。これは、転移点近傍でホール濃度が微視的な大きさで不均一に揺らいでいることを示唆していると考えられる。低ドープ領域で見られた $La_{2-x}Sr_xCuO_4$系と $Bi_2Sr_2CaCu_2O_{8+y}$系のスペクトルの違いは、$La_{2-x}Sr_xCuO_4$系で特に強いと言われる動的なストライプ型の揺らぎと関連しているように見える。電荷ストライプ間の反強磁性領域にホールが少ないため、縦や横のストライプと同じ向きの運動量の電子状態では金属的な準粒子ピークを見せるのに対して、ストライプを横切る斜め方向の運動量をもつ電子状態は伝搬が抑えられるものと考えられる。ホールをドープするとともに、絶縁体でホールが微視的に分離し縦と横に並んで反強磁性領域の境界をなしている状態から、ストライプ揺らぎのある超伝導体へと連続的に発展していくという描像が実験結果より示唆される。

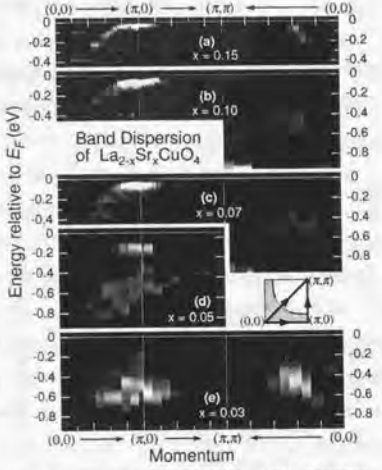


図4 $La_{2-x}Sr_xCuO_4$の超伝導−絶縁体転移近傍でのバンド構造のホール濃度依存性

以上の結果を合わせると、銅酸化物系の電子構造は、低ドープ領域で増大する二つのエネルギー・スケール、即ち高エネルギー擬ギャップ ($\Delta_{PG}$ ~ 100 meV) と超・常伝導ギャップ ($\Delta_{SC}$, $\Delta_{NG}$ ~ 10 meV) によって特徴づけられることがわかった。本実験から示唆される描像では、ホールをドープするとともにともに$La_{2-x}Sr_xCuO_4$ 系は、反強磁性絶縁体 ($x$ ~ 0) から、微視的な大きさで相分離した絶縁体 ($x \leq 0.05$)、擬ギャップ構造と動的なストライプ揺らぎの強い超伝導体 ($0.05 < x \leq 1/8$)、比較的フェルミ流体的な超伝導金属 ($0.2 \leq x < 0.27$)、そしてフェルミ流体的な常伝導金属 ($x$ ~ 0.3) へと変化する。$La_{2-x}Sr_xCuO_4$系の光電子分光によって、多くの新しい情報を得ることができた。高温超伝導機構の理解のためには、さらに$La_{2-x}Sr_xCuO_4$系を研究するとともに、多様な銅酸化物系を系統的に光電子分光で研究する必要があるだろう。

# Photoemission Study of the High-Temperature Superconductor $La_{2-x}Sr_xCuO_4$

THESIS

Akihiro Ino

*Department of Physics, University of Tokyo*

January 1999

# Contents

# Chapter 1

# Introduction

Since the discovery of the high critical temperature (high-$T_c$) superconductivity in cuprates [1], understanding the nature of these systems has been the most challenging issue in condensed matter physics. The cuprate systems show not only high-$T_c$ superconductivity but also various unusual behaviors in the vicinity of the filling-control Mott metal-insulator transition [2-4]. Underlying those curious behaviors are strong electron correlations. However, due to the difficulties inherent in the many-body character of the electron correlations, much remain unclarified for the superconductivity in cuprates in spite of the long-standing research effort.

The cuprate systems drastically change their behaviors depending on the electron density of two-dimensional $CuO_2$ planes, which is the stage of the high-$T_c$ superconductivity and related low-energy physics. The basic behaviors of the $CuO_2$ plane are common to all the cuprate superconductors. When the $CuO_2$ plane has half-filled $d_{x^2-y^2}$ orbitals as in $La_2CuO_4$, the system is an antiferromagnetic Mott insulator because of the strong on-site Coulomb repulsion between electrons [2-4]. Removing electrons from the insulating $CuO_2$ plane may be regarded as hole doping and is performed by, e.g., replacing part of $La^{3+}$ by $Sr^{2+}$ in $La_{2-x}Sr_xCuO_4$ (LSCO) system. Upon hole doping, the three-dimensional antiferromagnetic order is rapidly destroyed at a hole concentration $\delta = x \simeq 0.02$, and then a transition from the insulator to the superconductor takes place at $x \sim 0.05$. With further hole doping, the superconducting critical temperature ($T_c$) increases up to $\sim 40$ K at the optimum doping of $x \simeq 0.15$, and then $T_c$ decreases and disappears around $x \simeq 0.27$. While overdoped ($x \gtrsim 0.2$) cuprates behave like a relatively conventional metal above $T_c$, underdoped ($x < 0.15$) cuprates in the normal state show behaviors strongly deviated from the standard Fermi-liquid behaviors and thus are commonly called anomalous metals.

Therefore, it is necessary to know the electronic structure of the $CuO_2$ plane to understand the cuprate systems. Photoemission spectroscopy (PES) is a powerful tool to probe the electronic structure directly. Recent development of the PES method has enabled us to observe fine structures near the chemical potential ($\mu$). For the undoped insulating cuprate, a charge-transfer (CT) gap of $\sim$ 1.5 eV [5, 6] is present at $\mu$ and separates the Cu $3d$ band into upper and lower Hubbard bands (LHB and UHB). Practically the Zhang-Rice singlet band plays the role of an effective LHB [7, 8] and its dispersion has been observed for an undoped cuprate $Sr_2CuO_2Cl_2$ by angle-resolved photoemission spectroscopy (ARPES) [9-11]. On the other hand, since the hole-doped superconductor is metallic above $T_c$, a finite density of state (DOS) is present around $\mu$. Indeed, ARPES studies on the cuprate superconductors such as $Bi_2Sr_2CaCu_2O_{8+y}$ (Bi2212) have been performed extensively [12-35] and revealed the dispersion of a quasiparticle band crossing the chemical potential $\mu$ [14-23].

However, it has been controversial how the electronic structure evolves with hole doping from the undoped antiferromagnetic insulator to the superconductor and then to the normal metal. On the one hand, it has been claimed that, upon hole doping, the chemical potential jumps to the top of the LHB and the spectral weight just above $\mu$ increases [8, 36]. On the other hand, it has been also claimed that, upon hole doping, the chemical potential is pinned within the CT gap because new states emerge in the CT gap and that the doping-induced states evolve into the quasiparticle band responsible for the superconductivity [37].

A "spin-gap" behavior has been observed somewhat above $T_c$ in underdoped $YBa_2Cu_3O_{7-y}$ (YBCO) by nuclear magnetic resonance (NMR) [38, 39]. Also a "normal-state gap" behavior in underdoped Bi2212 has been revealed by ARPES, that is, the energy gap remains open somewhat above $T_c$ [29-33]. The magnitude of the normal-state gap is of the same order as the superconducting gap. On the other hand, underdoped cuprates have characteristic temperatures which are considerably *higher* than $T_c$ in the uniform magnetic susceptibility [40], the electronic specific heat [41], the Hall coefficient [42, 43] and the electrical resistivity [40]. All these characteristic temperatures show similar behaviors in the LSCO: they increase from $\sim$ 300 K at the optimal doping $x \sim 0.15$ to $\sim$ 600 K at $x \sim 0.1$ for the LSCO system, suggesting a pseudogap-type electronic structure. In addition to the energy of the superconducting gap, the energies of those pseudogaps and their doping dependences should be key issues to understand the cuprate systems and the underlying strong electron correlations.



In order to study the doping dependence of the electronic structure systematically, the LSCO system is suitable among the family of high-$T_c$ cuprate superconductors for several reasons. First, LSCO has a simple crystal structure with single $CuO_2$ layers. It has no Cu-O chains unlike YBCO nor complicated structural modulation of the block layers unlike Bi2212. Second, the hole concentration in the $CuO_2$ plane can be controlled in a wide range and uniquely determined by the Sr concentration $x$ (and the small oxygen non-stoichiometry). One can therefore investigate the doping dependence continuously from the undoped insulator ($x = 0$) to the heavily overdoped limit ($x \sim 0.3$) in the same system. Indeed the doping dependences of transport and thermodynamic properties have been extensively studied for the LSCO system [40, 42-47].

Recently, it has been widely discussed that the LSCO system is particularly close to the instability towards the spin-charge order in a stripe form [48, 49], suggested by incommensurate peaks in the inelastic neutron scattering (INS) [50], while such a observation has not been reported for Bi2212. Therefore, in order to clarify the impact of the stripe fluctuations, it is important to investigate what is common and what is different between the PES spectra of LSCO and Bi2212 systems.

Therefore, the present study focuses on the LSCO system among many cuprate superconductors. So far, the PES study of LSCO have been hindered in spite of its importance because of the difficulty in cleaving and the surface instabilities compared to the extremely stable surfaces of Bi2212 under an ultra high vacuum. In the present study, the difficulties in LSCO have been overcome owing to the high quality of samples and the careful experiments.

The present PES work is devoted to clarify how the electronic structure evolves with hole doping in the $La_{2-x}Sr_xCuO_4$ system from the undoped antiferromagnetic insulator ($x = 0$) through the superconductor ($0.05 \lesssim x \lesssim 0.27$) to the non-superconducting metal ($x = 0.3$). As backgrounds for the present study, other experimental results on the $La_{2-x}Sr_xCuO_4$ system and the techniques of photoemission spectroscopy will be briefly reviewed in Chapter 2. Among the present experimental results, the chemical potential shift, momentum-integrated and momentum-resolved electronic structures will be focused on in Chapters 3, 4, and 5, respectively. Unifying those results, perspective views and concluding remarks will be given in Chapter 6.

# Chapter 2

# Backgrounds

## 2.1 High-$T_c$ cuprates and $La_{2-x}Sr_xCuO_4$ system

Since the high-$T_c$ cuprates including the $La_{2-x}Sr_xCuO_4$ (LSCO) system have been extensively studied so far, some basic properties have already been revealed. In this thesis, the results of other experimental and theoretical studies will be frequently referred. Therefore, the progress in the field of high-$T_c$ is briefly reviewed in this section.

### 2.1.1 Crystal structure

All the cuprate superconductors have conductive $CuO_2$ planes separated by block layers as shown in Fig. 2.1(a). As an example, the crystal structure of $La_{2-x}Sr_xCuO_4$ (LSCO) system is shown in Fig. 2.1(b). For LSCO, the block layer is the La-O double planes. The block layers play the role of a charge reservoir. Replacing part of $La^{3+}$ by $Sr^{2+}$, electrons are withdrawn from the $CuO_2$ planes. Since the La-O blocks are ionic, they have no contributions to the low-energy electronic states ($\lesssim 1$ eV). On the other hand, the $CuO_2$ planes have an energy band around the chemical potential $\mu$ (Fermi level $E_F$) and thus dominate the low energy physics ($\lesssim 1$ eV) of the cuprate systems. The two-dimensional $CuO_2$ planes have been believed to be the stage of the superconductivity.

The simpleness of the crystal structure of LSCO is an advantage for studying the electronic structure of the $CuO_2$ plane itself. LSCO has single $CuO_2$ planes, while $Bi_2Sr_2CaCu_2O_{8+y}$ (Bi2212) and $YBa_2Cu_3O_{7-y}$ (YBCO)

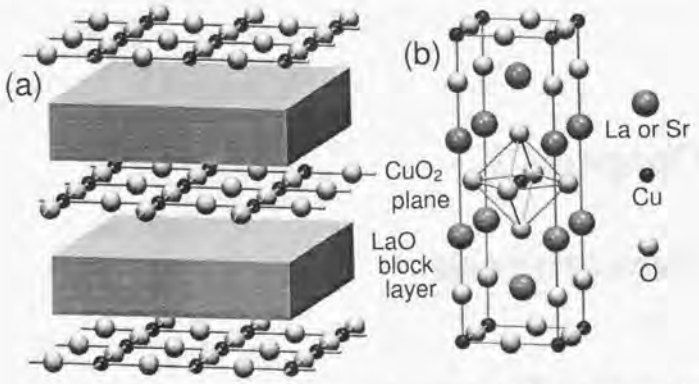


Figure 2.1: (a) Two-dimensional $CuO_2$ planes separated by block layers. All the cuprate superconductors contain such $CuO_2$ planes. (b) Crystal structure of $La_{2-x}Sr_xCuO_4$.

systems have double $CuO_2$ planes. The block layer of LSCO has neither the Cu-O chains which affect the $CuO_2$ plane of YBCO, nor the complicated structural modulation present in the block layer of Bi2212.

### 2.1.2 Phase diagram

Depending on the electron density in the $CuO_2$ plane, the physical properties of the cuprates change drastically. The phase diagram of $La_{2-x}Sr_xCuO_4$ is shown in Fig. 2.2. In the parent compound $La_2CuO_4$ ($x = 0$), owing to the valences of $La^{3+}$ and $O^{2-}$, the valence of Cu is +2 within the ionic picture. Since $Cu^{2+}$ has nine electrons (or one hole) in the Cu $3d$ band ($d^9$ configuration), the band with the highest energy is half-filled. Contrary to prediction of the band theory, $La_2CuO_4$ with the half-filled band is an antiferromagnetic Mott insulator with Néel temperature $T_N \simeq 300$ K because of strong electron interactions. Removing electrons from the insulating $CuO_2$ planes may be regarded as hole doping. Upon hole doping, the three-dimensional antiferromagnetic order disappears by $\delta = x \simeq 0.02$, while local magnetic field remain present even for $x > 0.02$ at low temperatures ($\lesssim 10$ K) [51], which has been considered as something like a "spin-glass" (SG) phase. At $x \sim 0.05$, the system undergoes a transition from the insulator to the superconductor. With further hole doping, $T_c$ increases up to $\sim 40$ K at the



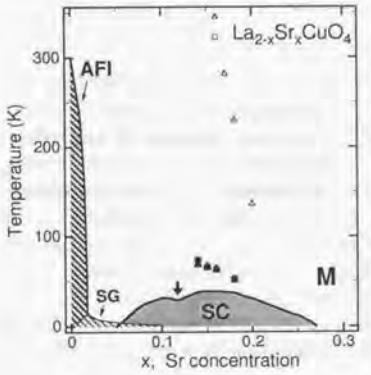


Figure 2.2: Phase diagram of $La_{2-x}Sr_xCuO_4$. AFI: antiferromagnetic insulator [51]. SG: so-called spin-glass [51]. SC: superconductor [47]. M: metal. Filled and open symbols denote the crossover temperatures in the electrical resistivity $\rho(T)$ (circles) and magnetic susceptibility $\chi(T)$ (triangles) as explained in Sec. 2.1.4. The hole concentration of the $CuO_2$ plane $\delta$ is almost equal to the Sr substitution $x$, $\delta \simeq x$.

optimum doping level of $x \simeq 0.15$, and then $T_c$ decreases and disappears around $x \simeq 0.27$.

While the $T_c$ of different cuprate systems have different maxima $T_c^{max}$, the $T_c$ scaled with $T_c^{max}$ roughly follows an universal curve as a function of the hole concentration $\delta$.

### 2.1.3 Electronic structure

In the $CuO_2$ plane, the $d_{x^2-y^2}$ band originated from Cu has the highest energy among the five $d$ bands as shown in Fig. 2.3, because the Cu $d_{x^2-y^2}$ orbital well hybridizes with oxygen $p$ orbitals through the in-plane Cu-O bonds which have shorter length than out-of-plane Cu-O bonds [Fig. 2.1(a)]. Therefore, in the parent compound $La_2CuO_4$ with nine $d$ electrons (or one $d$ hole), the $d_{x^2-y^2}$ band is half-filled and carries 1/2 spin. Since the on-site Coulomb repulsion $U$ between $d_{x^2-y^2}$ electrons is stronger than the band width $W$ (the kinetic energy of the electrons) in the cuprates, the electrons tends to avoid the double occupancy of the $d_{x^2-y^2}$ orbital and, at half-filling, the electrons are localized as a Mott insulator [2-4]. For the $CuO_2$ plane, the minimum charge excitation energy is not the energy $U$ for the electron transfer between the half-filled Cu $3d_{x^2-y^2}$ orbitals, but the energy $\Delta_{CT}$ for the charge transfer between the Cu $3d_{x^2-y^2}$ band and the O $2p$ bands hybridized with the $d_{x^2-y^2}$ band. The three bands in the $CuO_2$ plane, $d_{x^2-y^2}$, $p_x$ and $p_y$, and their energies relative to the chemical potential $\mu$ are schematically illustrated in Figs. 2.4(a) and (c), respectively. The Cu $3d_{x^2-y^2}$ band is split into the upper and lower Hubbard bands (UHB and LHB) by Coulomb repulsion $U$

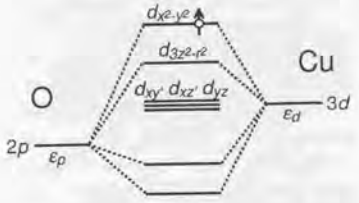


Figure 2.3: Schematic diagram for the energies of Cu $3d$ and O $2p$ orbitals in the cuprates. In $La_2CuO_4$, the Cu atom is surrounded by an oxygen octahedron elongated along the $z$-direction [Fig. 2.1(a)].

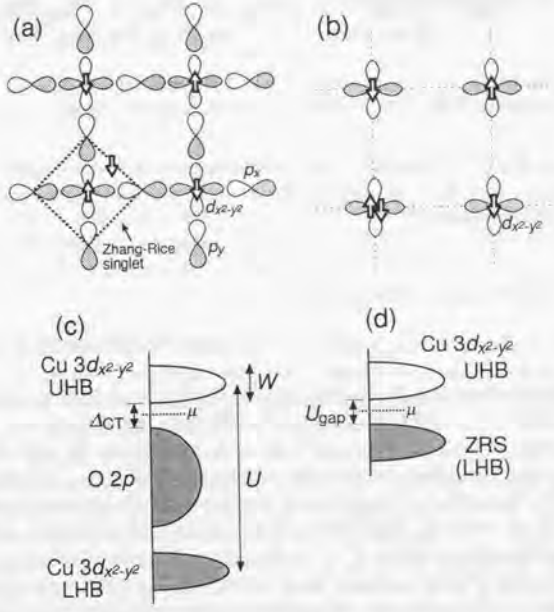


Figure 2.4: Schematic pictures for the electronic orbitals (a)(b) and the electronic structure (c)(d) of the $CuO_2$ plane. Three bands, Cu $3d_{x^2-y^2}$, O $2p_x$ and $2p_y$, are considered in (a) and (c). Only the $d_{x^2-y^2}$ band at the Cu site is considered in (b) and (d).



and the O $2p$ bands are located between them and separated from UHB by the charge-transfer gap $\Delta_{CT}$, whose magnitude is about $\Delta_{CT} \sim 1.5$ eV for $La_2CuO_4$ according to the optical conductivity studies [5, 6].

As for the low-energy physics ($\lesssim \Delta_{CT}$) in the $CuO_2$ plane, the three-band picture [Figs. 2.4(a) and (c)] may be further simplified. When a hole is introduced into the O $2p$ band in addition to the one $d$ hole, a local singlet state called Zhang-Rice singlet (ZRS) has the lowest energy for the $p$ hole [7, 8]. As shown in Fig. 2.4(a), the $p$ hole in the ZRS state surrounds the Cu site and carries another 1/2 spin of the direction opposite to the spin of the $d$ hole. Thus one may interpret the UHB and the ZRS band as the effective UHB and LHB split from a band of the $d_{x^2-y^2}$ symmetry at the Cu site by the effective Coulomb repulsion $U_{gap} = \Delta_{CT}$ as illustrated in Figs. 2.4(b) and (d). Hereafter, most of discussions will be based on the one-band picture [Figs. 2.4(b) and (d)].

Suppose that the Coulomb interaction $U$ is neglected and that the dispersion of the $d_{x^2-y^2}$ band is given by a simple three-band tight-binding model of the $CuO_2$ plane [Fig. 2.4(a)] with parameters $\varepsilon_d - \varepsilon_p$, $t_{d-p}$ and $t_{p-p}$. The calculated dispersion and Fermi surface are shown in the left and right panels of Fig. 2.5(a) [52], respectively. In the Brillouin zone of the $CuO_2$ plane, the $(0,0) - (\pi,0)$ direction is the direction parallel to Cu-O bond. The metallic band at half-filling has a square Fermi surface and a van-Hove singularity at $(\pi,0)$.

When the Coulomb interaction is turned on, the $d_{x^2-y^2}$ band is split into the UHB and LHB (ZRS band) as shown in Fig. 2.4(d) and the Fermi surface disappears. The dispersion of the LHB in the undoped insulating $CuO_2$ plane has been observed for $Sr_2CuO_2Cl_2$ by angle-resolved photoemission spectroscopy (ARPES) as shown in Fig. 2.5(b) [9-11].

With hole doping, the cuprates turn from the antiferromagnetic Mott insulator to the superconductor showing metallic behaviors above $T_c$ (Fig. 2.2). Thus the density of states (DOS) should be finite around $\mu$. Indeed, the quasiparticle band crossing $\mu$ has been extensively studied for the hole-doped superconductor $Bi_2Sr_2CaCu_2O_{8+y}$ (Bi2212) by ARPES. As for the Bi2212 system, the dispersion of the quasiparticle band crossing $\mu$ and the Fermi surface have been established as shown in Fig. 2.5(c), which is an ARPES result for a nearly optimally doped sample [17]. With hole doping, the qualitative features of the band dispersion approach those for the non-interacting band, even though the band effective mass may be renormalized due to the Coulomb interaction $U$. Comparing the ARPES result with the non-interacting band in Fig. 2.5(a), the flat band at the van-Hove singularity $(\pi,0)$ is consider-

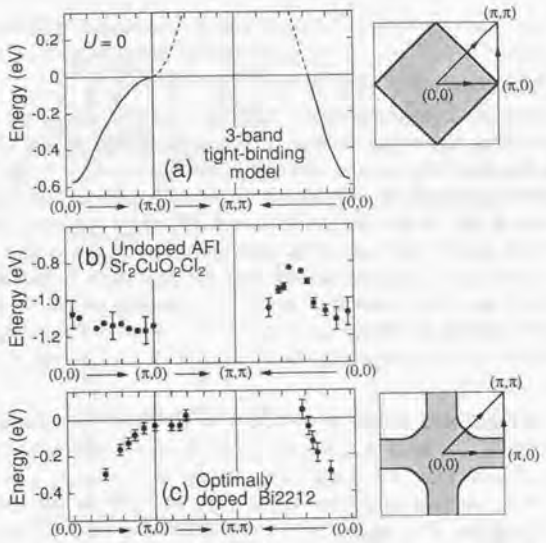


Figure 2.5: Band dispersions (left) and Fermi surfaces (right) of the $CuO_2$ plane. (a) Dispersion calculated for a simple three-band tight-binding model by Markiewicz [52]. The parameters are $\varepsilon_d - \varepsilon_p = 0.244$ eV, $t_{d-p} = 0.347$ eV and $t_{p-p} = 0.25$ eV. (b) ARPES result for the undoped $CuO_2$ plane of $Sr_2CuO_2Cl_2$ by Wells *et al.* [9]. (c) ARPES result for nearly optimally doped $Bi_2Sr_2CaCu_2O_{8+y}$ ($T_c = 85$ K) in the normal state by Marshall *et al.* [17].

ably extended as commonly called the "$(\pi, 0)$ flat band" [15, 17-21]. When the temperature is lowered below $T_c$, the superconducting gap with $d_{x^2-y^2}$ symmetry is opened on the Fermi surface around $(\pi, 0)$.

Nevertheless, it has not yet been clarified how the electronic structure evolves with hole doping, especially between the undoped antiferromagnetic insulator (AFI) and the superconductor, because the dispersions for the AFI and the superconductor are so different as shown in Figs. 2.5(b) and (c), respectively. So far two contrasting pictures have been proposed for this problem as shown in Fig. 2.6. In one picture [Fig. 2.6(b)], the chemical potential $\mu$ jumps upon hole doping from the charge-transfer gap region to the top of the LHB and the spectral weight is transferred from the UHB to the top of the LHB above $\mu$ [8, 36]. In the other picture [Fig. 2.6(c)], the



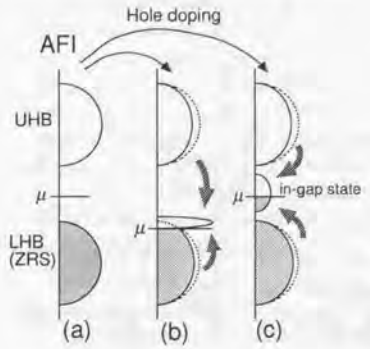


Figure 2.6: Two contrasting pictures of how the electronic structure evolves with hole doping from the Mott antiferromagnetic insulator (AFI) to the hole-doped metal.

chemical potential is fixed within the charge-transfer gap region of the parent insulator, and the spectral weight is transferred with hole doping from the UHB and LHB into around the chemical potential [37].

Therefore, in the following chapters, we will focus on the doping dependences of the chemical potential, the momentum-integrated DOS, the band dispersion and the Fermi surface.

### 2.1.4 Unusual behaviors of underdoped cuprates

The magnetic and transport properties of the high-$T_c$ cuprates have been extensively studied at temperatures much lower than the charge-transfer gap energy ($\ll \Delta_{CT} \sim 1.5$ eV). In a Fermi liquid, the magnetic susceptibility $\chi(T)$ and the Hall coefficient $R_H(T)$ are temperature independent, and the electrical resistivity $\rho(T)$ grows as $\sim T^2$ with increasing temperature $T$. However, as the cuprate approaches the AFI from the metallic side ($x \to 0$ in Fig. 2.2), the normal-state behaviors strongly deviate from those of the conventional Fermi liquid. As shown in Fig. 2.7, the underdoped LSCO shows characteristic temperatures: $T_\chi$ below which $\chi(T)$ decreases from the maximum value, $T_H$ below which $1/R_H(T)$ is reduced from the temperature-independent value, and $T_\rho$ below which $\rho(T)$ deviates downwards from the linear behavior extrapolated from the high-temperature data. These characteristic temperature have a similar value, which is much higher than $T_c$ ($T_c \ll T_\chi \ll \Delta_{CT}/k_B$). As $x$ decreases towards the AFI, the characteristic temperatures increase, namely, the anomalous metallic region grows wider as indicated by open symbols in Fig. 2.8.

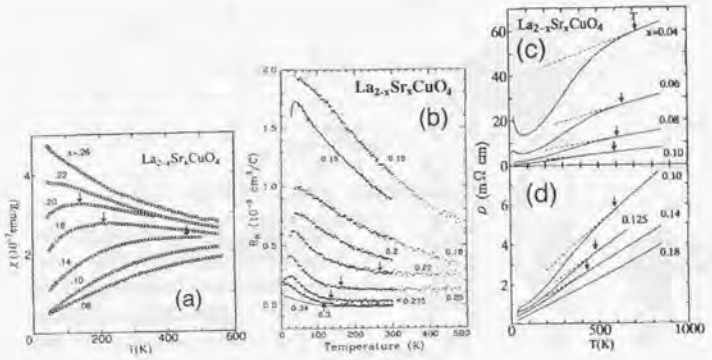


Figure 2.7: Temperature dependences of (a) the magnetic susceptibility $\chi(T)$ [40], (b) the Hall coefficient $R_H(T)$ [42] and (c) (d) the electrical resistivity $\rho(T)$ [40] of $La_{2-x}Sr_xCuO_4$, showing characteristic temperatures much higher than $T_c$.

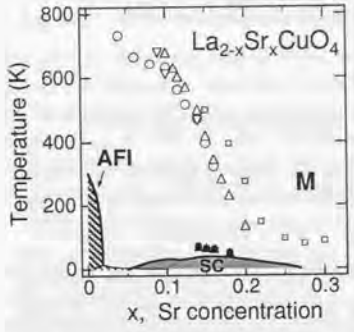


Figure 2.8: Characteristic temperatures in the magnetic susceptibility $T_\chi$ ($\triangle$ [40], $\triangledown$ [53]), the Hall coefficient $T_H$ ($\square$ [42]), and the electrical resistivity $T_\rho$ ($\bigcirc$ [40]), superimposed on the phase diagram of Fig. 2.2. Closed symbols denote the temperatures below which the electrical resistivity ($\bullet$) and the magnetic susceptibility ($\blacktriangle$) are slightly reduced from the $T$-linear behaviors [54].

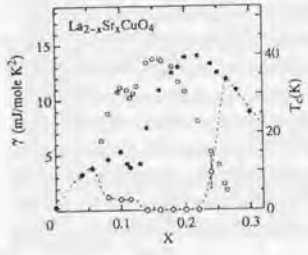


Figure 2.9: Low-temperature electronic specific heat coefficient of $La_{2-x}Sr_xCuO_4$ in the superconducting state $\gamma_s$ (open diamonds) and the normal state $\gamma_n$ (filled circles) by Momono *et al* [47]. The normal-state data have been deduced by breaking the superconductivity by Zn-substitution at low temperatures. Open circles denote the $T_c$ of $La_{2-x}Sr_xCuO_4$.



Also the normal-state electronic specific heat coefficient $\gamma_n$ shows unusual doping dependence for the cuprate systems. In an usual Fermi liquid, the conduction-electron mass $m^* \propto \gamma$ is expected to diverge towards the filling-control metal-insulator boundary as observed for a three-dimensional Mott system $La_{1-x}Sr_xTiO_3$. On the other hand, while the $\gamma_n$ of LSCO increases as $x$ decreases in the overdoped region ($x \gtrsim 0.2$), $\gamma_n$ turns to decrease with further decreasing $x$ in $x < 0.2$ [45-47] as shown in Fig. 2.9, suggesting that $m^* \to 0$ as $x \to 0$. The suppression of $\gamma_n$ indicates that the quasiparticle DOS at the chemical potential $N^*(\mu) \propto m^*$ is suppressed even when the superconductivity is broken.

Particularly remarkable anomalies are observed at further lower temperatures near $T_c$ for the underdoped cuprates. A striking evidence is the "spin-gap" behavior observed by nuclear magnetic resonance (NMR) for underdoped $YBa_2Cu_3O_{7-y}$ (YBCO) [38, 39]. Figure 2.10(a) [55] shows that the spin-lattice relaxation rate $1/T_1T$ deviates downwards from the Curie-Weiss law at a temperature somewhat above $T_c$. Another obvious anomaly is the "normal-state gap" behavior observed in the ARPES spectra of underdoped Bi2212 [29-33]. As shown in Fig. 2.10(b) [29], while the superconducting

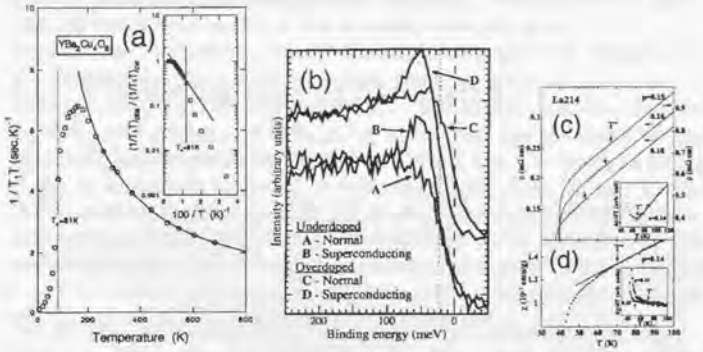


Figure 2.10: (a) "Spin-gap" behavior observed in the NMR spin-lattice relaxation rate $1/T_1T$ for underdoped $YBa_2Cu_3O_{7-y}$ (YBCO) by Yasuoka *et al.* [55]. (b) "Normal-state gap" behavior observed in the ARPES spectra for underdoped $Bi_2Sr_2CaCu_2O_{8+y}$ by Loeser *et al.* [29] (c) The reduction in the electrical resistivity $\rho(T)$ and the uniform magnetic susceptibility $\chi(T)$ at temperatures somewhat above $T_c$ for $La_{2-x}Sr_xCuO_4$, measured by Nakano *et al.* [54].

gap on the Fermi surface near $(\pi, 0)$ disappears above $T_c$ for an overdoped sample, the energy gap survives even at a temperature in the normal state for the underdoped sample. As for LSCO, somehow the spin-gap behavior is obscured in the NMR results [56]. However, also for LSCO, it has been reported that, below a temperature somewhat above $T_c$, the electrical resistivity $\rho(T)$ and the uniform magnetic susceptibility $\chi(T)$ slightly deviate downwards from the $T$-linear extrapolation from higher temperatures as in the Bi2212 system as shown in Fig. 2.10(c) [54]. All these anomalies have similar crossover temperatures, which decrease as $x$ increases and appear to merge with $T_c$ in the overdoped region ($x \gtrsim 0.2$) as shown by closed symbols in Fig. 2.2.

### 2.1.5 1/8 problem in $La_{2-x}Sr_xCuO_4$ system

It has been known as the "1/8 problem" that the $T_c$ of $La_{2-x}Sr_xCuO_4$ (LSCO) is slightly suppressed around the hole concentration $\delta \simeq x = 1/8$ as indicated by a thick arrow in Fig. 2.2. The suppression around $x = 1/8$ is more prominent in some related materials, e.g., $La_{2-x}Ba_xCuO_4$ [57] and $La_{1.6-x}Nd_{0.4}Sr_xCuO_4$ [58]. Meanwhile, in inelastic neutron scattering (INS) experiments, it has been observed that the $La_{2-x}Sr_xCuO_4$ system has dynamical incommensurate spin fluctuations as shown in Figs. 2.11(a) and (b) [59, 60]. Recently, the corresponding static spin-charge order has been reported for $La_{1.6-x}Nd_{0.4}Sr_xCuO_4$ by elastic neutron diffraction experiments [50]. It has been proposed that the static spin-charge order in $La_{1.6-x}Nd_{0.4}Sr_xCuO_4$ and the dynamical spin fluctuations in $La_{2-x}Sr_xCuO_4$ equally have a form of stripes as shown in Fig. 2.11(c) in analogy with the stripe-type spin-charge order in $La_{2-x}Sr_xNiO_4$. The suppression of $T_c$ may be understood as a natural result of the spin-charge order of Fig. 2.11(c), which is stabilized at the hole concentration of $\delta = 1/8$. The idea of the stripe fluctuations has also been supported by extended x-ray absorption fine structure (EXAFS) studies [61] and extensively discussed theoretically [48, 49, 62].

On the other hand, the incommensurate spin fluctuations have not yet been reported for $Bi_2Sr_2CaCu_2O_{8+y}$ (Bi2212) so far and the $T_c$ of Bi2212 is a smooth function of the hole concentration, while a weak 1/8 anomaly appears in the $T_c$ of Zn-substituted Bi2212 [63]. The stipe fluctuations of LSCO appear to be much stronger than those of Bi2212. Therefore, one may investigate the impact of stripe fluctuations by thoroughly comparing the LSCO and Bi2212 systems.



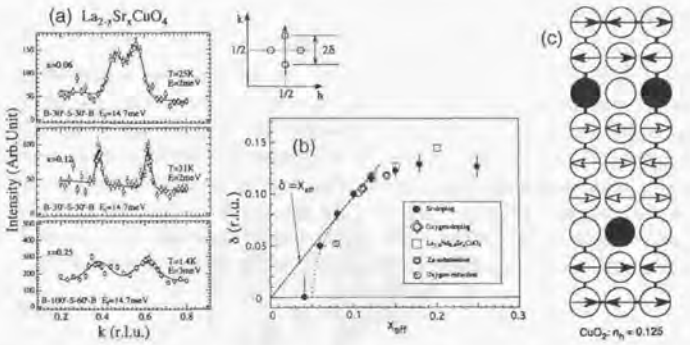


Figure 2.11: (a) Inelastic neutron scattering (INS) spectra of $La_{2-x}Sr_xCuO_4$, showing incommensurate spin fluctuations around $(\pi, \pi)$ [60] and (b) doping dependence of the incommensurability of the spin fluctuation, taken from the splitting of the observed incommensurate peaks by Yamada *et al.* [60]. The path along which the INS spectra were taken in the momentum space is shown in the middle top panel. (c) Spin-charge order in a stripe form proposed for the cuprates by Tranquada *et al.* [50]. Arrows denote 1/2-spins and filled circles denote holes in the Cu site.

## 2.2 Photoemission spectroscopy

### 2.2.1 Photoemission spectroscopy

Photoemission spectroscopy (PES) is a powerful tool to investigate the electronic structure of materials directly. Photoemission is the phenomenon that a material irradiated by light emits electrons. Knowing the kinetic energy $E^{\rm v}_{\rm kin}$ of the emitted electron in the vacuum, one can deduce how strong the electron was bound to the material. Owing to the energy conservation law,

$$E^{\rm v}_{\rm kin} = h\nu - E_{\rm B} - \Phi, \tag{2.1}$$

where $h\nu$ is the energy of the incident photons, $E_{\rm B}$ is the binding energy relative to the Fermi level $E_{\rm F}$ (chemical potential $\mu$) and $\Phi$ is a work function of the material under study. The work function $\Phi$ is the energy required for the electron to escape from the solid through the surface and to reach the vacuum level $E_{\rm vac}$, that is, $\Phi = E_{\rm vac} - E_{\rm F}$. In practical PES experiments, since both the sample and the electron energy analyzer are grounded, the measured kinetic energy $E_{\rm kin}$ of the emitted electron is referred to $E_{\rm F}$. Then,

we obtain

$$E_{\mathrm{kin}} = h\nu - E_{\mathrm{B}}. \tag{2.2}$$

Roughly speaking, the energy $-E_{\mathrm{B}}$ is approximately regarded as the energy $\varepsilon$ of the electron inside the sample material before it is emitted. Therefore, the energy distribution of the electrons inside the material can be directly mapped by the distribution of the kinetic energies of photoelectrons emitted with monochromatic incident photons. Figure. 2.12 diagrammatically shows how the electronic density of state (DOS) is mapped by the electronic distribution curve (EDC), namely, the photoemission spectrum. In this thesis, photoemission spectra will be displayed so that the energy relative to $E_{\mathrm{F}}$,

$$E \equiv -E_{\mathrm{B}}, \tag{2.3}$$

is taken for the horizontal axis.

In real systems, the photoemission spectra are affected by the relaxation of the whole electron system in the solid, in addition to the one-electron energy $\varepsilon$ in the simple view (frozen-orbital approximation). In response to the hole produced by the photoemission process, the surrounding electrons tend to screen the hole to lower the total energy of the system. Therefore, considering the whole electron system, the binding energy $E_{\mathrm{B}}$ is given by the energy difference between the $N$-electron initial state $E_{\mathrm{i}}^{N}$ and the $(N-1)$-electron final state $E_{\mathrm{f}}^{N-1}$ as

$$E_{\mathrm{B}} + \Phi = E_{\mathrm{f}}^{N-1} - E_{\mathrm{i}}^{N}. \tag{2.4}$$

In other words, $E_{\mathrm{B}}$ is the energy of the hole produced by the photoemission process, including the relaxation energy of the total electron system. Hence, much information of the electron correlations is derived by analyzing the photoemission spectra.

### 2.2.2 Inverse photoemission spectroscopy

Inverse photoemission spectroscopy (IPES) investigates the electronic structure of unoccupied states, using the inverse process of the photoemission. When an incident electron falls into an unoccupied state of the material, the decrease in the electron energy is emitted as a photon. The emitted photons are collected in the IPES experiments for the mapping of the electronic structure of the unoccupied states. In bremsstrahlung isochromat spectroscopy (BIS), which is a kind of IPES, photons with a fixed energy are collected with varying the energy of incident electrons.



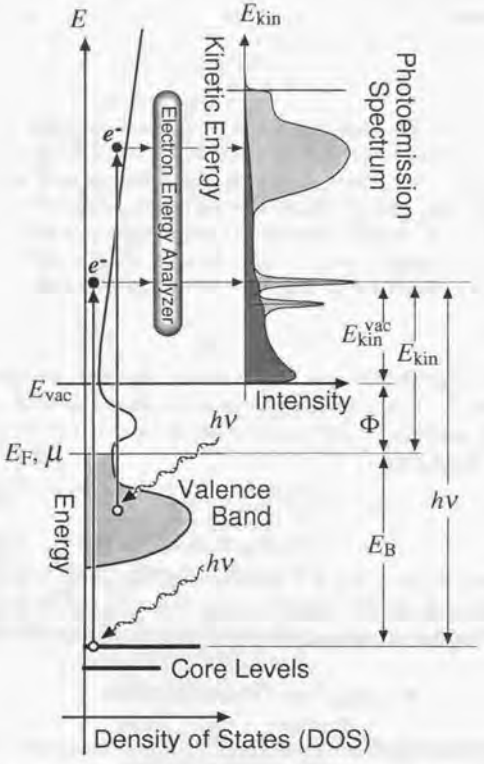


Figure 2.12: Schematic diagram showing the principle of photoemission spectroscopy (PES). Using the relation $E_{\mathrm{kin}} = h\nu - E_{\mathrm{B}}$, the electronic structure of the material is mapped by the electronic distribution curve (EDC), i.e., the photoemission spectrum.

### 2.2.3 Angle-resolved photoemission spectroscopy

In angle-resolved photoemission spectroscopy (ARPES), not only the energies but also the momenta of the electrons in the materials are probed. First, upon the photoexitation process, the crystal momentum should be conserved. Since the momentum of the ultraviolet light $h\nu/c$ is negligible compared to the size of the Brillouin zone, we obtain

$$\mathbf{K} = \mathbf{k} + \mathbf{G}, \tag{2.5}$$

where $\mathbf{k}$ and $\mathbf{K}$ are the crystal momenta of the electron in the initial and final states, respectively, and $\mathbf{G} = (2n_x\pi/a, 2n_y\pi/b, 2n_z\pi/c)$ is an arbitrary reciprocal lattice vector. Next, when the photoelectron escapes from the solid to the vacuum, part of the momentum perpendicular to the surface is lost due to the finite work function $\Phi$, whereas the momentum parallel to the surface is preserved owing to the translational symmetry along the surface. Therefore, when the momentum of the electron outside the vacuum is denoted by $\mathbf{p}$,

$$\mathbf{p}_\parallel/\hbar = \mathbf{K}_\parallel + \mathbf{G}'_\parallel. \tag{2.6}$$

In the ARPES experiments, the kinetic energy $E_{\rm kin}$ and the direction of the momentum, $\theta$ and $\phi$, of photoelectrons are measured using a directional electron energy analyzer. Therefore, we obtain the momentum of the emitted electron $\mathbf{p}_\parallel = (p_x, p_y)$ as

$$\begin{aligned} p_x &= \sqrt{2m_{\rm e}E^{\rm v}_{\rm kin}}\cos\phi\sin\theta \\ p_y &= \sqrt{2m_{\rm e}E^{\rm v}_{\rm kin}}\sin\phi \end{aligned} \tag{2.7}$$

for the geometry shown in Fig. 5.1. Summarizing Eqs. (2.2), (2.5), (2.6) and (2.7), we can directly observe both the energy $E \equiv -E_{\rm B}$ and the parallel momentum $\mathbf{k}_\parallel$ of the hole produced in the sample material by the photoemission process as

$$\begin{aligned} E &= E_{\rm kin} - h\nu \\ k_x &= \frac{\sqrt{2m_{\rm e}E^{\rm v}_{\rm kin}}}{\hbar}\cos\phi\sin\theta + \frac{2n''_x\pi}{a} \\ k_y &= \frac{\sqrt{2m_{\rm e}E^{\rm v}_{\rm kin}}}{\hbar}\sin\phi + \frac{2n''_y\pi}{b}, \end{aligned} \tag{2.8}$$

where $n''_x$ and $n''_y$ are arbitrary integers. Figure 2.13 schematically illustrates the procedure for the band mapping by the ARPES spectra. If the material under study is a two-dimensional system such as high-$T_{\rm c}$ cuprates, $E$ and $\mathbf{k}_\parallel$ are enough information to map the energy-momentum dispersion of the band structure.



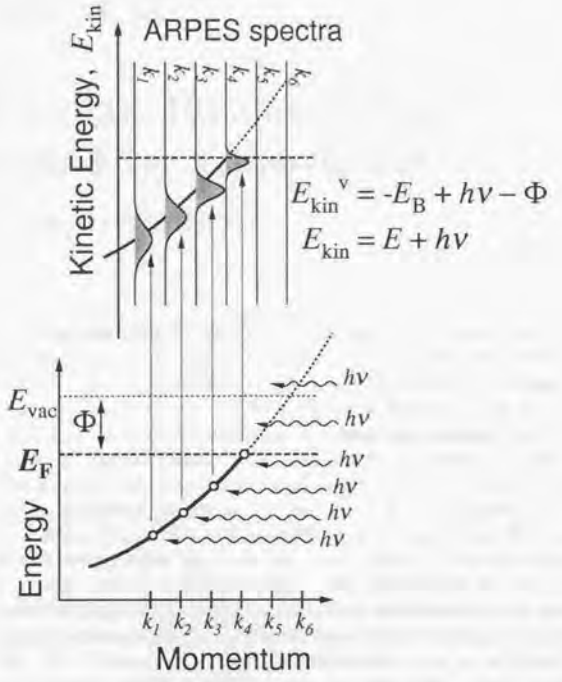


Figure 2.13: Schematic diagram showing the principle of angle-resolved photoemission spectroscopy (ARPES). The band dispersions in the material are directly mapped by the ARPES spectra.

# Chapter 3

# Chemical Potential Shift Studied by Core-Level Photoemission

The downward shift of the electron chemical potential ($\mu$) with hole doping ($\delta \equiv 1 - n \simeq x$) in $La_{2-x}Sr_xCuO_4$ has been deduced from the shifts of the photoemission and inverse photoemission spectra of O 1$s$, La 3$d$, La 4$f$ and Cu 2$p$ levels. The observed shifts of those levels indicate that the change in the Madelung potential with hole doping is almost screened by the redistribution of electronic charges. The deduced shift of the chemical potential $\mu$ is large ($\sim 1.5$ eV/hole) in the overdoped regime ($x > 0.15$), while it is suppressed ($< 0.2$ eV/hole) in the underdoped regime ($x < 0.15$), implying a divergent charge susceptibility ($\chi_c \equiv \partial n/\partial \mu \rightarrow$"$\infty$") near the metal-insulator transition. In the overdoped regime, the behaviors of the chemical potential $\mu$ and the electronic specific heat coefficient ($\gamma$) are consistently explained as those of a Fermi liquid with a Landau parameter $F_s^0 \sim 7 \pm 2$, whereas the same analysis gives an unphysical result in the underdoped regime. Perhaps, the non-Fermi-liquid behavior that $\gamma \rightarrow 0$ and $\chi_c \rightarrow$"$\infty$" for $x \rightarrow 0$ may be possible if a pseudogap is open at $\mu$ in the underdoped regime. It is also noted that the hole segregation in a dynamical stripe form proposed recently may pin the shift of $\mu$ upon hole doping in $La_{2-x}Sr_xCuO_4$.

*Main contents of this chapter have been published: "Chemical Potential Shift in Overdoped and Underdoped $La_{2-x}Sr_xCuO_4$" by A. Ino, T. Mizokawa, A. Fujimori, K. Tamasaku, H. Eisaki, S. Uchida, T. Kimura, T. Sasagawa and K. Kishio, Physical Review Letters* **79**, *2101 (1997).*

## 3.1 Introduction

A long-standing, yet unresolved issue in the high-$T_c$ cuprates is how the electronic structure evolves with hole doping from the antiferromagnetic Mott insulator to the paramagnetic metal/superconductor. For three-dimensional titanates such as $La_{1-x}Sr_xTiO_4$, it has been found that the renormalized conduction-electron mass $m^*$ diverges towards a filling-control metal-insulator transition (MIT) [64, 65] as predicted theoretically [66, 67]. On the other hand, for the cuprate $La_{2-x}Sr_xCuO_4$, the electronic specific heat coefficient $\gamma$ ($\propto m^*$) diminishes towards the MIT, suggesting the absence of the mass divergence [45-47]. In general, measuring the electron chemical potential $\mu$ as a function of the band filling $n$, one can deduce the behavior of the electron mass $m^*$, because the charge susceptibility,

$$\chi_c \equiv \frac{\partial n}{\partial \mu},$$

is proportional to $m^*$ within the Fermi liquid theory. Therefore, if $m^*$ diminishes towards the MIT, the rate of the chemical potential shift $\partial\mu/\partial n \propto (m^*)^{-1}$ would be enhanced near the MIT. Nevertheless, how the chemical potential is shifted with hole doping in the cuprates has been quite controversial so far. In one picture, the chemical potential $\mu$ is fixed in the middle of the charge-transfer gap of the parent insulator and new states emerge around $\mu$ with hole doping [37]. In another picture, the chemical potential $\mu$ jumps to the bottom of the energy gap upon hole doping and is further shifted downwards with increased doping concentration [8, 36]. In order to resolve these issues, it is necessary to clarify the critical behavior of the chemical potential near the MIT.

In photoemission experiments, since the energy of electrons are referred to $\mu$, it is possible to infer the shift of $\mu$ from the shifts of photoemission spectral features [68]. Indeed, a downward chemical potential shift of $\sim 1$ eV/hole with hole doping has been observed by photoemission spectroscopy in metallic samples of Y-substituted and oxygen-controlled $Bi_2Sr_2CaCu_2O_{8+y}$ system [68, 69]

For such a study, $La_{2-x}Sr_xCuO_4$ is suitable among the high-$T_c$ cuprates, because the hole concentration $\delta \equiv 1-n \simeq x$ in the $CuO_2$ plane is controlled over a wide range $0 \leq x \leq 0.3$. Furthermore, since the charge reservoir is well separated from the $CuO_2$ plane, the impurity potential of substituted Sr less affect the electronic states of the $CuO_2$ plane than in other cuprates. In the present work, therefore, $La_{2-x}Sr_xCuO_4$ has been studied by detailed photoemission experiments and the shift of chemical potential has been revealed from $x = 0$ to $x = 0.3$.



## 3.2 Experimental

Single crystals of $La_{2-x}Sr_xCuO_4$ with $x = 0$, 0.10, 0.15, 0.20 and 0.30 were supplied by Dr. K. Tamasaku, Dr. H. Eisaki and Prof. S. Uchida (Department of Superconductivity, University of Tokyo), and details of the growth conditions and characterization are described in Refs. 70, 71 and 72. Single crystals with $x = 0.074$ were supplied by Dr. T. Kimura, Mr. T. Sasagawa and Prof. T. Kishio (Department of Superconductivity, University of Tokyo), and details are described in Refs. 73 and 74. All the crystals were grown by the traveling-solvent floating-zone (TSFZ) method. The accuracy of the Sr concentration $x$ was $\pm 0.01$. All the samples were annealed so that the oxygen content is stoichiometric. The $x = 0$ sample was slightly hole-doped by excess oxygens: $y \sim 0.005$ in $La_2CuO_{4+y}$, judging from the Néel temperature of $\sim 220$ K [75] and hence $\delta \sim 0.01$.

X-ray photoemission (XPS) measurements were carried out using a PHI spectrometer equipped with a double-pass cylindrical-mirror analyzer (DCMA) and a Mg K$\alpha$ x-ray source ($h\nu = 1253.6$ eV). Inverse photoemission (bremsstrahlung isochromat spectroscopy: BIS) measurements were performed using a spectrometer equipped with a BaO cathode electron gun, a $SiO_2$ multicrystal monochromator, and a photon detector with CsI ($h\nu = 1486.6$ eV) evaporated on an Al plate. Incident electron current was limited to $\sim 100$ $\mu$A in order to minimize possible damages of sample surfaces. Uncertainty in energies of the BIS spectra were $\pm 0.15$ eV. For the XPS and BIS spectra, the total energy resolutions were $\sim 1.0$ and $\sim 0.8$ eV, respectively. Energies were calibrated using gold evaporated on each sample.

We found that any weak extrinsic features due to surface degradation or contamination hindered accurate determination of core-level peak positions, and therefore we had to keep the sample surfaces extremely clean. The clean surfaces were obtained by repeating *in situ* scraping with a diamond file at the liquid-nitrogen temperature ($\sim 77$ K) under ultra high vacuums of $\sim 3 \times 10^{-10}$ and $\sim 5 \times 10^{-10}$ Torr for the XPS and BIS measurements, respectively. During all the XPS and BIS measurements, the cleanliness of the sample surface was checked by the absence of the shoulder on the high binding energy side of the O 1$s$ core level as shown in Fig. 3.1(a). All the spectra presented here were taken less than $\sim 45$ minutes after scraping.

Great care was taken for measuring relative energy shifts. The XPS spectra for samples with different compositions were taken immediately in succession in order to avoid the change in any extrinsic factor. Consequently, it was possible to measure relative energy shifts in XPS spectra with an accuracy of $\pm 40$ meV even with the above resolutions, as far as the line

shape is unchanged with composition. There was no charging effects, which moves the spectral features away from the Fermi level, even for the $x = 0$ sample as can be seen from the data presented below. Therefore, it can be said that one can probe the charge response of $La_{2-x}Sr_xCuO_4$ on the energy scale of a few tens meV.

## 3.3 Core-level shifts implying the chemical potential shift

XPS spectra of the O 1$s$, La 3$d$ and Cu 2$p$ core levels and BIS spectra of the La 4$f$ level are shown in Fig. 3.1. Energy shifts of the core levels were determined by comparing the positions of spectral features whose line shapes are unchanged with composition.

The O 1$s$ and La 4$f$ line shapes are entirely identical among all the compositions, while the high binding energy side of the La 3$d$ peak shows small deviations for different samples, sensitively affected by slight surface degradation or contamination even with the above experimental precautions. Therefore, the shift of La 3$d$ is taken from the shift of the slope on the low binding energy side of the peak rather than the center of the peak. The obtained core-level shifts relative to $x = 0$ are plotted in Fig. 3.2 as a function of the hole concentration $\delta \simeq x$. The O 1$s$, La 3$d$ and La 4$f$ levels show almost the same shifts with $\delta$, namely, large shifts ($\sim 1.5$ eV/hole) towards lower binding energies for the overdoped ($x \gtrsim 0.15$) samples and considerably small shifts ($< 0.2$ eV/hole) for the underdoped ($x \lesssim 0.15$) samples.

The line shape of the Cu 2$p$ core level appear to be somewhat broadened for large $x$'s: a weak shoulder appears on the high binding energy side of the peak, probably corresponding to $Cu^{3+}$ component overlapping with the $Cu^{2+}$ one. Such two components have been clearly observed in Ti 2$p$ core-level spectra of $Y_{1-x}Ca_xTiO_3$, where the relative intensities of $Ti^{4+}$ component increases proportional to $x$ [76]. As $x$ increases in $La_{2-x}Sr_xCuO_4$, the peak position of Cu 2$p$ is shifted towards higher binding energies in the underdoped regime and then towards lower binding energies in the overdoped regime. This complicated Cu 2$p$ shift could be decomposed into two simple components, as shown in Fig. 3.2: one is the shift nearly linear in $\delta$ and the other is the shift common to all the core levels. The same decomposition has successfully been made for $La_{1-x}Sr_xCuO_{2.5}$ [77] and $La_{1.17-x}Pb_xVS_{3.17}$ [78].

In general, when energies are measured relative to the chemical potential $\mu$, the energy shift $\Delta E$ of a core level (or a localized empty level such as



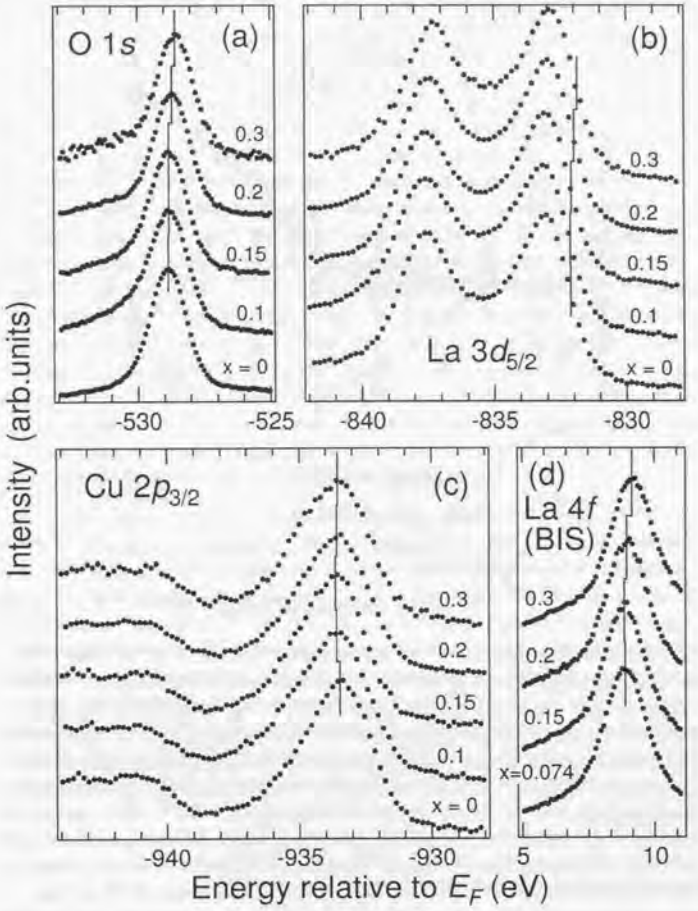


Figure 3.1: XPS spectra of (a) O 1$s$, (b) La 3$d$ and (c) Cu 2$p$ core levels and (d) BIS spectra of La 4$f$ level for $La_{2-x}Sr_xCuO_4$. Energies are referenced to the chemical potential $\mu$ (i.e., the Fermi level $E_F$). The O 1$s$, La 3$d$ and La 4$f$ levels show almost the same shift with $x$.

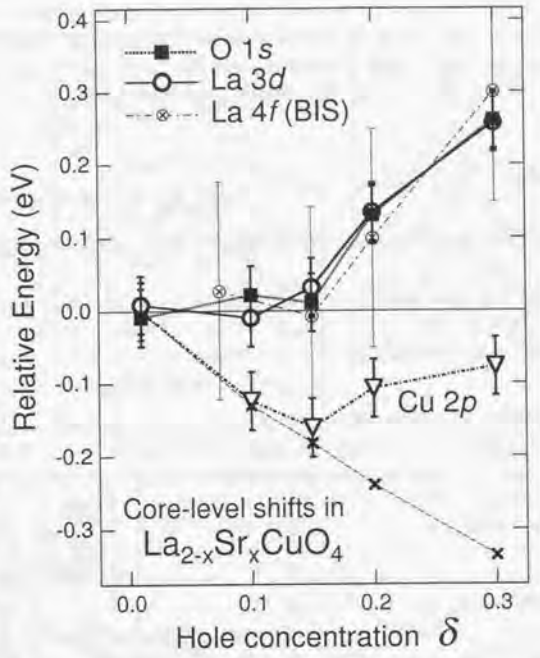


Figure 3.2: Energy shifts of O 1$s$, La 3$d$, La 4$f$ and Cu 2$p$ levels relative to the undoped sample ($x = 0$) plotted as a function of the hole concentration $\delta \simeq x$. Crosses with thin broken line at the bottom denote the shift of the difference between the Cu 2$p$ level and the average of the O 1$s$ and La 3$d$ levels, demonstrating that the Cu 2$p$ shift is decomposed into two simple components: the shift which is nearly linear in $\delta$ and the shift common to all the four levels.

La 4$f$) with varying chemical composition is given by

$$\Delta E = -\Delta\mu - K\Delta Q + \Delta V_{\rm M} + \Delta E_{\rm R},$$

where $\Delta\mu$ is the change in the chemical potential and common to all the atoms, $\Delta Q$ is the change in the number of valence electrons on the atom considered, $\Delta V_{\rm M}$ is the change in the Madelung potential and $\Delta E_{\rm R}$ is the change in the extra-atomic relaxation energy [79]. Here, $\Delta Q$ produces changes in



the electrostatic potential at the core-hole site as well as in the intra-atomic relaxation energy of the core-hole final state. $\Delta E_{\rm R}$ is due to changes in the screening of the core hole potential by metallic conduction electrons or by extra-atomic charge transfers through covalent bonds.

For the $La_{2-x}Sr_xCuO_4$ system, the 'linear' component of the Cu 2$p$ core-level shift may be regarded as due to the increase in the Cu valence $\Delta Q$ with hole doping from $Cu^{2+}$ towards $Cu^{3+}$, i.e., so-called "chemical shift." Strictly speaking, the holes doped in the $CuO_2$ plane has more O 2$p$ character than Cu 3$d$ character (Zhang-Rice singlet state surrounding the Cu site [7, 8]). However, note that, upon the photoemission from the Cu 2$p$ core orbitals, charge transfer from the O 2$p$ band to the Cu 3$d$ band occurs in the final state ($\underline{2p}3d^{10}\underline{L}$ configuration). Therefore, the holes doped into O 2$p$ much increases the charge transfer energy from O 2$p$ to Cu 3$d$ and consequently increases the binding energy of the Cu 2$p$ level. For the O 1$s$ level, on the other hand, no charge transfer occurs and the core-level shift due to the change in the oxygen valence is small because the oxygen contents is four times larger than Cu in $La_{2-x}Sr_xCuO_4$. Indeed, also for another cuprate $La_{1-x}Sr_xCuO_{2.5}$, the $x$-linear downward shift with hole doping has been observed in the Cu 2$p$ core-level shift rather than in the O 1$s$ shift [77].

Then, the remaining shift common to all the four levels should reflect the chemical potential shift $\Delta\mu$. In order to evaluate the $\Delta V_{\rm M}$ term for different core levels, we calculated changes in the Madelung potentials by taking into account the doping dependence of the crystal structure [80, 81] and assuming the average charges of $(3 - x/2)+$, $(2 + x)+$ and $2-$ at the La/Sr, Cu and O sites, respectively. As expected, the results showed that $\Delta V_{\rm M}$ are approximately linear in $x$ and towards different directions for different atomic sites. Hence, the nonlinear and identical shifts of the La 3$d$, La 4$f$ and O 1$s$ levels indicate that $\Delta V_{\rm M}$ is strongly screened by the redistribution of electronic charges. Therefore, $\Delta V_{\rm M}$ may be neglected. Moreover, also the change in the relaxation energy $\Delta E_{\rm R}$ due to metallic conduction electrons would be negligible because this would shift both the occupied and unoccupied levels toward the chemical potential, namely, towards the opposite directions between the occupied and unoccupied levels. We note that the line shapes of the core levels do not show asymmetric broadening characteristic of metallic screening [82] for all compositions, indicating negligibly weak metallic core-hole screening. The parallel shifts of the La 3$d$ and O 1$s$ core levels are consistent with this view, since the metallic screening would contribute more to an oxygen core hole in the metallic $CuO_2$ plane. Presumably, the carrier concentration ($\sim 10^{21}$ holes/cm$^{-3}$) is too low to produce ordinary metallic screening. For the above reasons, we can conclude that the nonlinear shift common to all

the core levels and the La $4f$ level faithfully reflects the chemical potential shift $\Delta\mu$. The $\Delta\mu$ deduced from the average of the O $1s$ and La $3d$ core-level shifts is plotted in Fig. 3.3 as a function of the hole concentration $\delta \simeq x$.

## 3.4 Analysis within Fermi-liquid theory

Let us first analyze the chemical potential shift in the overdoped regime, where the system is believed to be a Fermi liquid. For an isotropic Fermi liquid [83], the shift of the chemical potential $\mu$ is related to the density of states (DOS) of renormalized quasiparticles at $\mu$, $N^*(\mu)$, as

$$\frac{\partial\mu}{\partial n} = \frac{1+F_s^0}{N^*(\mu)} \equiv \left(\frac{m_b}{m^*}\right)\frac{1+F_s^0}{N_b(\mu)}, \tag{3.1}$$

where $m^*$ is the mass of renormalized quasiparticles, $m_b$ and $N_b(\mu)$ are the bare (unrenormalized) band mass and DOS at $\mu$, respectively, and $F_s^0$ ($> 0$) is a Landau parameter which represents the isotropic spin-symmetric part of the quasiparticle-quasiparticle repulsion. Accordingly, if $F_s^0$ is given, one can predict $\Delta\mu$ from $N^*(\mu)$ obtained from the measurement of the electronic specific heat coefficient $\gamma$:

$$\gamma = \frac{\pi^2}{3}k_B^2 N^*(\mu). \tag{3.2}$$

In Fig. 3.3(a), $\Delta\mu$ predicted for $F_s^0 = 0$ is shown by a solid curve. Since $\partial\mu/\partial n$ predicted from $\gamma$ is $8 \pm 2$ times smaller than the observed $\partial\mu/\partial n$ in the overdoped regime, we obtain $F_s^0 \sim 7 \pm 2$. From the observed $\gamma$ [47] and the calculated $N_b(\mu)$ [84], we have $m^*/m_b \equiv N^*(\mu)/N_b(\mu) \sim 2.5 \pm 0.5$. These values are comparable with those of liquid $^3$He at ambient pressure, $F_s^0 = 9.15$ and $m^*/m_b = 2.76$ [85].

On the other hand, in the underdoped regime, although the present results indicate that the charge susceptibility is enhanced ($\chi_c \to$ "$\infty$") as $\delta \to 0$ ($n \to 1$), the specific heat coefficient diminishes ($\gamma \to$ "0") [45-47]. If the Fermi-liquid relation (3.1) is applied to these behaviors, we have $F_s^0 \to -1$, which obviously contradicts the basic assumption that $F_s^0$ represents repulsive interaction. This suggests the breakdown of the Fermi-liquid description in the underdoped regime. (Inclusion of anisotropy in the Fermi-liquid analysis would not change the conclusion qualitatively.)



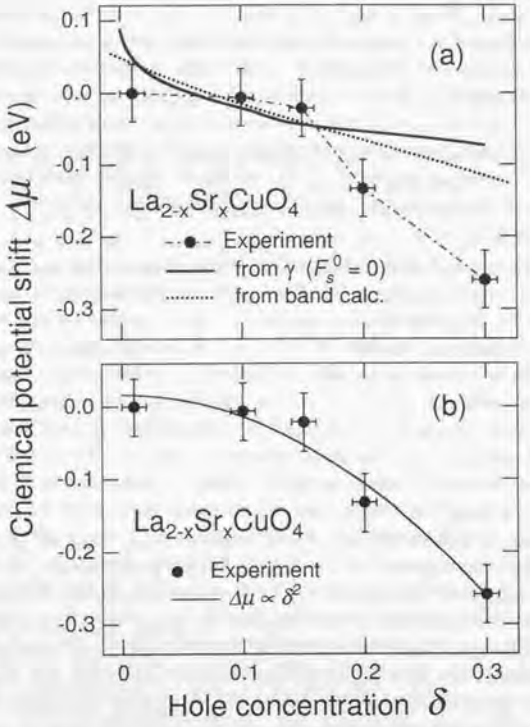


Figure 3.3: (a) Chemical potential shift $\Delta\mu$ plotted as a function of the hole concentration $\delta \simeq x$. The shift $\Delta\mu$ deduced from the photoemission experiments (filled circles) is compared with the shift predicted from the specific heat coefficient $\gamma$ [47] assuming $F_s^0 = 0$ (solid line), and the shift derived from $N_b(\mu)$ of the band-structure calculation [84] assuming $m^*/m_b = 1$ (dotted line). (b) Chemical potential shift $\Delta\mu$ fitted to $\Delta\mu \propto -\delta^2$ according to the prediction of the Monte-Carlo simulation [67].

## 3.5 Discussions

Suppression of the chemical potential shift $\chi_c \rightarrow$ "$\infty$" for $\delta \rightarrow 0$ has been suggested by numerical studies of the two-dimensional Hubbard model [67, 86]. In the Monte-Carlo study, the calculated chemical potential shift follows $\Delta\mu \propto -\delta^2$ for $0 < \delta \lesssim 0.3$ (hence $\chi_c \propto \delta^{-1}$) [67]. Indeed, the experimental data are compatible with $\Delta\mu \propto -\delta^2$ within experimental error as shown in Fig. 3.3 (b). Note that mean-field theories such as the Gutzwiller approximation [87] and the dynamical mean-field approximation [88] have not predicted the behavior observed presently, $\chi_c \rightarrow$ "$\infty$" for $\delta \rightarrow 0$, but predicted $\chi_c \rightarrow 0$ for $\delta \rightarrow 0$. This implies that quantum fluctuations are important near the MIT critical point.

One may suspect that the suppression of the chemical potential shift for small $\delta$ is caused by the pinning of the chemical potential by the impurity potential of substituted Sr or other defects. Such pinning effect cannot be excluded for the semiconducting $x = 0$ ($\delta \sim 0.01$) sample. However, the same effect would not occur in metallic samples ($\delta > 0.05$) when the impurity potential is weak enough. Indeed, the acceptor binding energy has been estimated to be as small as $\sim 40$ meV for semiconducting $La_2CuO_{4+y}$ with $y \sim 0.001$ and is rapidly reduced to below $\sim 10$ meV for $y \sim 0.01$ [89]. These small acceptor binding energies indicate that the chemical potential in the $x = 0$ sample is located very close to the bottom of the band gap of $La_2CuO_4$, and that for the metallic samples the pinning effect was too weak to affect the chemical potential shift. Recently, Zaanen and co-workers [48] have suggested that doped holes are segregated in the boundaries of antiferromagnetic domains in a stripe form in $La_{2-x}Sr_xCuO_4$. If such hole segregation occurs, the chemical potential $\mu$ may be pinned upon hole doping. In fact, the system becomes metallic already at $\delta \sim 0.05$ but the stripe correlation can normally exist as dynamical fluctuations [49]. The presence of the spin-charge stripes itself in $La_{2-x}Sr_xNiO_4$ and Nd-doped La cuprates [50] means that the Sr impurity potential is practically negligible when the stripe correlation is observed.

The experimental observation $\gamma \rightarrow$ "0" for $\delta \rightarrow 0$ in the underdoped samples, on the other hand, has not been predicted by any theoretical studies which reproduce $\chi_c \rightarrow$ "$\infty$" on two-dimensional metals. The apparently conflicting behaviors of $\gamma$ and $\chi_c$ may be resolved if we assume that a small excitation (pseudo)gap is opened at $\mu$ within the renormalized quasiparticle band for any small $\delta$. Recent angle-resolved photoemission studies have indicated the opening of a "normal-state gap" above $T_c$ in underdoped $Bi_2Sr_2CaCu_2O_{8+y}$ [29-33] as described by a mean-field treatment of the $t$-$J$ model [90]. Alternatively, strong antiferromagnetic spin fluctuations in the underdoped regime may give rise to a pseudogap at $\mu$ [91]. Pairing fluctuations (or preformed Cooper pairs) [92-95] are another possible explanation for the suppression of $\gamma$ in spite of the enhanced $\chi_c$. It should be noted that the experimental results for the underdoped samples are neither compatible with the simple small hole pocket which holds the same expression (3.1), provided that $N^*(\mu)$ is interpreted as the quasiparticle DOS around the "small Fermi surfaces."



Finally, we note that the present result for the overdoped $La_{2-x}Sr_xCuO_4$ is similar to the result ($\partial\mu/\partial n \sim 1$ eV/electron) for metallic $Bi_2Sr_2Ca_{1-x}Y_xCu_2O_8$ [68] and $Bi_2Sr_2CaCu_2O_{8+y}$ [69]. On the other hand, for semiconducting $Bi_2Sr_2Ca_{1-x}Y_xCu_2O_8$ samples, the rapid shift of $\sim 8$ eV/electron has been reported [68]. This rapid shift is likely to be the reminiscent of the discontinuous jump of $\mu$ through the band gap in the insulator: $\partial\mu/\partial n \rightarrow \infty$, which is practically obscured to be finite in $Bi_2Sr_2Ca_{1-x}Y_xCu_2O_8$ because a low but finite density of localized states is created within the band gap by the Ca-Y disorder adjacent to the $CuO_2$ planes unlike in $La_{2-x}Sr_xCuO_4$.

## 3.6 Conclusion

In summary, we have experimentally determined the doping dependence of the chemical potential shift $\Delta\mu$ in $La_{2-x}Sr_xCuO_4$ and observed a suppression of the shift in the underdoped regime ($x \lesssim 0.15$). The result implies that the charge susceptibility is enhanced towards $\delta \sim 0$, most likely reflecting critical fluctuations near the MIT such as microscopic phase separation in the underdoped $La_{2-x}Sr_xCuO_4$. Comparing the result with the electronic specific heat coefficient $\gamma$, the behaviors of $\mu$ and $\gamma$ are consistently explained within the Fermi-liquid theory in the overdoped regime if a large Landau parameter $F_s^0 \sim 7 \pm 2$ is assumed. On the other hand, the same comparison indicates a breakdown of the Fermi-liquid description in the underdoped regime, suggesting the opening of a (pseudo)gap at the chemical potential. It is interesting to see how the chemical potential behaves near the MIT for three-dimensional and quasi one-dimensional systems, because such information combined with electronic specific heats would give deep insight into the Fermi-liquid *versus* non-Fermi-liquid behaviors of unconventional metals. The temperature dependence of the chemical potential shift would also reflect the highly non-trivial nature of correlated electrons near the MIT.

# Chapter 4

# Pseudogap Behavior in Momentum-Integrated Electronic Structure

Photoemission (PES) and inverse photoemission (BIS) studies have been performed on $La_{2-x}Sr_xCuO_4$ in a wide hole concentration ($x$) range from a heavily overdoped metal to an undoped antiferromagnetic (AF) insulator. On the energy scale of the charge-transfer (CT) gap, the spectral weight is transferred with hole doping from the upper Hubbard band ($\sim +2.5$ eV) to the entire CT gap region centered at $\sim +1$ eV. Around the chemical potential ($\mu$), the spectral intensity is suppressed to some extent as a pseudogap on the energy scale of $\sim 0.1$ eV for underdoped samples. As $x$ decreases towards the metal-insulator transition, the intensity at $\mu$ is gradually suppressed with an $x$-dependence similar to the decrease in the electronic specific heat coefficient and the temperature-independent part of the magnetic susceptibility. Also the width of the pseudogap increases as $x$ decreases towards AF insulator, following the $x$-dependences that the characteristic temperatures of the magnetic susceptibility and the Hall coefficient increase with decreasing $x$. The coherence temperature lowered by the pseudogap may indicate that the incoherent metallic state dominate the transport properties of the underdoped cuprates. As for the present pseudogap, the energy scale ($\sim 0.1$ eV) and the doping dependence suggest that it is originated from AF correlations.

*Main contents of this chapter have been published: "Doping Dependent Density of States and Pseudogap Behavior in $La_{2-x}Sr_xCuO_4$" by A. Ino, T. Mizokawa, K. Kobayashi, A. Fujimori, T. Sasagawa, T. Kimura, K. Kishio, K. Tamasaku, H. Eisaki and S. Uchida, Physical Review Letters* **81**, *2124 (1998).*

## 4.1 Introduction

In order to understand the mechanism of high-temperature superconductivity in the cuprates, a central issue has been the electronic structure of the $CuO_2$ plane near the filling-control metal-insulator transition (MIT). In spite of extensive studies, it still remains unclear how the electronic structure evolves with hole doping, especially, between an underdoped metal and an antiferromagnetic (AF) insulator. For a systematic study of the doping dependence near the MIT, $La_{2-x}Sr_xCuO_4$ (LSCO) system is suitable because the hole concentration in the $CuO_2$ plane is well controlled over a wide range and uniquely determined by the Sr concentration $x$ (and small oxygen non-stoichiometry). Using LSCO, one can investigate the electronic structure of the $CuO_2$ plane continuously from the heavily overdoped limit ($x \simeq 0.3$) to the undoped AF insulator ($x = 0$) in a single system.

Indeed, spectral weight transfer has been observed for LSCO by optical conductivity [6] and x-ray absorption spectroscopy (XAS) [96] experiments. However, still it has been an open question whether the spectral weight transfer with hole doping is into the unoccupied states at the top of the lower Hubbard band (LHB) [36] or into the charge-transfer (CT) gap region in which the chemical potential $\mu$ is pinned [37, 6], because the XAS spectra have uncertainty in the position of $\mu$ and are affected by the core-hole potential. Therefore, for the true understanding of the weight transfer, it is necessary to measure the true electron removal and additional spectra referred to $\mu$ by photoemission and inverse photoemission spectroscopy.

Recently, a "normal-state gap" behavior above $T_c$ has been observed by angle-resolved photoemission spectroscopy (ARPES) in underdoped $Bi_2Sr_2CaCu_2O_{8+y}$ (Bi2212) [29-33] and a "spin-gap" behavior by NMR in underdoped $YBa_2Cu_3O_{7-y}$ (YBCO) [38, 39]. The magnitude of the normal-state gap is of the same order as the superconducting gap at optimal doping. On the other hand, the underdoped cuprates also have characteristic temperatures which are considerably *higher* than $T_c$ in the uniform magnetic susceptibility [40], the electronic specific heat [41], the Hall coefficient [42, 43] and the electrical resistivity [40]. All these characteristic temperatures show similar behaviors in LSCO: they increase from $\sim 300$ K at optimal doping $x \sim 0.15$ to $\sim 600$ K at $x \sim 0.1$, suggesting a pseudogap-type electronic structure. In addition, if a pseudogap is opened at $\mu$, it can be reconciled that both the electronic specific heat coefficient $\gamma$ [41, 47] and the chemical potential shift $\Delta\mu$ with doping are suppressed towards the MIT as discussed in Chapter 3. Experimentally, however, the relation between those characteristic temperatures and the actual electronic structure has not been clarified so far. In order to obtain the total view of those "gaps" and their doping dependences, it is essential to measure the total density of states (DOS) by angle-integrated photoemission spectroscopy (AIPES) with a high energy resolution.



In this Chapter, the results of photoemission spectroscopy (PES) and inverse photoemission spectroscopy (bremsstrahlung isochromat spectroscopy: BIS) on high-quality LSCO samples are presented in a wide hole concentration range from $x = 0$ (undoped AF insulator) to $x = 0.3$ (heavily overdoped), focusing on the spectral weight transfer and the evolution of the pseudogap.

## 4.2 Experimental

Single crystals of $La_{2-x}Sr_xCuO_4$ with $x = 0.074, 0.13, 0.175$ and $0.203$ were supplied by Mr. T. Sasagawa, Dr. T. Kimura and Prof. T. Kishio (Department of Superconductivity, University of Tokyo), and details of the growth conditions and characterization are described in Refs. 73 and 74. Single crystals with $x = 0.15, 0.20$ and $0.30$ were supplied by Dr. H. Eisaki, Dr. K. Tamasaku and Prof. S. Uchida (Department of Superconductivity, University of Tokyo), and details are described in Refs. 70, 71 and 72. All the crystals were grown by the traveling-solvent floating-zone (TSFZ) method. The samples had $T_c$'s of 18, 34, 32, 21 and 0 K for $x = 0.074, 0.13, 0.175, 0.203$ and 0.30, respectively, with transition widths of about 0.5 K. The accuracy of the Sr concentration is $\pm 0.01$. All the samples were annealed so that the oxygen content is stoichiometric. The $x = 0$ sample was annealed in a reducing atmosphere (100 Torr $O_2$ at 800°C) and confirmed that the Néel temperature was higher than 250 K, meaning that the hole concentration was less than 0.004 [75].

Photoemission (PES) measurements were carried out using the He I resonance line ($h\nu = 21.4$ eV) of a VG (Vacuum Generators) helium discharge lamp. The spectra were collected by a VSW (Vacuum Science Workshop) hemispherical analyzer of 150 mm radius. The total instrumental energy resolution was $\sim 22$ meV. Clean surfaces were obtained by *in situ* scraping with a diamond file under an ultra high vacuum with a base pressure in the $10^{-11}$ Torr range. The scraping was repeated every 40 minutes. In order to minimize the degradation of the sample surfaces, the samples were cooled down and kept at $T \sim 18$ K during the measurements using a closed-cycle helium refrigerator. Only $x = 0$ sample was measured at $\sim 70$ K to avoid charging effect, but still a slight charging effect (at most $\sim 10$ meV) could

not be eliminated for $x = 0$. Energies were carefully calibrated using gold evaporated on each sample so that the uncertainty in energies was about $\pm 1$ meV. The presented PES spectra were corrected for the He I$^*$ satellites, which are separated by $\sim 1.87, 2.53$ and $2.83$ eV from the main line, assuming that He I$^*$/He I ratio are $\sim 0.028, 0.0045$ and $0.0005$, respectively.

Inverse photoemission (bremsstrahlung isochromat spectroscopy: BIS) measurements were performed using a spectrometer equipped with a BaO cathode electron gun, a $SiO_2$ multicrystal monochromator, and a photon detector with CsI ($h\nu = 1486.6$ eV) evaporated on an Al plate. The total instrumental energy resolution was $\sim 0.8$ eV. In order to minimize possible damages of sample surfaces, incident electron current was limited to $\sim 100$ $\mu$A and all the BIS measurements were performed under an ultra high vacuum of $\sim 5 \times 10^{-10}$ Torr at liquid-nitrogen temperature $\sim 77$ K. Clean surfaces were obtained by *in situ* scraping with a diamond file and the scraping was repeated every 40 minutes. The absence of surface degradation/contamination was checked using O 1*s* core-level photoemission during the BIS experiments. Energies were calibrated using gold evaporated on each sample. Unfortunately, we could not record BIS spectra for the undoped ($x = 0$) sample because of charging.

## 4.3 Entire valence and conduction bands

Figure 4.1 shows the PES and BIS spectra of the entire valence and conduction bands of $La_{2-x}Sr_xCuO_4$ for various compositions. The PES spectra have no trace of hump at $\sim -9.5$ eV, indicating the high sample quality and the cleanliness of the sample surfaces.

All the PES spectra presented in this Chapter have been normalized to the maximum intensity of the valence band, because the general line shape of the valence band is almost unchanged with composition as shown in Fig. 4.1, while the area of the valence band was hard to determine accurately due to the experimentally ambiguous background on the low kinetic energy side of the valence band. All the presented BIS spectra have been normalized so that the intensity of the sharp La 4*f* peak is proportional to the amount of La atoms ($\propto 2 - x$).



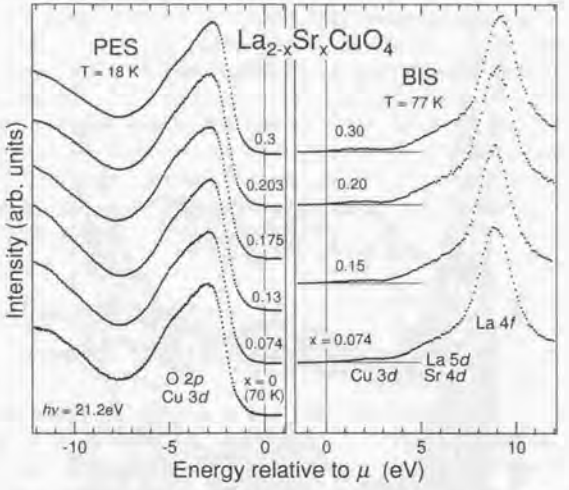


Figure 4.1: PES and BIS spectra of the entire valence and conduction bands of $La_{2-x}Sr_xCuO_4$ for various compositions. The valence band with a peak at $\sim -3$ eV is originated from O 2*p* and Cu 3*d* states. The sharp peak at $\sim +9$ eV is due to the La 4*f* orbitals and the shoulder at $\sim +6$ eV is attributed to the La 5*d* and Sr 4*d* bands. The spectral intensity derived from the unoccupied Cu 3*d* band is the faint structure near the chemical potential $\mu$ in the BIS spectra ($\lesssim +3$ eV). The absence of a hump at $\sim -9$ eV indicates the cleanliness of the sample surfaces.

## 4.4 Structures on the energy scale of charge-transfer gap

Figure 4.2 is an enlarged view of the PES and BIS spectra on the energy scale of the CT gap. The BIS spectra show that the spectral weight is transferred with hole doping from around $\sim 2.5$ eV to around $\sim 1$ eV. Hence the feature at $\sim 2.5$ eV is attributed to the upper Hubbard band (UHB). On the other hand, since the CT gap has a magnitude of about $\sim 1.5$ eV according to the optical study [5, 6], the growing weight is spread over the entire CT-gap region centered at $\sim 1$ eV in the BIS spectra and therefore may be assigned to "in-gap" states induced by the hole doping. Indeed, the spectral weight may be transferred also from the lower Hubbard band [or more precisely the

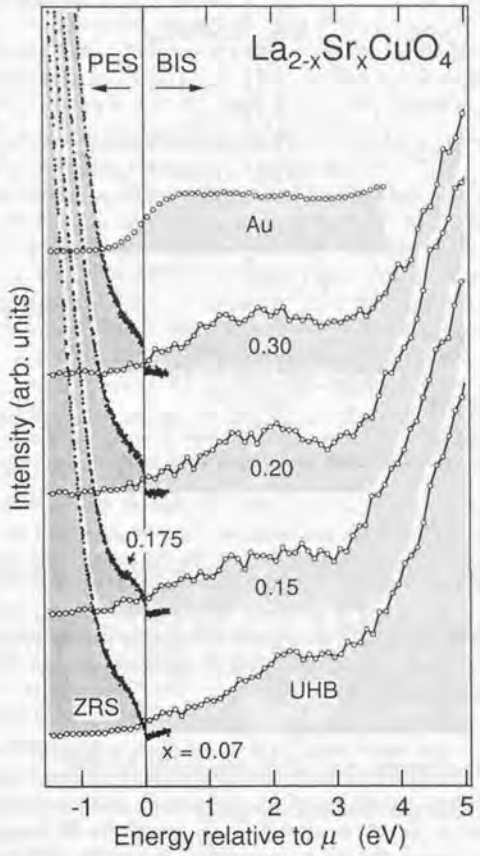


Figure 4.2: PES and BIS spectra of $La_{2-x}Sr_xCuO_4$ around the charge-transfer (CT) gap region. Also the spectrum of gold (Au) is displayed as a reference of the energy resolution of the BIS spectra. Spectral weight is transferred with hole doping from the feature at $\sim 2.5$ eV to the entire CT-gap region centered at $\sim 1$ eV. Therefore, the feature at $\sim 2.5$ eV and the top of the occupied band are attributed to the upper Hubbard band (UHB) and the Zhang-Rice singlet (ZRS) band, respectively.



Zhang-Rice singlet (ZRS) band] to above the chemical potential $\mu$ upon hole doping [36, 97]. Unfortunately, the tail of the intense O $2p$ band overlaps the ZRS band and is shifted upwards with doping, prohibiting us to estimate the intensity change of the ZRS band. As suggested in Refs. 36, 97 and 96, the position of $\mu$ appear to be located near the bottom of the CT gap. However, the present results show that the doping-induced weight is distributed not only just above $\mu$ but also over the wide energy range in the CT-gap region and that the DOS at $\mu$ is kept relatively low as revealed by comparison with the spectrum of gold.

## 4.5 Fine structure around the chemical potential

The PES spectra near the chemical potential $\mu$ are further enlarged in Fig. 4.3. With decreasing $x$, the intensity at $\mu$ starts to decrease in the metallic phase ($x < 0.2$) and disappears in the insulating phase ($x = 0$). While in the overdoped region ($x \gtrsim 0.2$) the spectra show an ordinary metallic Fermi edge, in the optimally doped and underdoped region ($x \lesssim 0.15$) the spectra show a pseudogap-type lineshape around $\mu$ in the sense that the spectral intensity gradually diminishes towards $\mu$ from somewhat below $\mu$ as marked by vertical bars in Fig. 4.3. Here the vertical bars indicate the points of maximum curvature determined by taking the second derivatives of the spectra. It appears that a rather large pseudogap develops in its width and depth as $x$ decreases towards the AF insulator ($x = 0$). Note that the energy scale of the DOS suppression is as large as the order of $\sim 0.1$ eV ("high-energy pseudogap" or "weak pseudogap") and therefore that it does *not* correspond to the "normal-state gap" ("low-energy pseudogap" or "strong pseudogap") which has a magnitude similar to the superconducting gap ($\sim 25$ meV for Bi2212) and has been observed in the ARPES spectra of underdoped Bi2212 [29-33]. In view of the energy scale, the marked feature in AIPES may rather correspond to the broad feature at $(\pi, 0)$ in the ARPES spectra of underdoped Bi2212 [98]. Unfortunately, one cannot judge whether the low-energy normal-state gap is opened or not in the underdoped LSCO from the present spectra, because the spectra were taken at a temperature below $T_c$ ($T \sim 18$ K $< T_c$) for $x = 0.13, 0.175$ and $0.203$.

In order to determine the spectral DOS at $\mu$, $\varrho(\mu)$, and the precise position of the leading edge, the spectra near $\mu$ ($> -0.1$ eV) have been fitted to linear DOS multiplied by the Fermi-Dirac distribution function convoluted with the Gaussian representing the instrumental resolution, as shown

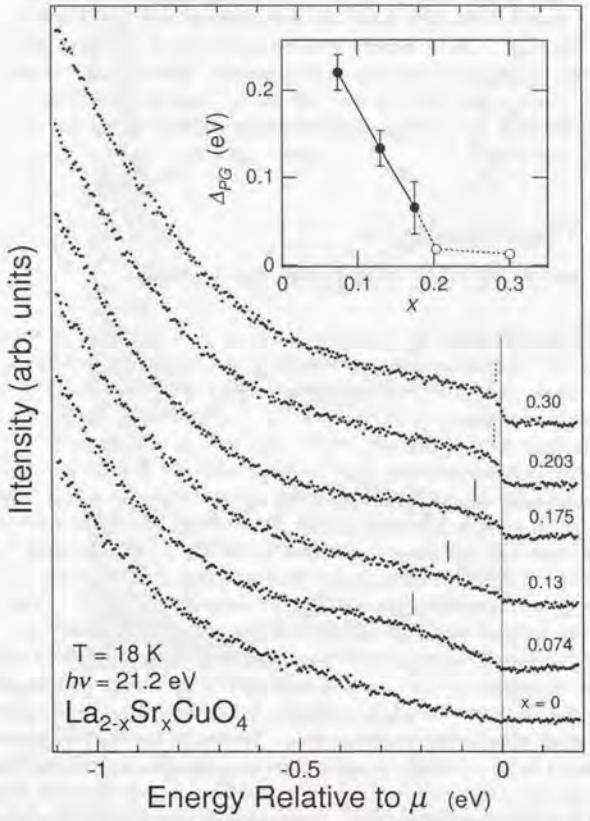


Figure 4.3: PES spectra of $La_{2-x}Sr_xCuO_4$ near the chemical potential $\mu$. The vertical bars mark the point of maximum curvature and represent the energy of the pseudogap $\Delta_{PG}$, whose doping dependence is shown in the inset.



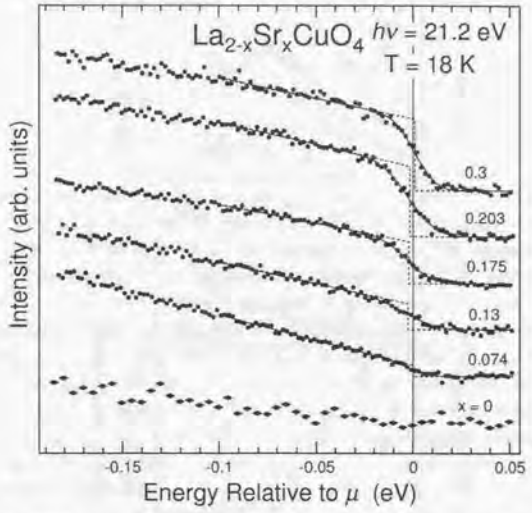


Figure 4.4: PES spectra in the vicinity of the chemical potential $\mu$ ($> -0.1$ eV), fitted to linear DOS multiplied by the Fermi-Dirac distribution function convoluted with the Gaussian representing the instrumental resolution. Hypothetical $T \to 0$ spectra without Gaussian broadening are also shown by dotted lines. The spectra were normalized to the maximum intensity of the valence band.

in Fig. 4.4. The obtained $\varrho(\mu)$ are shown in Fig. 4.5(a), where error bars include uncertainties in the normalization procedure due to subtle changes in the valence-band lineshape. In Fig. 4.5(a), $\varrho(\mu)$ is compared with the electronic specific heat coefficient $\gamma$ [47] and the Pauli-paramagnetic component $\chi_s^c$ of the spin susceptibility [40]. The three quantities, $\varrho(\mu)$, $\gamma$ and $\chi_s^c$, show quite similar $x$-dependences: with decreasing $x$, they slowly increase or remain nearly constant for $x > 0.2$, take a maximum around $x = 0.2$ and then decrease towards $x \sim 0$ for $x < 0.2$. A similar behavior has been predicted by Hubbard-model calculations [99] although the absolute value of the calculated $\varrho(\mu)$ is much higher than the observed one. In addition to $\varrho(\mu)$, we know the quasiparticle DOS at $\mu$, $N^*(\mu)$, which is obtained from $\gamma$ as $N^*(\mu) = \gamma/(\frac{1}{3}\pi^2 k_B^2)$, and the unrenormalized DOS at $\mu$, $N_b(\mu)$, which is calculated by band theory within the local density approximation (LDA) [84]. Using $\varrho(\mu)$, $N^*(\mu)$ and $N_b(\mu)$, one can deduce the mass enhancement

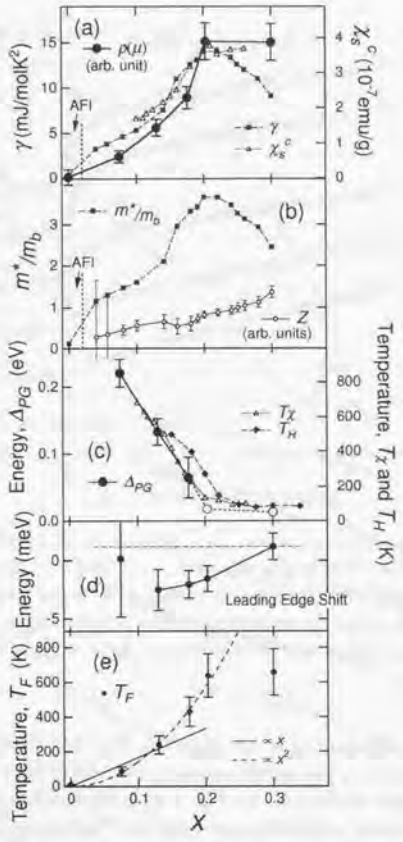


Figure 4.5: Doping dependences of (a) the spectral density of states (DOS) at $\mu$, $\varrho(\mu)$, compared with the electronic specific heat coefficient $\gamma$ [47] and the Pauli-paramagnetic component $\chi_s^c$ of the spin susceptibility [40], (b) the renormalization factor $Z = \varrho(\mu)/N^*(\mu)$ and the mass enhancement factor $m^*/m_b = N^*(\mu)/N_b(\mu)$, (c) the pseudogap energy $\Delta_{PG}$ compared with the characteristic temperatures $T_\chi$ where the magnetic susceptibility $\chi(T)$ takes a maximum [40] and $T_H$ below which the Hall coefficient $R_H(T)$ increases [42], (d) the position of the leading edge and (e) the "Fermi temperature" (coherence temperature) $T_F = (1/\pi k_B)\varrho(\omega)/(\partial\varrho(\omega)/\partial\omega)|_{\omega=\mu}$ of doped holes.



factor

$$\frac{m^*}{m_b} \equiv \frac{N^*(\mu)}{N_b(\mu)}$$

and the renormalization factor

$$Z \equiv \frac{\varrho(\mu)}{N^*(\mu)},$$

and the results are shown in Fig. 4.5(b). Figures 4.5(a) and (b) imply that the decrease in $m^*$ is a result of the development of the high-energy pseudogap observed in the AIPES spectra as the decrease in $\varrho(\mu)$. The renormalization factor (or equivalently the quasiparticle spectral weight) $Z$ also decreases towards $x = 0$, but it is not clear whether $Z$ goes to zero or remains finite for $x \to 0$ because of experimental uncertainties. For a typical Mott MIT system, e.g., $La_{1-x}Sr_xTiO_3$, the quasiparticle mass ($\propto m^* \propto \gamma$) is enhanced as $x$ decreases until the boundary of the AF phase is reached [64, 65]. It should be noted that also for LSCO the quasiparticle mass is enhanced with decreasing $x$ for $x > 0.2$ (the region where the pseudogap is absent), while the quasiparticle mass starts to decrease in the metallic phase ($x < 0.2$) far before the MIT boundary because of the formation of the high-energy pseudogap.

The energy of the high-energy pseudogap $\Delta_{PG}$ was defined by the binding energy of the point of maximum curvature determined by taking the second derivatives (as marked by the vertical bars in Fig. 4.3). The picture of the spectral DOS of the underdoped LSCO is schematically drawn in Fig. 4.6. Since $\Delta_{PG}$ is of the order of 0.1 eV, $\Delta_{PG}$ is compared with the characteristic temperatures $T_\chi$ [40] and $T_H$ [42] in Fig. 4.5(c). Here $T_\chi$ and $T_H$ are the temperatures at which the magnetic susceptibility $\chi(T)$ takes a maximum and below which the Hall coefficient $R_H(T)$ increases, respectively. Figure 4.5(c) shows that $\Delta_{PG}$ follows the $x$-dependence of $T_\chi$ and $T_H$. It has also been reported that the temperature $T_\rho$ below which the electrical resistivity $\rho(T)$ deviates downward from the linear-$T$ behavior follows $T_\chi$ and $T_H$ [40]. The similar $x$-dependence of $\Delta_{PG}$, $T_\chi$, $T_H$ and $T_\rho$ imply that these temperatures are closely related to the development of the high-energy pseudogap. Therefore, those characteristic temperatures may be referred as a "pseudogap temperature" $T_{PG}$. Then we find $2\Delta_{PG}/k_BT_{PG} \simeq 6$, indicating that the interaction is in the strong coupling regime.

Focusing on the energy scale of the superconducting gap, the position of the leading-edge midpoint obtained from the fitting is shown in Fig. 4.5(d). In going from the overdoped region to the optimum doping, the edge is shifted downward by $\sim 4$ meV as schematically illustrated in Fig. 4.6. If we attribute the shift to the opening of the superconducting gap, we obtain the

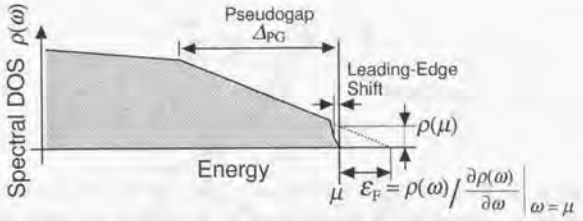


Figure 4.6: Schematic picture of the spectral density of states (DOS), $\varrho(\omega)$, around the chemical potential $\mu$ for the underdoped $La_{2-x}Sr_xCuO_4$, showing the characteristic energy scales: the pseudogap energy $\Delta_{PG} \simeq 3k_BT_{PG}$ above which $\varrho(\omega)$ is suppressed towards $\mu$, the energy of the leading-edge shift and the Fermi energy $\varepsilon_F \equiv \pi k_BT_F$ of the hypothetical hole pocket.

ratio $2\Delta/k_BT_c \sim 2$, which is smaller than the typical value $2\Delta/k_BT_c \sim 4-6$ deduced from the ARPES studies on Bi2212 [26] and YBCO [35]. However, if the superconducting gap is anisotropic as in $d$-wave pairing [26-28, 30, 32, 34, 35], it is understandable that the angle-integrated spectra fitted to the simple step function give a smaller leading-edge shift than the angle-resolved data.

## 4.6 Fermi temperature

In the underdoped regime, since $\varrho(\mu)$ is small and the slope of the DOS at $\mu$, $\partial\varrho(\omega)/\partial\omega|_{\omega=\mu}$, is steep, the Fermi edge would be obscured at high temperatures and the Fermi-Dirac distribution would lose its meaning. The crossover temperature for such a disappearance of the Fermi edge is thus given by

$$T_F = \frac{1}{\pi k_B}\,\varrho(\omega)\Big/\frac{\partial\varrho(\omega)}{\partial\omega}\Big|_{\omega=\mu},$$

which is shown in Figs. 4.5(e) and 4.7, and may be called the "coherence temperature" of the doped holes. $T_F$ may also be interpreted as the "Fermi temperature" of the doped holes because if one linearly extrapolates the DOS $\varrho(\omega)$ beyond $\mu$ as shown in Fig. 4.6, then the hypothetical hole pocket would have the Fermi energy of $\varepsilon_F \equiv \pi k_BT_F$. At temperatures higher than $T_F$ ($T \gtrsim T_F$), transport properties would be dominated by the incoherent charge dynamics of the doped holes [100]. Figure 4.5(e) shows that $T_F$ becomes very low ($< 100$ K) in the underdoped regime, indicating that the



thermodynamic and transport properties of the underdoped LSCO behave as those in "incoherent metals." Note that $T_F$ is considerably lower than $T_{PG}$ as shown in Fig. 4.7 and even lower than $J/\pi k_B$ in the underdoped region. Under such a condition, the kinetic energy gain of the doped holes alone may be insufficient to destroy the AF order, and alternatively the disappearance of the long-range order may be attributed to strong quantum fluctuations characteristic of two-dimensional systems. Figure 4.5(e) also suggests that, for small $x$, $T_F$ scales with $x^2$ rather than $x$. According to the hyperscaling hypothesis of the MIT [101], the critical behavior of $T_F$ and chemical potential shift $\Delta\mu$ near the MIT is given by $T_F \propto x^{z/d}$ and $\Delta\mu \propto x^{z/d}$, where $z$ is the dynamical exponent of the MIT and $d$ is the spatial dimension ($d = 2$). Thus the present result ($T_F \propto x^2$) implies $z = 4$, which is consistent with the suppression of the chemical potential shift ($\Delta\mu \propto x^2$) observed for the underdoped LSCO in Chapter 3. This $z$ value is distinctly different from that of an ordinary metal-to-band insulator transitions, i.e., $z = 2$.

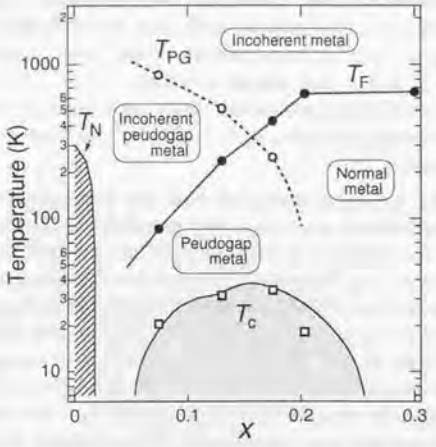


Figure 4.7: Crossover temperatures of $La_{2-x}Sr_xCuO_4$ shown in the phase diagram as a function of $x$. Open and filled circles denote the pseudogap temperature $T_{PG} = \Delta_{PG}/3k_B$ and the Fermi temperature (coherence temperature) $T_F = (1/\pi k_B)\varrho(\omega)/(\partial\varrho(\omega)/\partial\omega)|_{\omega=\mu}$, respectively.

## 4.7 Origins of the pseudogaps

Let us discuss the microscopic origin of the pseudogap behavior described in this Chapter. Since the energy scale of the present pseudogap is of the order of the super-exchange energy $J \sim 0.1$ eV, it is tempting to associate the pseudogap with the development of AF correlations or short-range AF order in the underdoped region [102, 103]. In this scenario, when the temperature is lowered below $T_{\rm PG}$, the AF correlation length increases and consequently the DOS shows a pseudogap reminiscent of the AF gap, which is present at $\mu$ for the antiferromagnetically ordered state [104]. The observed pseudogap may also be related with the short-range stripe order because it also originates from AF correlations. It has been stressed that LSCO is close to the instability of stripe order even in the metallic phase [49, 50]. Since $T_{\rm F} \ll T_{\rm PG} \sim J/\pi k_{\rm B}$ in the underdoped region, the system cannot be regarded as a normal Fermi liquid which is weakly perturbed by AF correlation but rather as an essentially AF state whose long range order has been destroyed by the motion of doped holes.

As an alternative scenario, a pseudogap may be produced by preformed Cooper pairs, which lose their coherence above $T_c$ but still keep local pairing [92-95], or by spinon pairing which already occurs above $T_c$ [90]. However, interactions which lead to such pairing would have only small energies; that is, the energy scale of such a pseudogap should be of the same order as that of the superconducting gap ($\Delta_{\rm SC} = 10 - 20$ meV) at least in the slightly underdoped region.

Probably, the pseudogap originated from such paring interactions corresponds to the normal-state gap (low-energy pseudogap or strong pseudogap), which has been also observed in LSCO by ARPES as in Bi2212 as described in Secs. 5.3.2.5 and 5.3.4. Furthermore, such a low-energy pseudogap would be also related with the spin gap observed by NMR in underdoped YBCO[38, 39], the gap observed by tunneling spectroscopy and the drop in the electrical resistivity just above $T_c$ [54]. On the other hand, the high-energy pseudogap observed in the present work corresponds to the anomalies at high temperatures in the magnetic susceptibility, the Hall effect and the electrical resistivity. Then the question may arise whether the high-energy pseudogap and the low-energy normal-state gap or spin gap are interrelated or not. Further studies are necessary to resolve this interesting issue, which is directly related to the mechanism of superconductivity in the doped cuprates.



## 4.8 Conclusion

In conclusion, we have observed the systematic evolution of the electronic structure with hole doping in $La_{2-x}Sr_xCuO_4$. On the scale of the CT gap, the spectral weight is transferred with hole doping from the upper Hubbard band to the entire CT gap region. Around the chemical potential, we have found rather large pseudogap on the energy scale of $\sim 0.1$ eV in the total spectral DOS of $La_{2-x}Sr_xCuO_4$ by AIPES. The presented spectra have given us a clear view of the evolution of the pseudogap from the overdoped metal to the undoped insulator. Its evolution with decreasing $x$ is represented by the increase in the pseudogap energy $\Delta_{\rm PG}$ and the suppression of the spectral DOS at $\mu$, $\rho(\mu)$, as well as the quasiparticle DOS at $\mu$, $N^*(\mu)$, near the AF insulating phase. Consequently, the coherence temperature $T_F$ is much smaller than $\Delta_{\rm PG}$ in the underdoped region, suggesting that an incoherent metallic state may dominate the thermodynamic and transport properties of the underdoped cuprates. The origin of the present large pseudogap is most likely due to AF correlations or short-range AF order, while its relation to the smaller "normal-state gap" or "spin gap" remains an open question and should be addressed in future studies.

# Chapter 5

# Band Dispersion, Fermi Surface and Energy Gap in Momentum-Resolved Electronic Structure

Using angle-resolved photoemission spectroscopy (ARPES), we have studied the band dispersion, the Fermi surface, the energy gap and their doping dependences in $La_{2-x}Sr_xCuO_4$ (LSCO) for a wide hole concentration range of $0.03 \leq x \leq 0.30$. The results have revealed a dramatic change in the Fermi surface: while it is hole-like and centered at $(\pi, \pi)$ for optimally doped and underdoped samples ($x \leq 0.15$) as in other cuprates, it turns electron-like and centered at $(0, 0)$ with heavily overdoping ($x = 0.30$). On the other hand, as $x$ is decreased, the superconducting gap at $T \sim 11$ K ($2\Delta_{SC} = 18 \pm 6$ meV for $x = 0.15$) monotonically grows larger in its energy and appears to evolve continuously into a "normal-state gap" observed for $x = 0.05$ ($2\Delta_{NG} = 48 \pm 9$ meV). Remarkably, in going from the optimally doped ($x = 0.15$) to underdoped ($x = 0.10$) samples, the Fermi surface and the quasiparticle (QP) band around the Fermi level ($E_F$) vanishes in the diagonal $[(0, 0) - (\pi, \pi)]$ direction in contrast to the ARPES spectra of the underdoped $Bi_2Sr_2CaCu_2O_{8+y}$. Furthermore, in the vicinity of the superconductor-insulator transition (SIT) $x = 0.05$, two components coexists in the ARPES spectra and the spectral weight is transferred between them with $x$, suggesting a microscopic inhomogeneity around the SIT. The observations in the underdoped LSCO can be reconciled with the dynamical stripe correlations, which have been widely discussed recently. We propose how the insulator with segregated holes evolves into the superconductor with fluctuating stripes.

## 5.1 Introduction

The key issue in clarifying the nature of the high-$T_c$ cuprate systems is how the electronic structure of the $CuO_2$ plane evolves with hole doping from the antiferromagnetic insulator (AFI) to the superconductor (SC) and then to the normal metal. Indeed, for the superconductors, extensive studies using angle-resolved photoemission spectroscopy (ARPES) [12-35] have revealed band dispersions [14-23], Fermi surfaces [17-25] and superconducting and normal-state gaps [26-35] in particular for the $Bi_2Sr_2CaCu_2O_{8+y}$ (Bi2212) system. Also for undoped AFI, a band dispersion has been observed for $Sr_2CuO_2Cl_2$ [9-11]. However, the band structures of AFI and SC have distinct differences and the ARPES data have been lacking for the most interesting doping levels: the region connecting the AFI and the SC, and the region where the superconductivity disappears with heavily overdoping.

In order to reveal the missing link between the AFI and the SC, $La_{2-x}Sr_xCuO_4$ (LSCO) system is suitable because it covers continuously from the undoped AFI ($x = 0$) to the heavily overdoped limit ($x \simeq 0.30$) in a single system and the hole concentration is solely controlled by the Sr concentration $x$ when the oxygen stoichiometry is achieved by annealing. Experimental data for such a wide-ranging doping dependence of the electronic structure should be highly useful to critically check existing theories of electron correlations and the superconductivity in the $CuO_2$ plane. Indeed, for the LSCO system, the doping dependences of thermodynamic and transport properties have been revealed in the wide hole-concentration range [40, 42-47].

Moreover, the LSCO system provides several unique opportunities among the family of the high-$T_c$ cuprates. First, LSCO has a simple crystal structure with single $CuO_2$ layers. It has no Cu-O chains unlike $YBa_2Cu_3O_{7-\delta}$ (YBCO) nor complicated structural modulation of the block layers unlike Bi2212. LSCO is most likely to show the properties of the $CuO_2$ plane itself. Second, the LSCO system is particularly near the instability towards the spin-charge order in a stripe pattern [48, 49] compared to the Bi2212 system, according to recent extensive discussions based on, e.g, incommensurate peaks in inelastic neutron scattering (INS) [50, 61] and the suppression of $T_c$ at $x \simeq 1/8$. The impact of stripe fluctuations on the ARPES spectra would be clarified by investigating what is common and what is different between the LSCO and Bi2212 systems.

So far ARPES studies of LSCO have been hindered in spite of the obvious importance, probably because of the difficulty in cleaving single crystals and the surface instability compared to the extremely stable surfaces of Bi2212 under an ultra high vacuum. In the present work, we have overcome the difficulties with high-quality single crystals and careful ARPES experiments, and made a thorough investigation of the electronic band structure of LSCO covering from a heavily overdoped normal metal ($x = 0.30$) and superconductors ($x = 0.22, 0.15, 0.1$ and $0.07$) through the superconductor-insulator transition (SIT) ($x = 0.05$) down to a slightly doped insulator ($x = 0.03$).



## 5.2 Experimental

Single crystals of $La_{2-x}Sr_xCuO_4$ ($x = 0.30, 0.22, 0.15, 0.10, 0.07, 0.05$ and $0.03$) were provided by Dr. H. Eisaki, Mr. M. Takaba, Mr. T. Kakeshita, Dr. K. Tamasaku and Prof. S. Uchida (Department of Superconductivity, University of Tokyo). Details of the growth conditions and characterization are described in Refs. 70, 71 and 72. All the crystals were grown by the traveling-solvent floating-zone (TSFZ) method and annealed so that the oxygen content is stoichiometric. The accuracy of the hole concentration $\delta$ is $\pm 0.01$.

ARPES measurements were carried out at the undulator beamline 5-3 of Stanford Synchrotron Radiation Laboratory (SSRL). The experimental setup is shown in Fig. 5.1. Incident photons had energies of $h\nu = 22.4$ and 29 eV and were linearly polarized. The electric vector and the wave vector of the incident photons and the sample surface normal were kept in the same

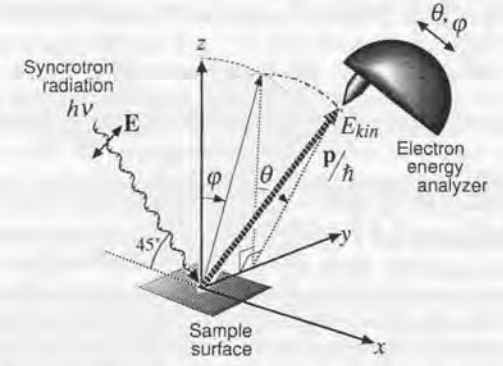


Figure 5.1: Experimental setup for the incident light, the sample surface and the electron energy analyzer.

plane as shown in Fig. 5.1. The sample was fixed with respect to the incident light with an incident angle of 45° and ARPES spectra were collected by a goniometer-mounted VSW (Vacuum Science Workshop) hemispherical analyzer of 50 mm radius. The total instrumental energy resolution including the analyzer and a monochromator was approximately 45 meV and the angular acceptance was $\sim \pm 1°$. In the case of LSCO, 1° corresponds to 1/23 and 1/19 of the $(0,0)-(\pi,0)$ distance in the Brillouin zone of the $CuO_2$ plane for the incident photon energies $h\nu = 22.4$ and 29 eV, respectively. The samples were oriented *ex situ* using Laue diffraction with an accuracy of $\sim \pm 1°$. The samples were mounted on sample holders with the surface parallel to the $CuO_2$ planes and ceramic posts were glued on the top of the samples. The samples were cleaved *in situ* with planes parallel to the $CuO_2$ planes by knocking the top-post under an ultra high vacuum better than $5 \times 10^{-11}$ Torr, which was kept during the measurements to minimize possible surface degradation. Orientation of the sample surface normal was finely readjusted using the reflection of a laser beam and the direction of the $a$- and $b$-axes were finely corrected using the band folding in the ARPES spectra with respect to the $k_y = 0$ line. Since the sample surface degraded rapidly at high temperatures, the samples were cooled down with the liquid helium flow and kept at low temperatures ($T \sim 11$ K) during the measurements. The cleanliness of the surface was checked by the absence of a hump at energy $\sim -9.5$ eV and of a shoulder of the valence band at $\sim -5$ eV. All the spectra presented here were taken within 12 hours after cleaving. The position of the Fermi level ($E_F$) was calibrated with gold spectra for every measurement and the experimental uncertainty in the energy calibration was about $\pm 2$ meV. The intensity of the spectra at different angles was normalized to the intensity of the incident light.

## 5.3 Band structure near the Fermi level

### 5.3.1 Criteria for determining Fermi-surface crossings

When a quasiparticle (QP) band crosses the Fermi level ($E_F$) in going along a line in the momentum space, two events occur concomitantly in ARPES spectra: the energy of the QP peak reaches $E_F$ and the intensity of the QP peak drops. Practically, even the QP peak right at $E_F$ is broadened due to the finite instrumental energy resolution and thus the leading edge of the QP peak is pushed above $E_F$. In previous studies, the midpoint of the leading edge reaches more than 5 meV above $E_F$ at the Fermi-surface crossing for the energy resolution of $\sim 45$ meV [29]. If an energy gap is present on the



Fermi surface, the leading-edge midpoint stays somewhat below this level ($\sim 5$ meV above $E_F$). As for the superconducting gap, it has been confirmed that the momentum where the QP energy comes the closest to $E_F$ (minimum-gap locus) coincides with the Fermi surface in the normal state [105]. On the other hand, the intensity of the QP peak may vary slowly with the momentum due to the effect of the transition-matrix elements. Note that, while the momentum dependence of the matrix elements generally change with incident photon energy $h\nu$, the Fermi-surface crossing causes a decrease in the peak intensity irrespective of the incident photon energy. Therefore, we adopt the criteria for determining the Fermi-surface crossing as follows: the momentum where most of the QP-peak intensity is lost irrespective of the incident photon energy, and concomitantly, if a clear peak exists, where the leading-edge midpoint of the QP peak reaches the maximum energy.

### 5.3.2 Angle-resolved photoemission spectra

#### 5.3.2.1 Heavily overdoped region

Figures 5.2 and 5.3 show ARPES spectra for heavily overdoped LSCO ($x = 0.30$), which shows no superconductivity. The measured crystal momenta $\mathbf{k} = (k_x, k_y)$ are referred to in units of $1/a$, where $a$ is twice of the Cu-O bond length within the $CuO_2$ plane, and the extended zone notation is adopted, that is, a $k_x$ value larger than $\pi$ means that the momentum is in the second Brillouin zone (BZ). Insets show the measured momenta (circles) and the in-plane component of the polarization of the incident photons (arrows).

Along the $(0,0) \rightarrow (\pi,0)$ cut, a clear band dispersion is observed as shown in Figs. 5.2 (a) and (b). The quasiparticle (QP) peak near $E_F$ has almost the same width as that of overdoped Bi2212 under the same energy resolution [15, 17, 18, 29, 98]. When one goes from $(0,0)$ to $(\pi,0)$ or from $(2\pi,0)$ to $(\pi,0)$, the energy of the QP peak moves upwards, reaches $E_F$ around $\sim (0.8\pi,0)$ or $\sim (1.2\pi,0)$, then the peak intensity decreases and almost disappears by $(\pi,0)$. Note that the distinct QP peak at $\sim (1.2\pi,0)$ has the leading edge whose midpoint is $\sim 6$ meV above $E_F$. Therefore, a Fermi-surface crossing occurs around $(0.8\pi,0)$ for $x = 0.30$.

While the QP peaks in the first and second BZ have the identical dispersion, their intensity is enhanced around $\sim (1.2\pi,0)$ probably because of the effect of the transition-matrix elements as seen in the other compositions [Figs. 5.5(a) and 5.6(b)]. Indeed it has also been observed for other cuprates [16] that the peak intensity differs between the first and second BZ. Nevertheless, it is difficult to explain with the matrix-element effect that the peak

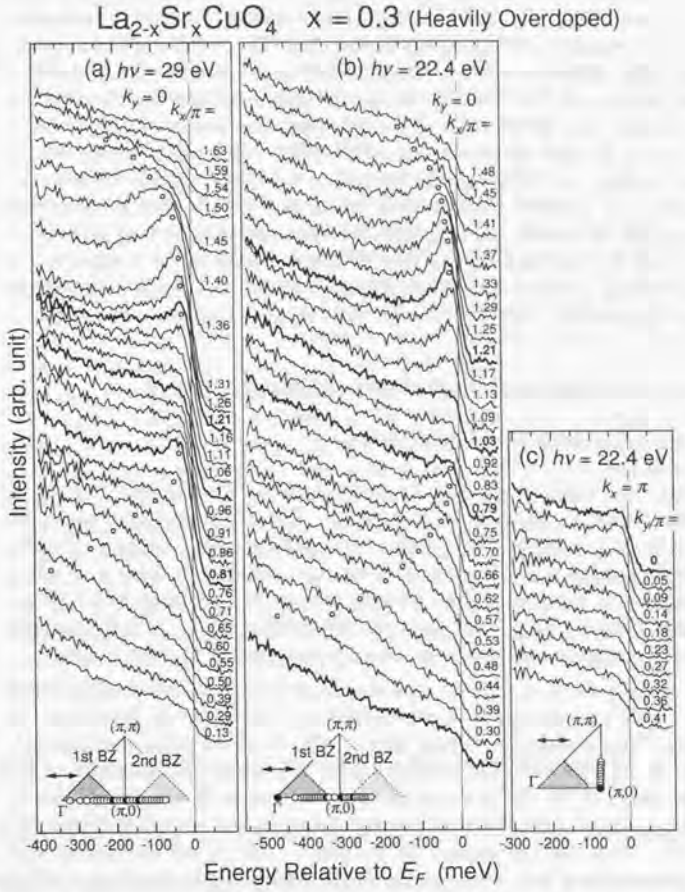


Figure 5.2: ARPES spectra near the Fermi level for heavily overdoped $La_{2-x}Sr_xCuO_4$ ($x = 0.30$), which shows no superconductivity. Insets show the measured momenta in the Brillouin zone (circles) and the in-plane component of the polarization of the incident photons (arrows). The band crosses the Fermi surface around $(0.8\pi, 0)$.



intensity decreases not only for $(1.2\pi, 0) \rightarrow (\pi, 0)$ but also for $(0.8\pi, 0) \rightarrow (\pi, 0)$ both in the spectra taken at $h\nu = 29$ eV [Fig. 5.2(a)] and at $h\nu = 22.4$ eV [Fig. 5.2(b)], unless a Fermi-surface crossing occurs around $(0.8\pi, 0)$.

ARPES spectra taken along $(\pi, 0) \rightarrow (\pi, \pi)$ are shown in Fig. 5.2(c). It appears that the intensity slightly decreases in going from $(\pi, 0)$ to $(\pi, \pi)$, indicating that a small part of the QP peak weight remains below $E_F$ around $(\pi, 0)$. Probably, the dispersion is quite slow around $(\pi, 0)$ as reported for other cuprates [15, 17-21] and thus the QP band stays only slightly above $E_F$ even at $(\pi, 0)$. Note that, in the presence of strong electron correlation, the QP peak is no more a single peak and therefore part of the spectral weight is distributed on the other side of the Fermi level. Comparing the spectra along the $(0, 0) \rightarrow (\pi, 0)$ and $(\pi, 0) \rightarrow (\pi, \pi)$ cuts, one finds that the most part of the QP weight goes above $E_F$ at $\sim (0.8\pi, 0)$ in going along $(0.0) \rightarrow (\pi, 0) \rightarrow (\pi, \pi)$.

As shown in Fig. 5.3, the intensity of the QP peak near the Fermi surface decreases in going from $\sim (0.8\pi, 0)$ towards $(\pi/2, \pi/2)$. Although the peak is not clearly identified along the $(0, 0) \rightarrow (\pi, \pi)$ cut [Fig. 5.3(c)], the edge intensity slightly increases at $\sim (0.38\pi, 0.38\pi)$ and then drops by $\sim (0.44\pi, 0.44\pi)$,

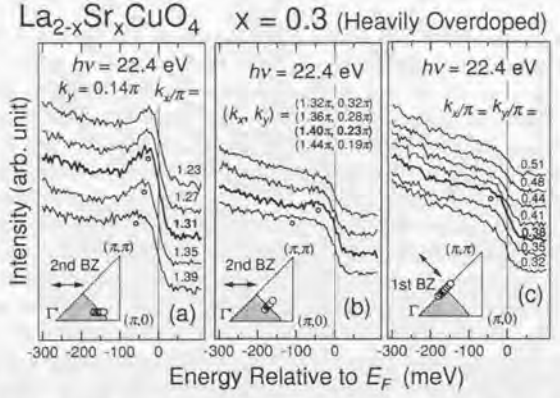


Figure 5.3: ARPES spectra of heavily overdoped $La_{2-x}Sr_xCuO_4$ ($x = 0.3$) near the Fermi level. Insets show the measured momenta in the Brillouin zone (circles) and the in-plane component of the polarization of the incident photons (arrows).

suggesting a Fermi-surface crossing. This small variation in intensity was reproduced in several measurements for both the incident photons of $h\nu = 22.4$ and 29 eV. The QP peak near $(\pi/2, \pi/2)$ is considerably weak and broad compared to the peak around $(\pi, 0)$, while other cuprates show clear QP peaks around $(\pi/2, \pi/2)$ [9-11, 14-19, 21, 29, 34, 35, 98].

#### 5.3.2.2 Overdoped region

Figure 5.4 shows ARPES spectra for overdoped LSCO ($x = 0.22$) in the superconducting state. In going from $(0,0)$ to $(\pi,0)$ or from $(2\pi,0)$ to $(\pi,0)$ [Fig. 5.4(a)], the peak energy moves upwards and reaches around $E_F$ near $(\pi,0)$. However, certain part of the QP weight appears to remain at $(\pi,0)$ in Figs. 5.4(a) and (b). Under the present experimental uncertainties, the QP band is too flat around $(\pi,0)$ to distinguish whether the Fermi-surface crossing is in the $(0,0) \rightarrow (\pi,0)$ cut or in the $(\pi,0) \rightarrow (\pi,\pi)$ cut. Again the dispersive feature in the $(0,0) \rightarrow (\pi,\pi)$ cut is broad and weak as in $x = 0.3$, while a slight intensity variation suggests a Fermi-surface crossing around $\sim (0.4\pi, 0.4\pi)$.

#### 5.3.2.3 Optimally doped region

Figure 5.5 shows ARPES spectra for optimally doped LSCO ($x = 0.15$) in the superconducting state. As one goes from $(0,0)$ to $(\pi,0)$ or from $(2\pi,0)$ to $(\pi,0)$ [Fig. 5.5(a)], the QP peak approaches $E_F$ but the peak remains distinctly below $E_F$ until $\sim (\pi,0)$. Furthermore, the leading-edge midpoint of the QP peak is always below $E_F$ along the $(0,0) - (\pi,0) - (2\pi,0)$ cut, e.g., $-7$ meV at $\sim (\pi,0)$. Therefore, there is no Fermi-surface crossing in the $(0,0) - (\pi,0)$ direction for $x = 0.15$. While the peak intensity is enhanced around $(1.2\pi,0)$ as in $x = 0.3$ [Fig. 5.2(b)], the QP peak loses no intensity in going from $(0.8\pi,0)$ to $(\pi,0)$ in the first BZ for $x = 0.15$ unlike for $x = 0.3$. In going from $(\pi,0)$ to $(\pi,\pi)$ [Fig. 5.5(b)], the peak intensity decreases around $\sim (\pi, 0.1\pi)$, while the leading-edge midpoint stays below $E_F$ ($-3$ meV at the closest to $E_F$, i.e., the minimum-gap locus). This implies that the QP band goes above $E_F$ through the superconducting gap. The spectra along $(0,0)$ to $(\pi,\pi)$ for $x = 0.15$ are similar to those for $x = 0.3$ and 0.22. Although the QP peak is weak, one can identify the band dispersion of a broad QP peak crossing $E_F$ around $\sim (0.4\pi, 0.4\pi)$.



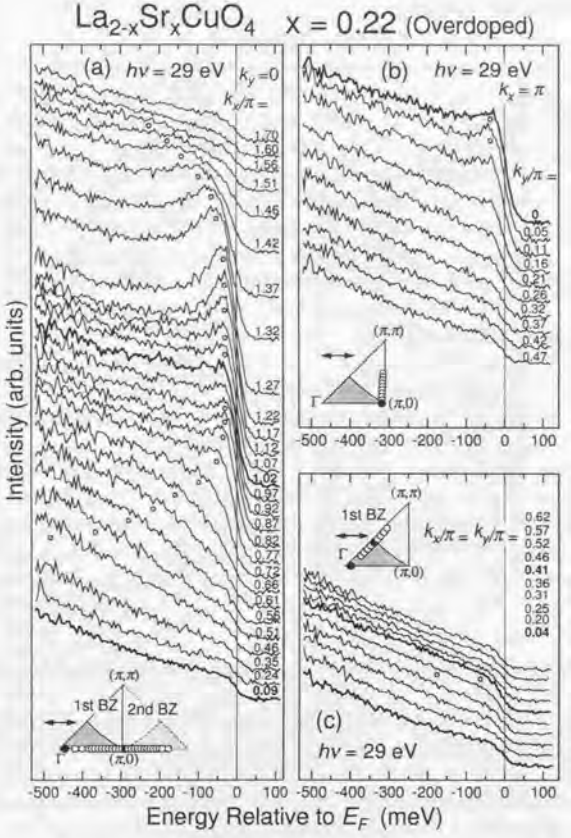


Figure 5.4: ARPES spectra near the Fermi level for overdoped $La_{2-x}Sr_xCuO_4$ ($x = 0.22$). Insets show the measured momenta in the Brillouin zone (circles) and the in-plane component of the polarization of the incident photons (arrows). The band crosses the Fermi surface in the vicinity of $(\pi,0)$ with a quite slow dispersion.

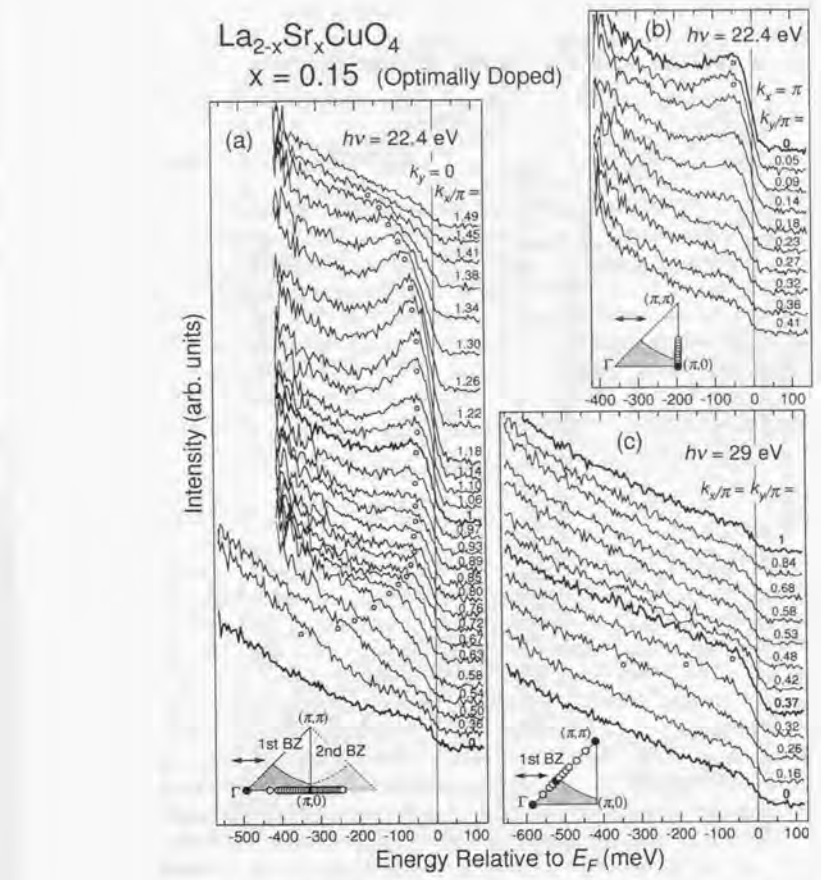


Figure 5.5: ARPES spectra near the Fermi level for optimally doped $La_{2-x}Sr_xCuO_4$ ($x = 0.15$). Insets show the measured momenta in the Brillouin zone (circles) and the in-plane component of the polarization of the incident photons (arrows). The band appears to go above $E_F$ through the superconducting gap on the Fermi surface between $(\pi, 0)$ and $(\pi, 0.2\pi)$.



#### 5.3.2.4 Underdoped region

Figures 5.6 and 5.7 show ARPES spectra for underdoped LSCO ($x = 0.1$ and 0.07, respectively) in the superconducting state. The QP peak around $(\pi, 0)$ is considerably broadened for the underdoped LSCO as in other underdoped cuprates [11, 17, 24, 29, 31, 32, 34, 98]. Nevertheless, the dispersion of the QP band is observed as shown in Figs. 5.6(a), 5.6(b) and 5.7(a). In going from $(0, 0)$ to $\sim (0.8\pi, 0)$ or from $(2\pi, 0)$ to $\sim (1.2\pi, 0)$ the peak approaches $E_F$, and then it stays below $E_F$ until $(\pi, 0)$, where the leading-edge midpoint is about $\sim -17$ meV for $x = 0.1$ and 0.07. Obviously the QP band is below $E_F$ at $(\pi, 0)$. While the spectra taken at $h\nu = 22.4$ eV [Fig. 5.6(b)] show the enhancement in the peak intensity around $(1.2\pi, 0)$, the spectra taken at $h\nu = 29$ eV [Figs. 5.6(a) and 5.7(a)] shows almost no enhancement around $(1.2\pi, 0)$, indicating that the intensity variation between $(\pi, 0)$ and $(1.2\pi, 0)$ for $h\nu = 22.4$ eV is not due to a Fermi-surface crossing but due to the matrix-element effect. On the other hand, as one goes from $(\pi, 0)$ towards $(\pi, \pi)$ [Figs. 5.6(c) and 5.7(b)], the broad peak and its leading edge further approach $E_F$ and then the peak disappears, implying that the band goes above $E_F$ around $\sim (\pi, 0.2\pi)$. The leading-edge midpoint is about $\sim -8$ meV at the closest to $E_F$ for $x = 0.1$ and 0.07. This energy gap at $E_F$ should be assigned to the superconducting gap because the measurements were done in the superconducting state. Therefore, we may conclude that the band crosses an underlying Fermi surface around $\sim (\pi, 0.2\pi)$ [105]. As for the $(0, 0) \rightarrow (\pi, \pi)$ cut [Figs. 5.6(c) and 5.7(c)], no QP peak is identified in the spectra.

#### 5.3.2.5 Vicinity of the superconductor-insulator transition

Figure 5.8 shows the ARPES spectra of LSCO for $x = 0.05$. Since the superconductor-insulator transition is around $x = 0.05$, $T_c$ is almost zero or absent for this sample. Although the QP peak near $E_F$ is further broadened and weakened, the momentum-dependence of the dispersive feature is still identified. The band dispersion near $E_F$ for $x = 0.05$ is qualitatively similar to that for $x = 0.07, 0.10$ and 0.15: in going along $(0, 0) \rightarrow (\pi, 0) \rightarrow (\pi, \pi)$, the QP peak comes near $E_F$ ($\sim 100$ meV) at $\sim (0.8\pi, 0)$, stays there in $(0.8\pi, 0) \rightarrow (\pi, 0)$, then further approaches $E_F$ and disappears between $(\pi, 0)$ and $(\pi, \pi)$. Here, the energy of the leading-edge midpoint is $\sim -48$ meV at $\sim (\pi, 0)$ and $\sim -18$ meV at the closest to $E_F$, i.e., at $\sim (\pi, 0.25\pi)$. Figure 5.8(b) exhibits that a reminiscent of the superconducting gap is present even for $x = 0.05$, consistent with the "normal-state gap" observed for the underdoped Bi2212 [29-33].

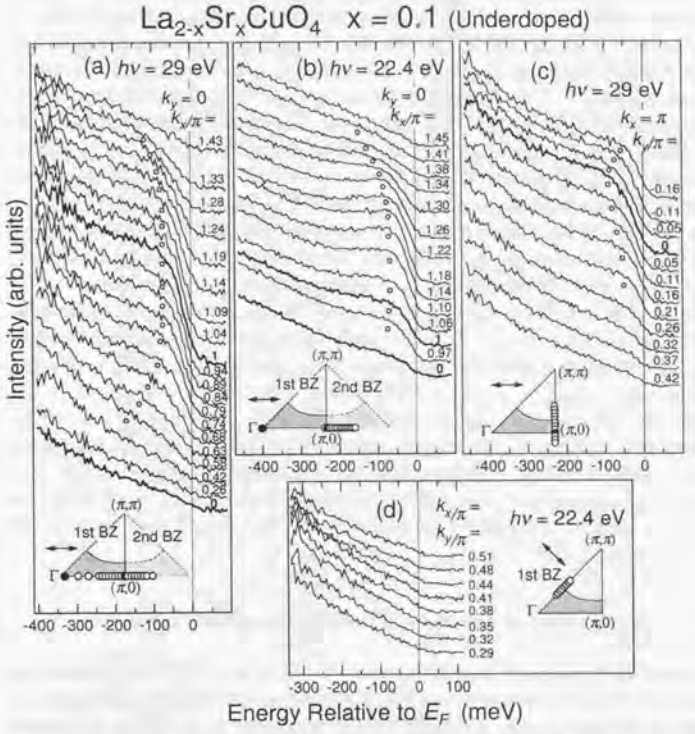


Figure 5.6: ARPES spectra near the Fermi level for underdoped $La_{2-x}Sr_xCuO_4$ ($x = 0.10$). Insets show the measured momenta in the Brillouin zone (circles) and the in-plane component of the polarization of the incident photons (arrows). The band appears to go above $E_F$ through the superconducting gap on the Fermi surface around $(\pi, 0.2\pi)$.



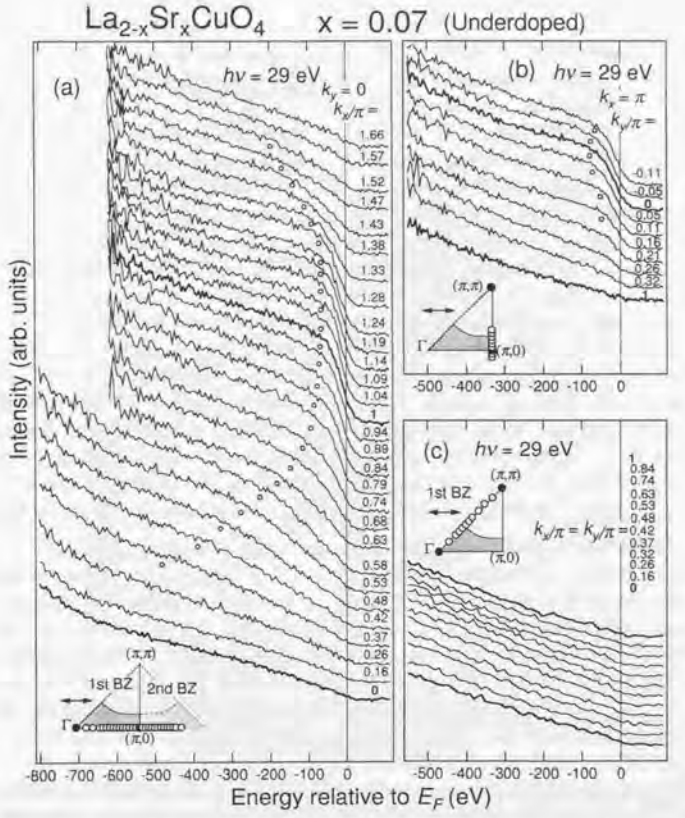


Figure 5.7: ARPES spectra near the Fermi level for underdoped $La_{2-x}Sr_xCuO_4$ ($x = 0.07$). Insets show the measured momenta in the Brillouin zone (circles) and the in-plane component of the polarization of the incident photons (arrows). The band appears to go above $E_F$ through the superconducting gap on the Fermi surface around $(\pi, 0.2\pi)$.

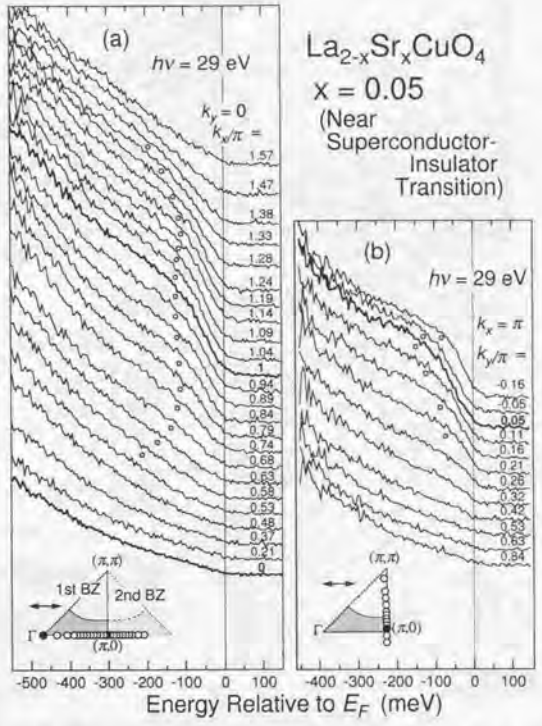


Figure 5.8: ARPES spectra near the Fermi level for $La_{2-x}Sr_xCuO_4$ around the superconductor-insulator transition ($x = 0.05$). Insets show the measured momenta in the Brillouin zone (circles) and the in-plane component of the polarization of the incident photons (arrows). The band appears to go above $E_F$ through the "normal-state gap" on the Fermi surface around $(\pi, 0.25\pi)$.



### 5.3.3 Fermi surface

Comparing the ARPES spectra for $x = 0.15$ [Figs. 5.5(a) and (b)] and $x = 0.3$ [Figs. 5.2(b) and (c)], the peak intensity around $(\pi, 0)$ is strikingly depressed for $x = 0.3$, indicating that most part of the QP weight is above $E_F$ at $(\pi, 0)$ for $x = 0.3$. Furthermore, the midpoint of the leading edge reaches about 6 meV above $E_F$ at $\sim (1.2\pi, 0)$ for $x = 0.3$, while for the underdoped LSCO ($x \leq 0.15$) and other cuprates [17, 24, 20, 23, 29, 31, 34, 35], the leading-edge midpoint is always sufficiently below $E_F$ along the $(0, 0) - (\pi, 0)$ direction. Therefore, it is concluded that the Fermi surface of LSCO undergoes a drastic change from a hole-like Fermi surface centered at $(\pi, \pi)$ for $x = 0.15$ into an electron-like one centered at $(0, 0)$ for $x = 0.3$. So far, hole-like Fermi surfaces have been observed in other cuprates such as Bi2212 (Fig. 2.5) [17, 18, 24], $Bi_2Sr_2CuO_{6+y}$ (Bi2201) [19], YBCO [22] and $Nd_{2-x}Ce_xCuO_4$ [23, 25]. The present observation manifests that the hole-like Fermi surface may turn into the electron-like one when the $CuO_2$ plane is as heavily overdoped as $x = 0.3$. The change in the Fermi-surface topology may correspond to the fact that the sign of the Hall coefficient turns from positive to negative around $x = 0.25$ with hole doping in LSCO [106, 107]. The same trend of the change in the Fermi-surface topology has been expected from the local-density-approximation (LDA) band structure of undoped $La_2CuO_4$ by shifting the Fermi level within the rigid band model [84, 108].

The Fermi surfaces (or minimum-gap loci) deduced from the ARPES spectra are shown in Fig. 5.9. Error bars denote the observed Fermi-surface crossings. The areas enclosed by the Fermi surfaces are $71 \pm 3$, $79 \pm 8$ and $85 \pm 5\%$ of the half BZ area for $x = 0.3$, 0.22 and 0.15, respectively, and consistent with the Luttinger sum rule if the electron density is $1-x$ ($= 70, 78$ and 85%, respectively). Thus the result supports the "large Fermi surface" picture rather than the small hole pockets centered at $(\pi/2, \pi/2)$. For $x = 0.1$ and 0.05, the Fermi surface around $(\pi/2, \pi/2)$ is not identified (dotted curve) because the QP band near $E_F$ is invisible there for LSCO unlike the underdoped Bi2212 [9-11, 17, 29, 98]. The issue of the disappearance of the Fermi surface and the QP band around $(\pi/2, \pi/2)$ will be discussed in Sec. 5.4.2.

According to the ARPES result [Fig. 5.9(a)], the Fermi surface for $x = 0.3$ seems to be almost square and have a large straight portion around $(\pi/2, \pi/2)$. Recently, the Fermi-surface nesting [90] and short-range stripe order [50] have been proposed as the origin of the incommensurate peaks in the dynamical magnetic structure factor $S(\mathbf{q}, \omega)$ observed by inelastic neutron scattering for LSCO (Fig. 2.11). However, in the presence of the straight

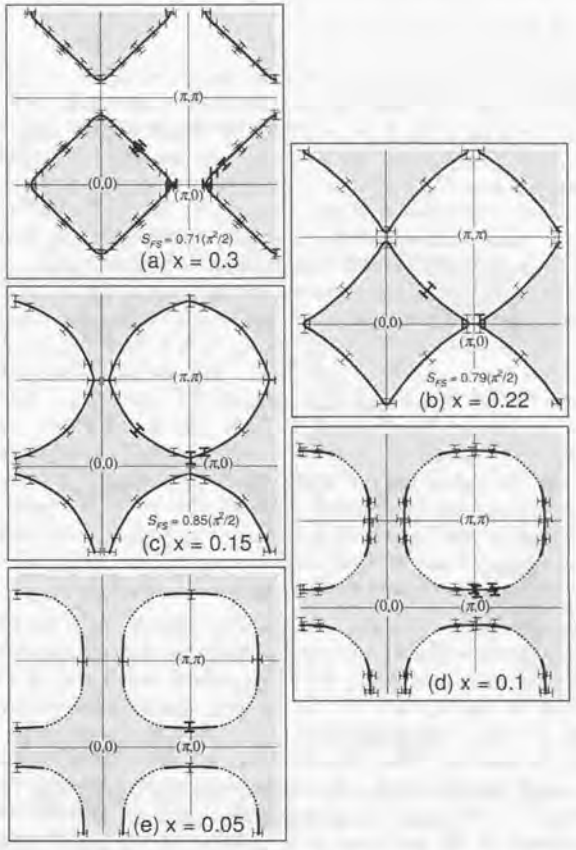


Figure 5.9: Fermi surfaces (or minimum-gap loci) of $La_{2-x}Sr_xCuO_4$, obtained from ARPES experiments. The observed Fermi-surface crossings are indicated by thick error bars. Thin error bars denote Fermi-surface crossings folded by symmetry. As for $x = 0.10$ and 0.05, since no dispersive features are observed near $E_F$ around $(\pi/2, \pi/2)$, the dotted curves are tentatively drawn there so that the area enclosed by the Fermi surface is $\sim 0.9$ and $\sim 0.95$, respectively, of the half BZ area. As $x$ decreases, the electron-like Fermi surface centered at $(0,0)$ for $x = 0.30$ turns into the hole-like one centered at $(\pi,\pi)$ for $x = 0.15$.



Fermi surface for $x = 0.3$, it is difficult to explain within the picture of the Fermi-surface nesting why the incommensurate peaks are smeared out in the overdoped region ($x > 0.25$) as reported recently [60].

### 5.3.4 Energy gap

The magnitude of the energy gap at $E_F$ may be estimated from the leading-edge shift of the QP peak on the Fermi surface [27-32, 34, 35]. Figure 5.10(a) shows the ARPES spectra at the momenta where the leading edge comes to the maximum energy (minimum-gap locus) around $(\pi, 0)$ as shown by open circles in the inset. From the ARPES spectrum for each composition, the spectrum at $(0, 0)$ has been subtracted as the angle-independent background. For the non-superconducting sample ($x = 0.3$), the leading-edge midpoint is pushed above $E_F$ ($\sim 6$ meV) due to the finite instrumental resolution ($\sim 45$ meV) [29]. As the hole concentration decreases, the energy of the QP peak and its leading edge are shifted downwards as a result of the opening of the superconducting gap.

In Fig. 5.10(b), the energy shift of the leading-edge midpoint relative to that for $x = 0.3$, $\Delta$, are plotted and compared with the magnitude of the superconducting gap deduced from other experiments on LSCO, i.e., Raman scattering [110], tunneling [54] and neutrons [59] results (left axis). Crosses indicate the superconducting transition temperature $T_c$ (right axis) and the prediction of the mean-field theory for the $d$-wave superconductor $2\Delta_{SC}^{MF} = 4.3 k_B T_c$ [109] (left axis). The experiments including ARPES are roughly consistent with each other in the magnitude of the gap and its doping dependence. Here the leading-edge shift tends to underestimate the energy gap compared to the other experiments. This is because the intrinsic broadness of the QP peak reduces the shift of the leading edge observed by ARPES, while it hardy affect the peak position such as observed in other experiments.

As the hole concentration $x$ decreases, the magnitude of the superconducting gap $\Delta$ keeps increasing even for the underdoped LSCO in spite of the decreasing $T_c$. This remarkable feature has also been reported for Bi2212 [30] and is thus likely to be universal among the cuprate superconductors. Note that the doping dependence of the superconducting and normal-state gaps $\Delta$ observed by the leading-edge shift is quite similar to that of the high-energy pseudogap $\Delta_{PG}$, even though their energy scales are different. Since the high-energy pseudogap $\Delta_{PG}$ is associated with the antiferromagnetic correlations in Chapter 4, the similar doping dependences may imply that these gaps have the same origin. The relation between the antiferromagnetic cor-

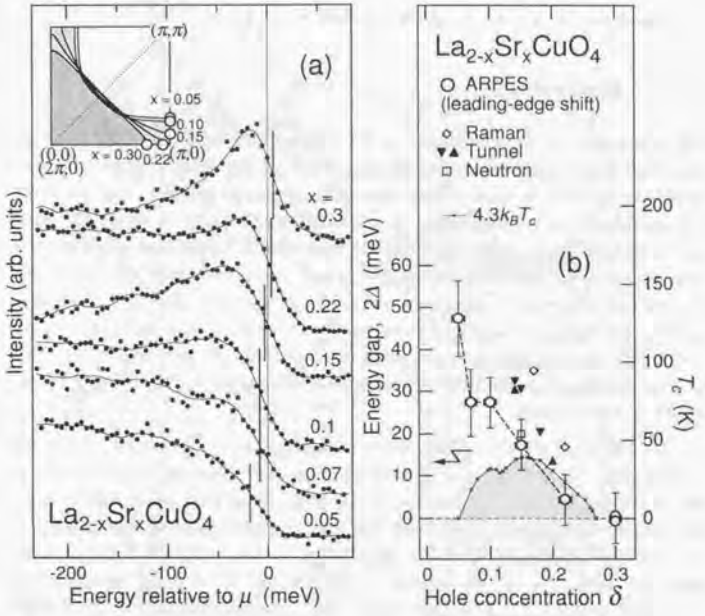


Figure 5.10: (a) ARPES spectra for momenta on the Fermi surface (minimum-gap locus) near $(\pi, 0)$ as denoted by open circles in the inset. From the ARPES spectrum for each composition $x$, the spectrum at $(0, 0)$ has been subtracted as the angle-independent background. (b) Relative shift $\Delta$ in the leading-edge midpoint of the ARPES spectra, denoted by open circles. The leading-edge shift $\Delta$ approximately represents the magnitude of the superconducting ($\Delta_{SC}$) and normal-state ($\Delta_{NG}$) gaps and is compared with the gap deduced from the $d$-wave mean-field approximation $2\Delta_{SC}^{MF} = 4.3k_BT_c$ (crosses) [109] and other experiments: Raman scattering (open diamonds) [110], scanning tunnel spectroscopy (filled triangles) [54], and inelastic neutron scattering (open boxes) [59]. As $\delta$ decreases, the magnitude of energy gap keeps increasing even for the underdoped LSCO in spite of the decreasing $T_c$.



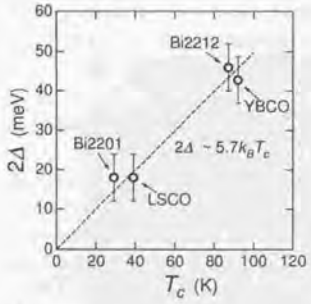


Figure 5.11: Relation between $T_c$ and the superconducting gaps $\Delta$ for various optimally doped cuprates, LSCO (present study), Bi2212 [32], Bi2201 [34] and YBCO [35]. The magnitude of the superconducting gap has been derived from the leading-edge shift $\Delta$ in the ARPES spectra.

relations and the superconductivity should be crucial issue to understand the mechanism of the high-$T_c$ superconductivity [111].

Even for the sample of $x = 0.05$ in the normal state ($T \sim 11$ K $> T_c \sim 0$ K), a similar energy gap remains open on the underlying Fermi surface at $\sim (\pi, 0.25\pi)$ as shown in Fig. 5.8(b), corresponding to the "normal-state gap" observed for Bi2212 [29-33]. In the present ARPES results [Figs. 5.8(b) and 5.10(b)], it appears that the superconducting gap continuously evolves into the normal-state gap with decreasing hole concentration $x$ in the same way as with increasing temperature $T$ [30, 32, 33].

Figure 5.11 shows the relation between $T_c$ and the superconducting gaps $\Delta$ for various optimally doped cuprates. Here, the magnitude of the superconducting gap has been derived from the leading-edge shift $\Delta$ in the ARPES spectra [32, 34, 35]. The magnitude of the superconducting gap $\Delta$ scales well with transition temperature $T_c$. For the optimally doped cuprates, the scaling factor $2\Delta/k_BT_c \sim 5.7 \pm 1$ appear to be somewhat larger than the prediction of the mean-field theory 4.3 [109], although it is within the experimental uncertainty for LSCO alone. Note that the systems with single $CuO_2$ planes, i.e., LSCO and Bi2201 are similar in the magnitude of the superconducting gap $\Delta$ and the maximum $T_c$.

### 5.3.5 Band dispersion

Band dispersion around $(\pi, 0)$ is quite slow, as observed for $x \leq 0.15$ [Figs. 5.5(a), 5.6(a), 5.6(b), 5.7(a) and 5.8(a)]. Thus, as in other cuprates [15, 17-21] (Fig. 2.5), LSCO system also has an extended saddle point singularity at $(\pi, 0)$, i.e., so-called "$(\pi, 0)$ flat band," suggesting that it is a feature universal to the hole-doped $CuO_2$ plane. The presence of the flat band around

$(\pi, 0)$ may be expected even for the overdoped LSCO ($x = 0.22$ and 0.30) because the intensity decrease due to the Fermi-surface crossing near $(\pi, 0)$ is considerably slow [Figs. 5.2(a), 5.2(b) and 5.4(a)].

Band mapping has been performed by taking the second derivatives of the ARPES spectra and the obtained band structure is denoted by the gray scale plot and the black curves in Fig. 5.12. Note that, because of the finite instrumental resolution $E_{\rm res} \sim 45$ meV, the structure near $E_{\rm F}$ are pushed down approximately below the resolution limit $E \lesssim -E_{\rm res}/2$ (dashed line). Then, the momenta and energies at the minimum-gap locus is consistent with the obtained Fermi surfaces in Fig. 5.9 and the doping dependence of the energy gap in Fig. 5.10. The band dispersion for optimally doped LSCO ($x = 0.15$) is quite similar to those for other optimally doped cuprates such as Bi2212 (Fig. 2.5) [17] and Bi2201 systems [19].

The doping dependence of the flat band around $(\pi, 0)$ may be related with the superconductivity. The flat band is at a distance of $\sim 100$ meV from $E_{\rm F}$ around the SIT ($x = 0.05$), approaches $E_{\rm F}$ as $T_c$ increases with hole doping in the underdoped region, and comes just below $E_{\rm F}$ exactly for the optimally doped ($x = 0.15$) LSCO. As $T_c$ decreases with further hole doping in the overdoped region, the flat band partly goes above $E_{\rm F}$ and, upon the disappearance of $T_c$ with heavily overdoping ($x = 0.3$), the most of the flat band goes above $E_{\rm F}$ with small QP weight remaining below $E_{\rm F}$. As a result, the topology of the Fermi surface is turned over. It is notable that also for the Bi2212 system the flat band comes just below $E_{\rm F}$ for the optimally doped sample (Fig. 2.5) [17]. The presence of the extended flat band around $(\pi, 0)$ and the trend on which the flat band energy is shifted with hole doping agree with the results of the numerical studies on the Hubbard model [99, 104]. The band around $(\pi, 0)$ should be responsible for the superconductivity, because without QP band weight near $E_{\rm F}$ around $(\pi/2, \pi/2)$ the superconductivity occurs for the underdoped LSCO ($x = 0.10$ and 0.07). These observations are also consistent with the picture that the extended van Hove singularity near $E_{\rm F}$ explains the high-$T_c$ superconductivity [52].

The inverse of the dispersion rate at the Fermi surface $(dE(k)/dk|_{E=E_{\rm F}})^{-1}$ is directly related to quasiparticle DOS at $E_{\rm F}$, $N^*(E_{\rm F})$, and quasiparticle mass $m^*$. Since $(dE/dk|_{E=E_{\rm F}})^{-1}$ is small near $(\pi/2, \pi/2)$ [Fig. 5.12(c)], $dE/dk|_{E=E_{\rm F}}$ near $(\pi, 0)$ represents the main part of $N^*(E_{\rm F}) \propto m^*$. As the flat band approaches $E_{\rm F}$ in going from $x = 0.05$ to $x = 0.15$, the dispersion rate along $(\pi, 0) \rightarrow (\pi, 0.2\pi)$ becomes quite slower. When the flat band has almost gone above $E_{\rm F}$ for $x = 0.3$, a finite dispersion rate is recovered at the Fermi-surface crossing $\sim (0.8\pi, 0)$. In Fig. 5.13, $(dE/dk|_{E=E_{\rm F}})^{-1}$ along $(0, 0) \rightarrow (\pi, 0) \rightarrow (\pi, \pi)$ deduced from Fig. 5.12 is compared with the electronic



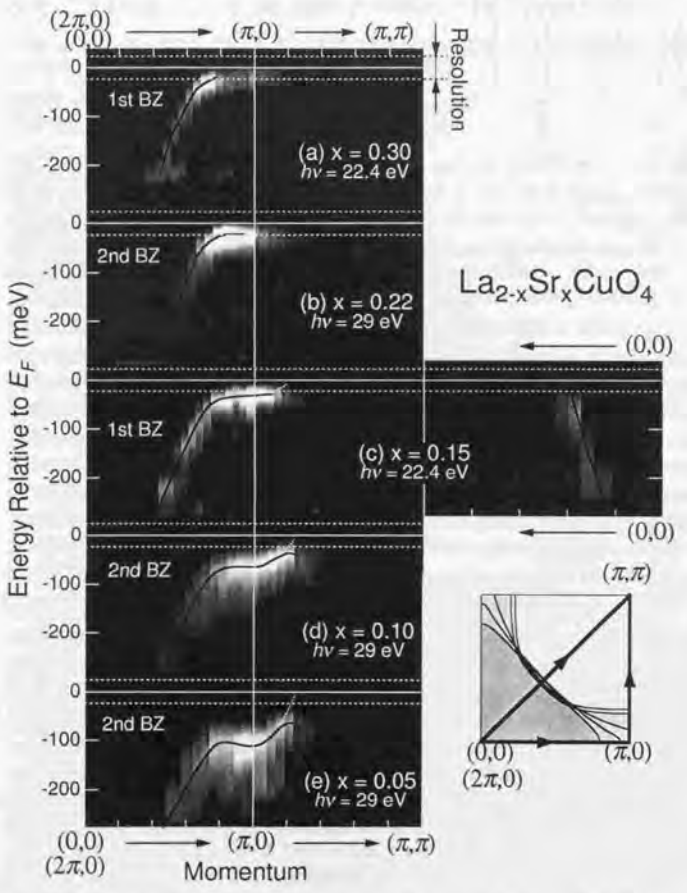


Figure 5.12: Band dispersion of $La_{2-x}Sr_xCuO_4$ near the Fermi level $E_{\rm F}$ measured by ARPES. The second derivatives of the ARPES spectra are plotted on the gray scale. Before taking the derivatives, the spectrum at $(0, 0)$, which is assumed to represent the angle-independent background, was subtracted from the ARPES spectra for each composition. Note that, because of the finite instrumental resolution $E_{\rm res} \sim 45$ meV, the structure near $E_{\rm F}$ are pushed down approximately below the resolution limit $E \lesssim -E_{\rm res}/2$ (dashed line).

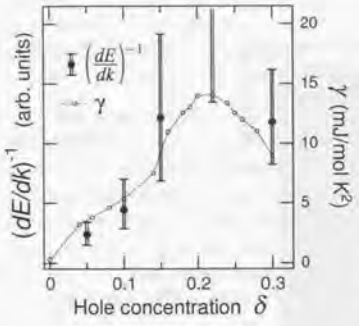


Figure 5.13: Inverse of the dispersion rate $(dE(k)/dk|_{E=E_F})^{-1}$ at the Fermi-surface crossing along $(0,0) \rightarrow (\pi,0) \rightarrow (\pi,\pi)$, (filled circles), which represents the contribution of the band around $(\pi,0)$ to the quasiparticle DOS at $E_F$, $N^*(E_F) \propto m^*$. Open circles denote the electronic specific heat coefficient $\gamma = \frac{1}{3}\pi^2 k_B^2 N^*(E_F) \propto m^*$ [47].

specific heat coefficient $\gamma = \frac{1}{3}\pi^2 k_B^2 N^*(E_F) \propto m^*$ [47]. As for $x = 0.15, 0.1$ and 0.05, $dE/dk|_{E=E_F}$ are derived from hypothetical band dispersions which would be present if there were no energy gaps as denoted by white dotted curves in Fig. 5.12, where the hypothetical dispersions are drawn by interpolating between the band around $(\pi,0)$ and the Fermi-surface crossing as a cosine curve. The general doping dependence of $(dE/dk|_{E=E_F})^{-1}$ near $(\pi,0)$ agrees with that of $\gamma$, indicating that $m^* \propto N^*(E_F)$ indeed diminishes in going from the superconductor towards the AFI ($x \sim 0$) as the flat band is lowered away from $E_F$.

In the ARPES spectra of LSCO [Figs. 5.2(a), 5.2(b), 5.4(a), 5.5(a), 5.6(a), 5.6(b), 5.7(a) and 5.8(a)], the QP peak around $(\pi,0)$ is gradually broadened as the hole concentration $x$ decreases. This broadening is not due to extrinsic origins such as the quality of cleaved surfaces but rather intrinsic to the $CuO_2$ planes, because the cleaved surfaces were flatter for the underdoped crystals ($x = 0.05$, 0.07 and 0.1) than for the overdoped crystals ($x = 0.3$, 0.22) in the present experiments, probably reflecting the stronger two-dimensionality of the underdoped LSCO [70, 112, 113]. The present observations of the QP peak width at $\sim (\pi,0)$, the energy of the flat band and their doping dependences for LSCO are consistent with the trend observed for the Bi2212, Bi2201 and $Sr_2CuO_2Cl_2$ systems and that for the $t$-$t'$-$t''$-$J$ model calculations [11, 17, 34, 98]. According to the discussion in Ref. 11 based on the $t$-$t'$-$t''$-$J$ model calculation, the broadening for the QP peaks at $\sim (\pi,0)$ and the lowering of the flat band away from $E_F$ are likely originated from the development of antiferromagnetic correlations in the underdoped $CuO_2$ plane.



## 5.4 Transition of the electronic structure from the superconductor to the insulator

### 5.4.1 Two spectral components

Figure 5.14(a) shows the doping dependence of the ARPES spectrum at $(\pi,0)$ taken in a wider energy range ($E \geq -1$ eV) than that in the previous section (Sec. 5.3). The QP peak is just below $E_F$ and relatively sharp for the optimally doped sample ($x = 0.15$), and it is broadened and shifted downwards for the underdoped samples ($x = 0.10$ and 0.07). When the hole concentration is further decreased to the vicinity of the SIT ($x = 0.05$), the QP peak near $E_F$ rapidly loses its intensity and concomitantly another broad feature appears around $-0.55$ eV. In the insulating phase ($x = 0.03$), the peak near $E_F$ almost disappears while the structure at $\sim -0.55$ eV grows into a distinct peak. Figure 5.14(b) demonstrates that spectral weight is

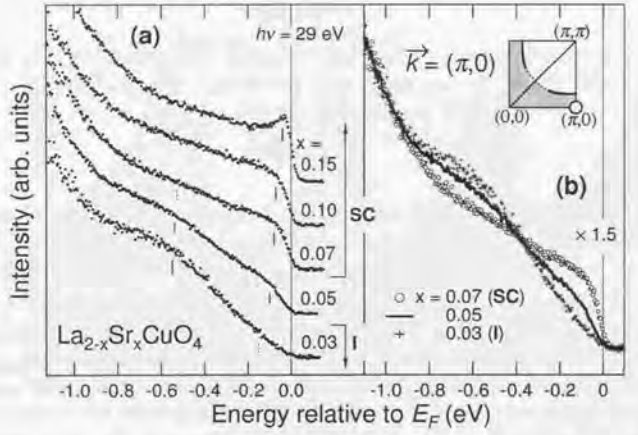


Figure 5.14: (a) Doping dependence of the ARPES spectrum at $\mathbf{k} = (\pi,0)$, showing two spectral features marked by the vertical bars in the vicinity of the superconductor-insulator transition (SIT) of $La_{2-x}Sr_xCuO_4$ ($x \sim 0.05$). $x = 0.10$ and 0.07 are underdoped superconductors (SC) and $x = 0.03$ is an insulator (I). (b) Overlaid spectra demonstrating the transfer of spectral weight between the two components in the vicinity of the SIT ($x \sim 0.05$). Inset shows the Fermi surface of the underdoped $La_{2-x}Sr_xCuO_4$.

transferred between the two features rather than that a single peak is shifted continuously from the AFI to the SC as in Bi2212 [114].

On the other hand, ARPES spectra in the $(0,0) \rightarrow (\pi,\pi)$ direction show another doping dependence as shown in Fig. 5.15. For the optimally doped sample ($x = 0.15$), although the dispersive feature is considerably broad and weak, one can identify a band crossing $E_F$ around $(0.4\pi, 0.4\pi)$. For the underdoped samples ($x = 0.10$ and 0.07), the dispersive band is invisible around $E_F$, while a faint structure may be found at $\sim -0.45$ eV around $(\pi/2, \pi/2)$. It is remarkable that, even though the system is a SC, the band crossing $E_F$ is absent in the $(0,0) \rightarrow (\pi,\pi)$ direction for $x = 0.10$ and 0.07. In the insulating sample ($x = 0.03$), the band at $\sim -0.45$ eV around $(\pi/2, \pi/2)$ becomes distinct, correlated with the growth of the broad structure around $(\pi, 0)$ at $\sim -0.55$ eV.

The band dispersions were investigated by ARPES also for the two structures seen at $\sim (\pi, 0)$ as shown in Fig. 5.16. The results for the band mapping are summarized in Fig. 5.17, where the second derivatives of the ARPES

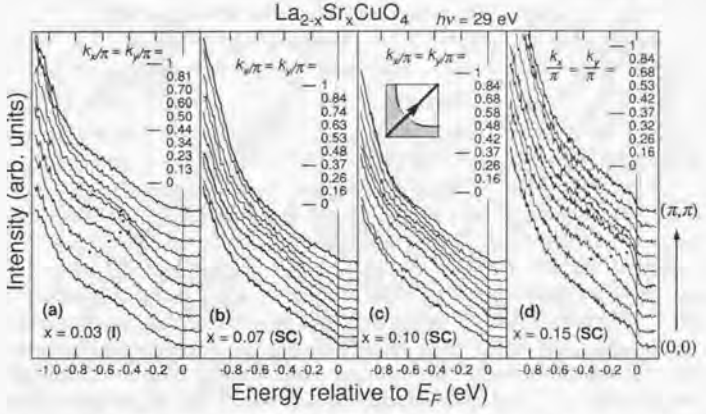


Figure 5.15: Doping dependence of ARPES spectra of $La_{2-x}Sr_xCuO_4$ along $(0,0) \rightarrow (\pi,\pi)$ for (a) $x = 0.03$, (b) $x = 0.07$, (c) $x = 0.10$ and (d) $x = 0.15$. While a broad feature dispersing across $E_F$ is identified for $x = 0.15$, the dispersive band is absent around $E_F$ for $x = 0.10$ and 0.07, even though the system is a superconductor. For $x = 0.03$, a band appears at $\sim -0.45$ eV around $(\pi/2, \pi/2)$.



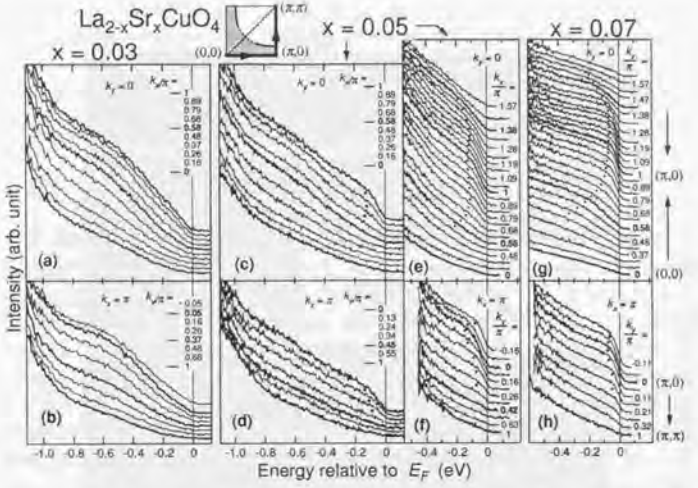


Figure 5.16: Momentum dependence of ARPES spectra of $La_{2-x}Sr_xCuO_4$ along $(0,0) \rightarrow (\pi,0)$ (upper panels) and $(\pi,0) \rightarrow (\pi,\pi)$ (lower panels) for $x = 0.03$ [(a) and (b)], $x = 0.05$ [(c), (d), (e) and (f)] and $x = 0.07$ [(g) and (h)].

spectra are plotted on the gray scale. Before differentiating, the spectrum at $(0,0)$, which is assumed to represent the angle-independent background, was subtracted from the ARPES spectra for each composition.

The dispersions of the band near $E_F$ are quite similar around $(\pi, 0)$ among $x = 0.15$, 0.10, 0.07 and 0.05: when one goes as $(0,0) \rightarrow (\pi,0) \rightarrow (\pi,\pi)$, the band approaches $E_F$ until $\sim (0.8\pi, 0)$, stays there until $(\pi, 0)$, then further approaches $E_F$ and goes above $E_F$ through the energy gap around $\sim (\pi, \pi/4)$. Therefore, this band should be responsible for the superconductivity. On the other hand, the dispersion of the broad feature seen around $-0.5$ eV for $x = 0.03$ and 0.05 is similar to the band dispersion of the undoped $CuO_2$ plane in $Sr_2CuO_2Cl_2$ [9-11] and $PrBa_2Cu_3O_7$ [115]. Along the $(0,0) \rightarrow (\pi,\pi)$ cut, the broad peak moves upwards, reaches a band maximum ($\sim -0.45$ eV) around $(\pi/2, \pi/2)$ and then disappears. The broad peak emerges in going from $(0,0)$ to $(\pi,0)$ and then disappears between $(\pi,0)$ and $(\pi,\pi)$. Therefore, the band around $-0.5$ eV is attributed to the lower Hubbard band (LHB) of the AFI.

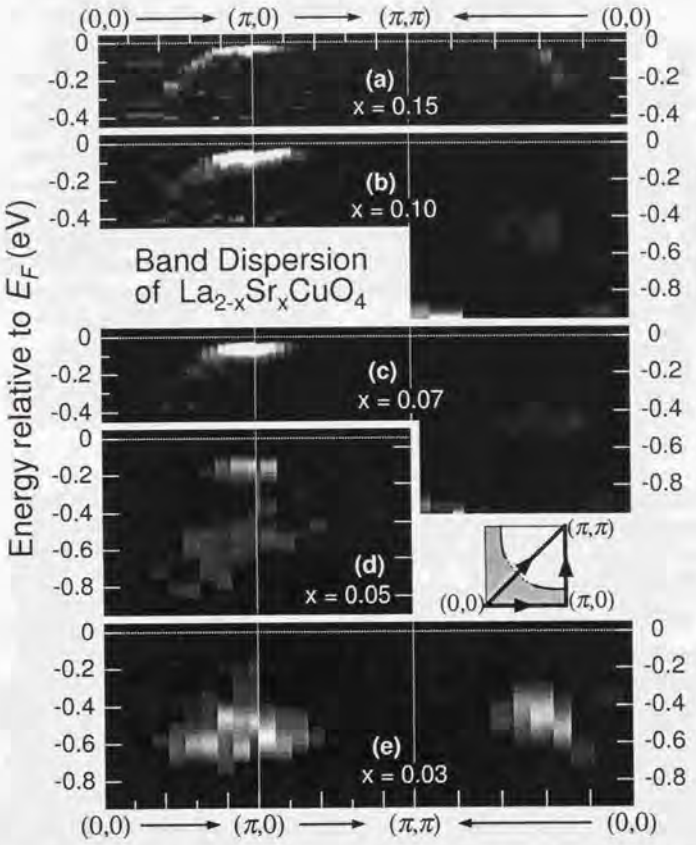


Figure 5.17: Band dispersions of $La_{2-x}Sr_xCuO_4$ ($x \leq 0.15$) derived from the ARPES spectra by taking the second derivatives after subtracting the spectrum at $(0,0)$, which is assumed to represent the angle-independent background. For $x = 0.05$, while the band around $-0.1$ eV evolves from the band near $E_F$ in the underdoped superconductor ($x = 0.10$ and 0.07), the band around $-0.5$ eV appears to evolve from the lower Hubbard band in the undoped insulator.



The energy difference between $(\pi, 0)$ and $(\pi/2, \pi/2)$ is smaller ($\sim$ 0.1 eV) in the insulating ($x = 0.03$) LSCO than that in $Sr_2CuO_2Cl_2$ ($\sim$ 0.3 eV). According to $t$-$t'$-$t''$-$J$ model calculations, the small energy difference results from small $t'$ and $t''$ values [11, 116]. Perhaps, the second and third nearest hoppings $t'$ and $t''$ may be affected by the presence of apical oxygens in LSCO.

### 5.4.2 Discussion

The ARPES spectra for $x = 0.05$ may be regarded as a superposition of the spectra of the SC and the AFI, as illustrated in Fig. 5.18. As shown in the lower panel of Fig. 5.19, while the spectra for $x = 0.05$ have two structures at $(\pi, 0)$, they have only one broad peak near $(\pi/2, \pi/2)$. This excludes extrinsic origins for the two components such as a partial charge-up of the sample. A possible origin for the coexistence of the two spectral features is a phase separation into hole-poor antiferromagnetic domains and hole-rich superconducting domains. Indeed, for $La_2CuO_{4+y}$ with excess oxygens, such a phase separation occurs macroscopically as revealed by, e.g., neutron diffraction [117, 118], but corresponding observation has never been reported for the Sr-doped LSCO system. A more likely interpretation is a microscopic inhomogeneity of the hole density in the sense that the doped holes are segregated in the boundaries of antiferromagnetic domains on the scale of several atomic distances [62]. Indeed, $\mu^+$SR [51] and $^{139}$La NQR [119] experiments have shown the presence of a local magnetic field in the so-called "spin-glass" phase (the upper panel of Fig. 5.19). Then, for the presented spectra taken above the "spin-glass" transition temperature, the splitting into the two structures would be due to dynamical fluctuations of such a microscopic phase separation. Furthermore, the microscopic phase separation may explain why the chemical potential is pinned against hole doping

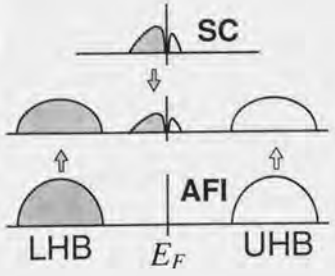


Figure 5.18: Schematic drawing indicating that the spectra for $x = 0.05$ may be derived from the band around $E_F$ in the superconductor (SC) and the lower Hubbard band (LHB) in the antiferromagnetic insulator (AFI).

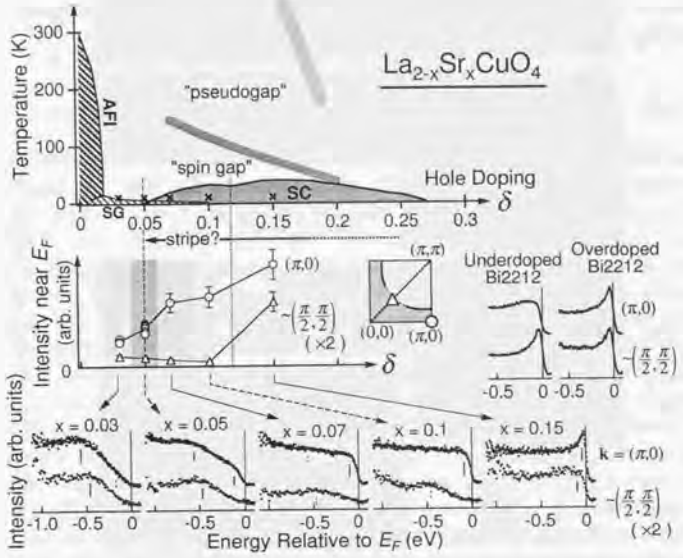


Figure 5.19: **Top:** Phase diagram of $La_{2-x}Sr_xCuO_4$ taken from Refs. 51 and 47 (SG: so-called spin-glass phase). Crosses denote measured points. **Middle:** Doping dependence of the integrated spectral intensity near $E_F$ ($E > -0.2$ eV) at $(\pi, 0)$ (open circles) and at $\sim (\pi/2, \pi/2)$ (open triangles, multiplied by 2). The intensity near $E_F$ is strongly suppressed at $\sim (\pi/2, \pi/2)$ compared to $(\pi, 0)$ for $0.05 \leq x \leq 0.10$. **Bottom:** Doping dependence of the spectral lineshape at $(\pi, 0)$ and at $\sim (\pi/2, \pi/2)$. From the ARPES spectra for each composition, the spectrum at $(0, 0)$ has been subtracted as the angle-independent background. The spectral intensity for $\sim (\pi/2, \pi/2)$ have been multiplied by 2. **Right:** Spectral lineshapes for $Bi_2Sr_2CaCu_2O_{8+y}$ (Bi2212) taken from Ref. 98, displayed on the same scale as the bottom panel. While the lineshapes at $(\pi, 0)$ are similar between $La_{2-x}Sr_xCuO_4$ and $Bi_2Sr_2CaCu_2O_{8+y}$, the lineshapes at $\sim (\pi/2, \pi/2)$ are quite different.



for $x \lesssim 0.15$ as revealed in Chapter 3. As for the underdoped Bi2212, two components split by $\sim 0.5$ eV have not been reported and spectral features seem to be shifted smoothly from the SC to the AFI [114].

The ARPES spectral lineshapes are compared between LSCO and Bi2212 [98] in Fig. 5.19. Whereas the lineshapes at $(\pi, 0)$ are similar irrespective of doping levels, the spectra near $(\pi/2, \pi/2)$ are quite different: while the peak near $E_F$ is sharp for both the overdoped and underdoped Bi2212, one finds no peak around $E_F$ for underdoped LSCO and a considerably broad peak for optimally doped LSCO. This difference is likely to be related with the dynamical stripe correlations [48, 49], which is particularly strong in LSCO as suggested by, e.g., inelastic neutron scattering (INS) studies (Fig. 2.11) [50, 61, 62]. Also for Bi2212 system, it has been reported that the sharp peak near $E_F$ is suppressed near $(\pi/2, \pi/2)$ upon Zn-doping [120], which is considered to induce stripe correlations [63]. The absence of the band crossing $E_F$ near $(\pi/2, \pi/2)$ may be reconciled with the vertically and horizontally oriented stripes in LSCO [50]. Intuitively, while the system may be metallic along the half-filled stripes, namely, in the $(0, 0) - (\pi, 0)$ or $(0, 0) - (0, \pi)$ direction, the low-energy excitation should be strongly suppressed in the directions crossing all the stripes such as the $(0, 0) - (\pi, \pi)$ direction.

The spectral intensity near $E_F$ ($E > -0.2$ eV) evolves differently between at $(\pi, 0)$ and near $(\pi/2, \pi/2)$, as shown in the middle panel of Fig. 5.19. Upon hole doping, the intensity at $(\pi, 0)$ grows in $x \gtrsim 0.05$, where the incommensurability of the spin fluctuations also arises according to the INS study [Fig. 2.11(b)] [60]. On the other hand, the intensity near $(\pi/2, \pi/2)$ remains suppressed with hole doping for the entire underdoped region ($0.05 \leq x \leq 0.10$). Hence, one may think that the segregated holes for $x \sim 0.05$ already start to be arranged vertically and horizontally. Therefore we propose that the hole-rich boundaries of the antiferromagnetic domains around the SIT continuously evolves into the stripe correlations in the underdoped SC. As hole doping reduces the distances between stripes compared to the coherence length, the transition to the superconductor may occur ($x \sim 0.05$), and the structure at $\sim 0.55$ eV is broadened to be a tail of the QP peak near $E_F$ for $x = 0.07$ and 0.1 probably because the size of the antiferromagnetic domains becomes so small.

In going from $x = 0.10$ to 0.15, the band crossing $E_F$ suddenly appears in the $(0, 0) - (\pi, \pi)$ direction, probably corresponding to the phenomenon that the incommensurability in INS saturates for $x \gtrsim 0.15$ [Fig. 2.11(b)] [60]. This may be understood that the doped holes in excess of $x = 1/8$ overflow the saturated stripes. Nevertheless, the peak near $(\pi/2, \pi/2)$ is still

broad and weak for $x \gtrsim 0.15$, implying that the effect of the dynamical stripe correlations persists to some extent in the optimally doped and overdoped LSCO.

## 5.5 Conclusion

To summerize the present ARPES results on LSCO, a schematic picture of the band structure of LSCO is drawn in Fig. 5.20, based on Figs. 5.9, 5.12 and 5.17. The present study on LSCO have shown that, when the $CuO_2$ plane is as heavily overdoped as $x = 0.3$, the Fermi surface changes its topology: the hole-like underlying Fermi surface centered at $(\pi, \pi)$ for $x \leq 0.15$ turns into the electron-like Fermi surface centered at $(0, 0)$ for $x = 0.3$. On the other hand, as the hole concentration $x$ decreases, the magnitude of superconducting gap $\Delta_{SC}$ monotonously increases and continuously evolves into the energy gap in the normal state $\Delta_{NG}$ near the SIT ($x = 0.05$), implying that these gaps have the same origin. The similarity between the doping dependences of the superconducting gap $\Delta_{SC}$ and the high-energy pseudogap $\Delta_{PG}$ suggests close relation between the superconductivity and the antiferromagnetic correlations. More studies are necessary to identify the anisotropy and temperature dependence of the superconducting as well as normal-state gaps for the LSCO system as in other cuprates [26-30, 32-35]. When $x$ decreases from the superconductor to the insulator, the spectral weight is rapidly transferred from the QP band responsible for superconductivity ($\sim -0.1$ eV) to the band at $\sim -0.5$ eV similar to the LHB in the AFI. The two features coexist in the spectra around the SIT ($x \sim 0.05$), suggesting that the LSCO system around the SIT has a microscopic homogeneity of the hole density. In the $(0, 0) - (\pi, \pi)$ direction, it appears as if the metal-insulator transition occurred between $x = 0.15$ and $x = 0.1$ in the sense that the QP band crossing $E_F$ near $(\pi/2, \pi/2)$ is absent in the underdoped LSCO ($x \leq 0.10$). The suppression of the QP band crossing $E_F$ near $(\pi/2, \pi/2)$ may be reconciled with the formation of the dynamical stripes. These observations have provided a new perspective of how the doped holes in the AFI evolve into the fluctuating stripes in the underdoped SC. The mechanism in which the SC-to-AFI transition occurs is the subject of strong theoretical interest [111, 121] and therefore should be addressed in further studies.



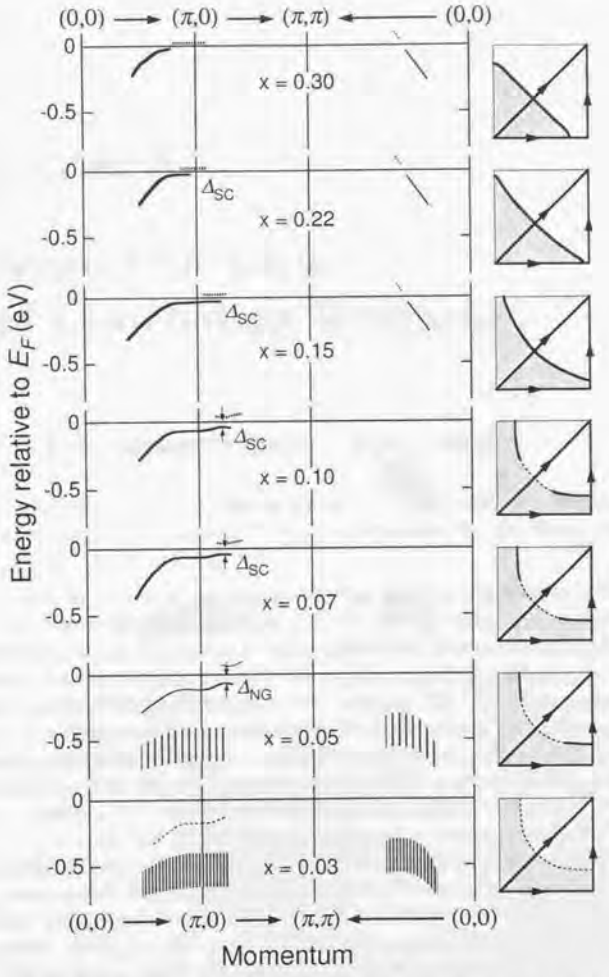


Figure 5.20: Schematic picture of the band structure of $La_{2-x}Sr_xCuO_4$ (left panels), based on the ARPES results (Figs. 5.12 and 5.17). The right panels show the Fermi surfaces deduced from the ARPES results, mainly taken from Fig. 5.9. $\Delta_{SC}$: superconducting gap. $\Delta_{NG}$: "normal-state gap."

# Chapter 6

# Perspective Views and Concluding Remarks

## 6.1 Two characteristic energy scales

From the PES results in Chapters 4 and 5, it turns out that the doping-dependent electronic structure of LSCO is dominated by two characteristic energy scales as shown in Fig. 6.1.

One is the energy of the superconducting gap $\Delta_{SC}$ observed by ARPES on the Fermi surface near $(\pi, 0)$ (Fig. 5.10), corresponding to the gaps observed by scanning tunnel spectroscopy (STS) [54], Raman scattering [110], inelastic neutron scattering (INS) [59] and the gap deduced from the electronic specific heat in the superconducting state [47]. The energy $\Delta_{SC}$ is likely to be scaled with the temperature $T^*$ above which the energy gap is closed, approximately as $2\Delta_{SC} \sim 4.3 k_B T^*$. In the overdoped region ($x \gtrsim 0.2$), $T^*$ coincides with the superconducting transition temperature $T_c$, yielding $2\Delta_{SC} \sim 4.3 k_B T_c$. In the optimally doped and underdoped regions ($x \lesssim 0.15$), the "normal-state gap" ("low-energy pseudogap" or "strong pseudogap") remains opened above $T_c$ and probably $T^*$ would agree with the temperature $T_{NG}$ above which the normal-state gap is closed in the ARPES spectra. The evidence of the normal-state gap in LSCO has been observed for $x = 0.05$ in the present study, but the measurement of $T_{NG}$ should be addressed in future ARPES studies on LSCO. Indeed, it has been also reported for LSCO that, below a temperature corresponding to $T^*$, the electrical resistivity $\rho(T)$ and the uniform magnetic susceptibility $\chi(T)$ deviate downward slightly from the linear-$T$ behavior in the same way as those for Bi2212 [54]. Somehow, the "spin-gap" behavior observed in the underdoped YBCO [38, 39]

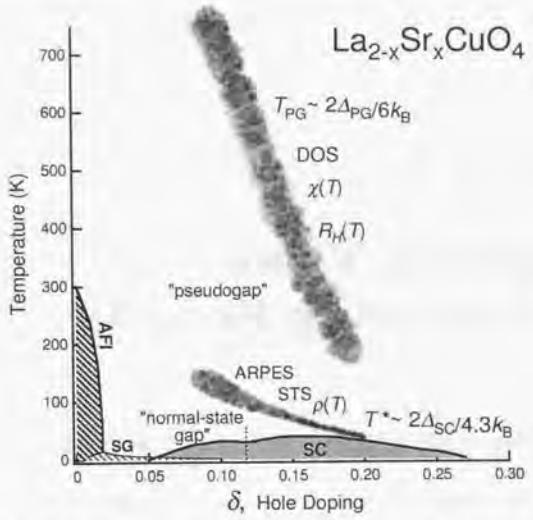


Figure 6.1: Two characteristic energy scales of $La_{2-x}Sr_xCuO_4$, empirically determined by the PES measurements and other various experiments.

is obscured for the underdoped LSCO in the NMR results [56]. As for the ARPES spectra, the energy gaps in the superconducting and normal states are quite similar as shown in Figs. 5.6(c), 5.7(b) and 5.8(b), suggesting that the normal-state gap has the same origin as the superconducting gap, e.g., preformed Cooper pairs, which lose their coherence above $T_c$ but still keep local pairing [92-95], and the spinon pairing which already occurs above $T_c$ [90].

The other energy scale is the pseudogap energy $\Delta_{PG}$ ("high-energy pseudogap" or "weak pseudogap") observed by AIPES in the underdoped LSCO. The spectral density of states is suppressed to some extent around the chemical potential $\mu$ in the energy scale $\Delta_{PG}$ much larger than $\Delta_{SC}$ (Fig. 4.3). The energy $\Delta_{PG}$ is scaled as $2\Delta_{PG} \sim 6k_BT_{PG}$ with the temperature $T_{PG}$ below which the underdoped LSCO shows pseudogap-like behaviors such as the reduction of the magnetic susceptibility $\chi$ [40], the enhancement of the Hall coefficient $R_H$ [40] and the acceleration in the decrease in the resistivity with deceasing temperature $d\rho/dT$ [42]. As discussed in Sec. 4.7, the high-energy pseudogap $\Delta_{PG}$ is likely originated from antiferromagnetic correlations.



Accordingly, we find that the strong electron correlation, which may be represented by the energy of the charge-transfer gap $\Delta_{CT}$ of the order of 1 eV, yields two doping-dependent lower energy scales, i.e., the pseudogap energy $\Delta_{PG}$ of the order of 100 meV and the energy of the superconducting gap $\Delta_{SC}$ of the order of 10 meV. Although the scales of $\Delta_{PG}$ and $\Delta_{SC}$ are different ($\Delta_{PG} \gg \Delta_{SC}$), these two energies increase in a similar way with decreasing $x$. This implies a close relation between the superconductivity and the antiferromagnetic correlations, even though the clarification of the microscopic mechanism remains to be made in the future.

## 6.2 Evolution of the electronic structure with hole doping

Finally, let us draw the picture of how the electronic structure evolves from the undoped antiferromagnetic insulator to the overdoped metal in the LSCO system, based on the PES results presented in the preceeding chapters. The evolution of the overall electronic structure is schematically illustrated in Fig. 6.2. The details of the momentum dispersions below $\mu$ have been already summarized in Fig. 5.20. Upon hole doping into the antiferromagnetic Mott insulator ($x = 0$), the chemical potential $\mu$ is pinned within the charge-transfer gap ($\Delta_{CT} \sim 1.5$ eV), and the spectral weight is transferred from the upper Hubbard band (UHB) and the Zhang-Rice singlet (ZRS) band [effective lower Hubbard band (LHB)] into the charge-transfer gap region below and above $\mu$, probably because the holes are segregated from the "microscopic AF domains." Here the momentum-integrated spectral weight around $\mu$ is suppressed in the energy scale of $\Delta_{PG}$ ("high-energy pseudogap" or "weak pseudogap") larger than $\Delta_{SC}$ ($\Delta_{SC} \ll \Delta_{PG} \ll \Delta_{CT}$) owing to the strong antiferromagnetic correlations. As more holes are doped, the size of the AF domains is reduced and accordingly the insulator with the vertical and horizontal domain walls evolves into the superconductor with the stripe correlations for $x > 0.05$. Because of the stripe correlations, the quasiparticle weight near $\mu$ in the $(0,0)-(\pi,\pi)$ direction is almost completely suppressed, even though the spectral weight is further transferred to near $\mu$ around $(\pi,0)$ in the underdoped region ($0.05 \lesssim x \lesssim 0.125$). Meanwhile, as the in-plane antiferromagnetic correlation length decreases with increasing $x$, the pseudogap $\Delta_{PG}$ is weakened in its width and depth. The stripes are saturated with a hole concentration $x = 1/8$ and the holes doped in excess of $x = 1/8$ overflow the stripes to contribute the recovery of the conventional two-dimensional electronic structure of the $CuO_2$ planes. With further hole

doping in the optimally and overdoped regions ($x \gtrsim 0.15$), the weight transfer is decelerated and thus the chemical potential start to be shifted as in a conventional metal. In the overdoped region ($x \gtrsim 0.2$), the pseudogap disappears and the usual metallic Fermi edge is observed in the AIPES spectra. When the $CuO_2$ plane is heavily overdoped ($x \gtrsim 0.22$), the flat band at $(\pi, 0)$ goes above $\mu$ and the topology of the Fermi surface turns from hole-like into electron-like. The superconducting transition temperature $T_c$ decreases and vanishes around $x \sim 0.27$.

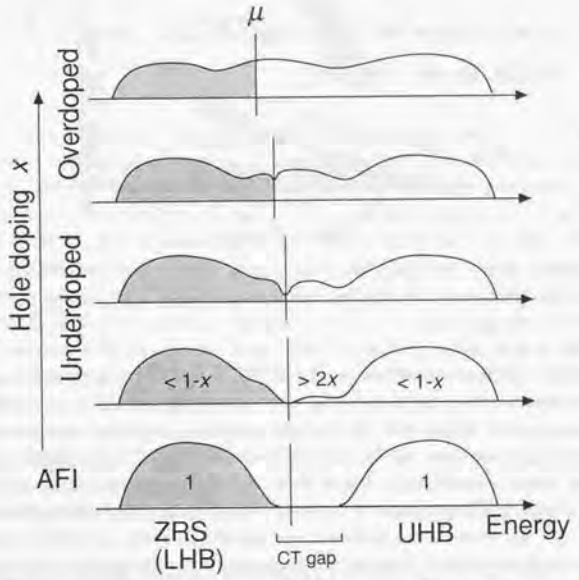


Figure 6.2: Schematic picture for the evolution of the electronic structure of $La_{2-x}Sr_xCuO_4$ with hole doping, based on the present PES experiments. With hole doping in the underdoped regime, the spectral weight is transferred into the charge-transfer (CT) gap region and the chemical potential ($\mu$) is pinned within the CT gap, while the spectral density of states around the chemical potential $\mu$ is suppressed on the energy scale of $\Delta_{PG}$ ("high-energy pseudogap" or "weak pseudogap"). For the simplicity, the superconducting gap is omitted in the picture.



## 6.3 Concluding remarks

The present photoemission study on LSCO has been fruitful, providing us much information which have not been obtained from other cuprates. For examples, the chemical potential shift with hole doping is unusually suppressed in the underdoped LSCO, the Fermi-surface topology turns from hole-like to electron-like between the optimally doped and heavily overdoped LSCO, and the spectral weight is transferred between the two components coexisting in the ARPES spectra around the superconductor-insulator transition. Perhaps, these novel observations may come from the availability of LSCO in a wide hole concentration range ($0 \leq x \leq 0.3$). Therefore, further PES studies on various kinds of cuprates are necessary to distinguish whether the above observations are specific to the LSCO system or universal to the $CuO_2$ planes in the cuprate superconductors. Also a clear difference between LSCO and Bi2212 has been found. The QP band is absent around $\mu$ in the $(0,0) - (\pi,\pi)$ direction for the underdoped LSCO. The high-energy pseudogap (weak pseudogap) in AIPES spectra is expected to be universal among the cuprate superconductors, but corresponding measurements are required for other cuprates.

Therefore, it is important to clarify what is common and what is different among the family of the cuprate systems. Indeed, many cuprate superconductors with various peculiarities have been synthesized so far. However, it seems that the previous PES and especially ARPES studies have been concentrated on a few representative systems. More kinds of cuprate superconductors should be studied in detail for the true understanding of the high-$T_c$ cuprate systems and for obtaining the cuprates with further higher critical temperatures.

# Acknowledgments

I would like to express my sincere gratitude to Prof. Atsushi Fujimori for guiding me to the exciting field of research, a lot of helpful advice, many enlightening discussions and continuous encouragement throughout my graduate days under his tight schedule. I would also like to express my thanks to Dr. Takashi Mizokawa for his great help and precious discussions.

I am very grateful to Prof. Zhi-Xun Shen for providing me invaluable opportunities and stimulative advice. I am particularly indebted to Dr. Changyoung Kim for valuable discussions, for his cooperation in the present ARPES work not only in the daytime but also at midnight and early in the morning, and for kindly helping me to enjoy my stay in Stanford.

I have to express my gratitude to Dr. Kenji Tamasaku, Mr. Masamitsu Takaba, Mr. Teruhisa Kakeshita, Dr. Hiroshi Eisaki and Prof. Shinichi Uchida for supplying high-quality crystals of $La_{2-x}Sr_xCuO_4$ used in the ARPES and XPS studies. In particular, I appreciate Dr. Eisaki's efforts in growing the crystals for the sake of the ARPES study. I have to express my gratitude to Mr. Takao Sasagawa, Dr. Tsuyoshi Kimura and Prof. Kouji Kishio for supplying high-quality crystals of $La_{2-x}Sr_xCuO_4$ used in AIPES and BIS studies.

It is my pleasure to express my thanks to Mr. Kensuke Kobayashi for his supports in the high-resolution AIPES experiments and a lot of encouraging advice for the five years. I would like to thank Dr. Motohiko Nakamura for his cooperation to the hard experiments in the ARPES work.

I would like to acknowledge Prof. Takami Tohyama, Prof. Sadamichi Maekawa, Prof. Masatoshi Imada and Prof. Kousaku Yamada for valuable discussions.

I would like to thank all the members of Shen-group, Dr. Paul J. White, Dr. Anne Y. Matsuura, Dr. Chul-Hong Park, Dr. Tschang-Uh Nahm, Dr. Jeffrey M. Harris, Dr. Mattias C. Schabel, Dr. Stuart L. Friedman, Dr. Anton V. Puchkov, Dr. Dong-Hui Lu, Dr. Huey-Chuen Kao, Mr. Md-Zahid Hasan,

Mr. N. Peter Armitage, Mr. Pavel Bogdanov, Mr. Dong-Lai Feng, Mr. Filip Ronning, Mr. Zheng-Yu Wang and Mrs. Marilyn Gordon for kindly helping with the ARPES measurements and my enjoyable stay in Stanford. I am grateful to the staffs of Stanford Synchrotron Radiation Laboratory (SSRL) for their friendly and kindly service.

This work is supported by a Grant-in-Aid for Scientific Research from the Ministry of Education, Science, Sports and Culture of Japan, the New Energy and Industrial Technology Development Organization (NEDO), Special Coordination Fund for Promoting Science and Technology from Science and Technology Agency of Japan, the U. S. DOE, Office of Basic Energy Science and Division of Material Science. Stanford Synchrotron Radiation Laboratory is operated by the U. S. DOE, Office of Basic Energy Sciences, Division of Chemical Sciences.

Finally, I would like to thank all the members of Fujimori-group, Dr. Keiji Morikawa, Dr. Tomohiko Saitoh, Dr. Kenya Shimada, Dr. Kazutoshi Mamiya, Dr. Akira Sekiyama, Dr. Takehisa Konishi, Dr. Oliver Rader, Mr. Jin-Young Son, Mr. Jun Okamoto, Mr. Tomofumi Susaki, Mr. Toshiyuki Tsujioka, Mr. Jobu Matsuno, Mr. Teppei Yoshida, Mr. Masahiko Satake, Mr. Jun Okabayashi, Mr. Kouzou Okazaki, Mr. Yoshisuke Ishikawa and Miss. Hazuki Wakazono for their support, encouragements, fruitful and fruitless discussions, which have pleased me for the five years.

January 1999

Akihiro Ino

# References

[1] J. G. Bednorz and K. A. Müller, Z. Phys. B **64**, 189 (1986).

[2] N. F. Mott, Proc. Phys. Soc. A **62**, 416 (1949).

[3] J. Hubbard, Proc. Roy. Soc. A **277**, 237 (1964).

[4] J. Hubbard, Proc. Roy. Soc. A **281**, 401 (1964).

[5] Y. Tokura, S. Koshihara, T. Arima, H. Takagi, S. Ishibashi, T. Ido, and S. Uchida, Phys. Rev. B **41**, 11657 (1990).

[6] S. Uchida, T. Ido, H. Takagi, T. Arima, Y. Tokura, and S. Tajima, Phys. Rev. B **43**, 7942 (1991).

[7] F. C. Zhang and T. M. Rice, Phys. Rev. B **37**, 3759 (1988).

[8] H. Eskes and G. A. Sawatzky, Phys. Rev. Lett. **61**, 1415 (1988).

[9] B. O. Wells, Z.-X. Shen, A. Matsuura, D. M. King, M. A. Kastner, M. Greven, and R. J. Birgeneau, Phys. Rev. Lett. **74**, 964 (1995).

[10] J. J. M. Pothuizen, R. Eder, N. T. Hien, M. Matoba, A. A. Menovsky, and G. A. Sawatzky, Phys. Rev. Lett. **78**, 717 (1997).

[11] C. Kim, P. J. White, Z.-X. Shen, T. Tohyama, Y. Shibata, S. Maekawa, B. O. Wells, Y. J. Kim, B. J. Birgeneau, and M. A. Kastner, Phys. Rev. Lett. **80**, 4245 (1998).

[12] Z.-X. Shen and D. S. Dessau, Phys. Rep. **253**, 1 (1995).

[13] Z.-X. Shen, W. E. Spicer, D. M. King, D. S. Dessau, and B. O. Wells, Science **267**, 343 (1995).

[14] C. G. Olson, R. Liu, D. W. Lynch, R. S. List, A. J. Arko, B. W. Veal, Y. C. Chang, P. Z. Jiang, and A. P. Paulikas, Phys. Rev. B **42**, 381 (1990).

[15] D. S. Dessau, Z.-X. Shen, D. M. King, D. S. Marshall, L. W. Lombardo, P. H. Dickinson, A. G. Loeser, J. DiCarlo, C.-H. Park, A. Kapitulnik, and W. E. Spicer, Phys. Rev. Lett. **71**, 2781 (1993).

[16] R. Liu, B. W. Veal, A. P. Paulikas, J. W. Downey, P. J. Kostić, S. Fleshler, U. Welp, C. G. Olson, X. Wu, A. J. Arko, and J. J. Joyce, Phys. Rev. B **46**, 11056 (1992).

[17] D. S. Marshall, D. S. Dessau, A. G. Loeser, C.-H. Park, A. Y. Matsuura, J. N. Eckstein, I. Bozovic, P. Fournier, A. Kapitulnik, W. E. Spicer, and Z.-X. Shen, Phys. Rev. Lett. **76**, 4841 (1996).

[18] H. Ding, A. F. Bellman, J. C. Campuzano, M. Randeria, M. R. Norman, T. Yokoya, T. Taakahashi, H. Katayama-Yoshida, T. Mochiku, K. Kadowaki, G. Jennings, and G. P. Brivio, Phys. Rev. Lett. **76**, 1533 (1996).

[19] D. M. King, Z.-X. Shen, D. S. Dessau, D. S. Marshall, C.-H. Park, W. E. Spicer, J. L. Peng, Z. Y. Li, and R. L. Greene, Phys. Rev. Lett. **73**, 3298 (1994).

[20] K. Gofron, J. C. Campuzano, A. A. Abrikosov, M. Lindroos, A. Bansil, H. Ding, D. Koelling, and B. Dabrowski, Phys. Rev. B **46**, 11056 (1992).

[21] M. C. Schabel, C.-H. Park, A. Matsuura, Z.-X. Shen, D. A. Bonn, R. Liang, and W. N. Hardy, Phys. Rev. B **57**, 6090 (1998).

[22] M. C. Schabel, C.-H. Park, A. Matsuura, Z.-X. Shen, D. A. Bonn, R. Liang, and W. N. Hardy, Phys. Rev. B **57**, 6107 (1998).

[23] D. M. King, Z.-X. Shen, D. S. Dessau, W. E. Spicer, A. J. Arko, D. S. Marshall, J. DiCarlo, A. G. Loeser, C.-H. Park, B. O. Wells, E. R. Ratner, J. L. Peng, Z. Y. Li, and R. L. Greene, Phys. Rev. Lett. **70**, 3159 (1993).

[24] H. Ding, M. R. Norman, T. Yokoya, T. Takeuchi, M. Randeria, J. C. Campuzano, T. Taakahashi, T. Mochiku, and K. Kadowaki, Phys. Rev. Lett. **78**, 2628 (1997).

[25] R. O. Anderson, R. Claessen, J. W. Allen C. G. Olson, C. Janowitz, L. Z. Liu, J.-H. Park, M. B. Maple, Y. Dalichaouch, M. C. de Andrade, R. F. Jardim, E. A. Early, S.-J. Oh, and W. P. Ellis, Phys. Rev. Lett. **70**, 3163 (1993).



[26] Z.-X. Shen, D. S. Dessau, B. O. Wells, D. M. King, W. E. Spicer, A. J. Arko, D. Marshall, L. W. Lombardo, A. Kapitulnik, P. Dickinson, S. Doniach, J. DiCarlo, A. G. Loeser, and C. H. Park, Phys. Rev. Lett. **70**, 1553 (1993).

[27] H. Ding, M. R. Norman, J. C. Campuzano, M. Randeria, A. F. Bellman, T. Yokoya, T. Takahashi, T. Mochiku, and K. Kadowaki, Phys. Rev. B **54**, R9678 (1996).

[28] T. Yokoya, T. Takahashi, T. Mochiku, and K. Kadowaki, Phys. Rev. B **53**, 14055 (1996).

[29] A. G. Loeser, Z.-X. Shen, D. S. Dessau, D. S. Marshall, C.-H. Park, P. Fournier, and A. Kapitulnik, Science **273**, 325 (1996).

[30] J. M. Harris, Z.-X. Shen, P. J. White, D. S. Marshall, M. C. Schabel, J. N. Eckstein, and I. Bozovic, Phys. Rev. B **54**, 15665 (1996).

[31] P. J. White, Z.-X. Shen, C. Kim, J. M. Harris, A. G. Loeser, P. Fournier, and A. Kapitulnik, Phys. Rev. B **54**, R15669 (1996).

[32] H. Ding, T. Yokoya, J. C. Campuzano, T. Takahashi, M. Randeria, M. R. Norman, T. Mochiku, K. Kadowaki, and J. Giapintzakis, Nature **382**, 51 (1996).

[33] M. R. Norman, H. Ding, M. Randeria, J. C. Campuzano, T. Yokoya, T. Takeuchi, T. Takahashi, T. Mochiku, and K. Kadowaki, Phys. Rev. B **54**, R9678 (1996).

[34] J. M. Harris, P. J. White, Z.-X. Shen, H. Ikeda, R. Yoshizaki, H. Eisaki, S. Uchida, W. D. Si, J. W. Xiong, Z.-X. Zhao, and D. S. Dessau, Phys. Rev. Lett. **79**, 143 (1997).

[35] M. C. Schabel, C.-H. Park, A. Matsuura, Z.-X. Shen, D. A. Bonn, R. Liang, and W. N. Hardy, Phys. Rev. B **55**, 2796 (1997).

[36] M. A. van Veenendaal, G. A. Sawatzky, and W. A. Groen, Phys. Rev. B **49**, 1407 (1994).

[37] J. W. Allen, C. G. Olson, M. B. Maple, J.-S. Kang, L. Z. Liu, J.-H. Park, R. O. Anderson, W. P. Ellis, J. T. Markert, Y. Dalichaouch, and R. Liu, Phys. Rev. Lett. **64**, 595 (1990).

[38] H. Yasuoka, T. Imai, and T. Shimizu, in *Strong Correlation and Superconductivity*, edited by H. Fukuyama, S. Maekawa, and A. P. Malozemof (Springer-Verlag, Berlin, 1989), p. 254.

[39] M. Takigawa, A. P. Reyes, P. C. Hammel, J. D. Thompson, R. H. Heffner, Z. Fisk, and K. C. Ott, Phys. Rev. B **43**, 247 (1991).

[40] T. Nakano, M. Oda, C. Manabe, N. Momono, Y. Miura, and M. Ido, Phys. Rev. B **49**, 16000 (1994).

[41] J. W. Loram, K. A. Mirza, J. M. Wade, J. R. Cooper, and W. Y. Liang, Physica C **235**, 134 (1994).

[42] H. Y. Hwang, B. Batlogg, H. Takagi, H. L. Kao, R. J. Cava, J. J. Krajewski, and W. F. Peck, Jr., Phys. Rev. Lett. **72**, 2636 (1994).

[43] T. Nishikawa, J. Takeda, and M. Sato, J. Phys. Soc. Jpn. **63**, 1441 (1994).

[44] H. Takagi, B. Batlogg, H. L. Kao, J. Kwo, R. J. Cava, J. J. Krajewski, and W. F. Peck, Jr., Phys. Rev. Lett. **69**, 2975 (1992).

[45] J. W. Loram, K. A. Mirza, W. Y. Liang, and J. Osborne, Physica C **162-164**, 498 (1989).

[46] T. Nishikawa, S. Shamoto, M. Sera, M. Sato, S. Ohsugi, Y. Kitaoka, and K. Asayama, Physica C **209**, 553 (1993).

[47] N. Momono, M. Ido, T. Nakano, M. Oda, Y. Okajima, and K. Yamaya, Physica C **233**, 395 (1994).

[48] J. Zaanen and A. M. Oleś, Ann. Physik **5**, 224 (1996).

[49] M. I. Salkola, V. J. Emery, and S. A. Kivelson, Phys. Rev. Lett. **77**, 155 (1996).

[50] J. M. Tranquada, B. J. Sternlieb, J. D. Axe, Y Nakamura, and S. Uchida, Nature **375**, 561 (1995).

[51] Ch. Niedermayer, C. Bernhard, T. Blasius, A. Golnik, A. Moodenbaugh, and J. I. Budnick, Phys. Rev. Lett. **80**, 3843 (1998).

[52] R. S. Markiewicz, J. Phys. Chem. Solids. **58**, 1179 (1997).

[53] R. Yoshizaki, N. Ishikawa, H. Sawada, E. Kita, and A. Tasaki, Physica C **166**, 417 (1990).

[54] T. Nakano, N. Momono, M. Oda, and M. Ido, J. Phys. Soc. Jpn. **67**, 2622 (1998).



[55] H. Yasuoka, S. Kambe, Y. Itoh, and T. Machi, Physica B **199&200**, 278 (1994).

[56] S. Fujiyama, Y. Itoh, H. Yasuoka, and Y. Ueda, J. Phys. Soc. Jpn. **66**, 2864 (1997).

[57] A. R. Moodenbaugh, Y. Xu, M. Suenaga, T. J. Folkerts, and R. N. Shelton, Phys. Rev. B **38**, 4596 (1988).

[58] M. K. Crawford, R. L. Harlow, E. M. McCarron, W. E. Farneth, J. D. Axe, H. Chou, and Q. Huang, Phys. Rev. B **44**, 7749 (1991).

[59] K. Yamada, S. Wakimoto, G. Shirane, C. H. Lee, M. A. Kastner, S. Hosoya, M. Greven, Y. Endoh, and R. J. Birgeneau, Phys. Rev. Lett. **75**, 1626 (1995).

[60] K. Yamada, C. H. Lee, K. Kurahashi, J. Wada, S. Wakimoto, S. Ueki, H. Kimura, Y. Endoh, S. Hosoya, G. Shirane, R. G. Birgeneau, M. Greven, M. A. Kastner, and Y. J. Kim, Phys. Rev. B **57**, 6165 (1998).

[61] A. Bianconi, N. L. Saini, A. Lanzara, M. Missori, T. Rossetti, H. Oyanagi, H. Yamaguchi, K. Oka, and T. Ito, Phys. Rev. Lett. **76**, 3412 (1996).

[62] S. R. White and D. J. Scalapino, Phys. Rev. Lett. **81**, 3227 (1998).

[63] M. Akoshima, T. Noji, Y. Ono, and T. Koike, Phys. Rev. B **57**, 7491 (1998).

[64] Y. Tokura, Y. Taguchi, Y. Okada, Y. Fujishima, T. Arima, K. Kumagai, and Y. Iye, Phys. Rev. Lett. **70**, 2126 (1993).

[65] K. Kumagai, T. Suzuki, Y. Taguchi, Y. Okada, Y. Fujishima, and Y. Tokura, Phys. Rev. B **48**, 7636 (1993).

[66] X. Y. Zhang, M. J. Rozenberg, and G. Kotliar, Phys. Rev. Lett. **70**, 1666 (1993).

[67] N. Furukawa and M. Imada, J. Phys. Soc. Jpn. **62**, 2557 (1993).

[68] M. A. van Veenendaal, R. Schlatmann, G. A. Sawatzky, and W. A. Groen, Phys. Rev. B **47**, 446 (1993).

[69] Z.-X. Shen, D. S. Dessau, B. O. Wells, C. G. Olson, D. B. Mitzi, L. Lombado, R. S. List, and A. J. Arko, Phys. Rev. B **44**, 12098 (1991).

[70] Y. Nakamura and S. Uchida, Phys. Rev. B **47**, 8369 (1993).

[71] S. Uchida, K. Tamasaku, and S. Tajima, Phys. Rev. B **53**, 14558 (1996).

[72] K. Tamasaku, Y. Nakamura, and S. Uchida, Phys. Rev. Lett. **69**, 1455 (1992).

[73] T. Kimura, K. Kishio, T. Kobayashi, Y. Nakayama, N. Motohira, K. Kitazawa, and K. Yamafuuji, Physica C **192**, 247 (1992).

[74] T. Sasagawa, K. Kishio, Y. Togawa, J. Shimoyama, and K. Kitazawa, Phys. Rev. Lett. **80**, 4297 (1998).

[75] C. Y. Chen, J. Birgeneau B, M. A. Kastner, N. W. Preyer, and T. Thio, Phys. Rev. B **43**, 392 (1991).

[76] K. Morikawa, T. Mizokawa, A. Fujimori, Y. Taguchi, and Y. Tokura, Phys. Rev. B **54**, 8446 (1996).

[77] K. Mizokawa, K. Ootomo, T. Konishi, A. Fujimori, Z. Hiroi, N. Kobayashi, and M. Takano, Phys. Rev. B **55**, R13373 (1997).

[78] A. Ino, Master's thesis, University of Tokyo, 1996.

[79] S. Hüfner, in *Photoelectron Spectroscopy* (Springer-Verlag, Berlin, 1995), Chap. 2, p. 35.

[80] V. Voronin, A. Mirmelstein, V. Kozhevnikov, and B. Goshchitskii, Physica C **218**, 407 (1993).

[81] M. Braden, P. Schweiss, G. Heger, W. Reichardt, Z. Fisk, K. Gamayunov, I. Tanaka, and H. Kojima, Physica C **223**, 396 (1994).

[82] G. K. Wertheim and P. H. Citrin, in *Photoemission in Solids I*, edited by M. Cardona and L. Ley (Springer-Verlag, Berlin, 1978), Chap. 5, p. 197.

[83] N. Furukawa and M. Imada, J. Phys. Soc. Jpn. **61**, 3331 (1992).

[84] L. F. Mattheiss, Phys. Rev. Lett. **58**, 1028 (1987).

[85] D. S. Greywall, Phys. Rev. B **27**, 2747 (1983).

[86] E. Dagotto, A. Moreo, F. Ortolani, J. Riera, and D. J. Scalapino, Phys. Rev. Lett. **67**, 1918 (1991).

[87] D. Vollhardt, Rev. Mod. Phys. **56**, 99 (1984).



[88] A. George and W. Krauth, Phys. Rev. Lett. **69**, 1240 (1992).

[89] C. Y. Chen, N. W. Preyer, P. J. Picone, M. A. Kastner, H. P. Jenssen, D. R. Gabbe, A. Cassanho, and R. J. Birgeneau, Phys. Rev. Lett. **63**, 2307 (1989).

[90] T. Tanamoto, H. Kohno, and H. Fukuyama, J. Phys. Soc. Jpn. **61**, 1886 (1992).

[91] J. J. Deisz, D. W. Hess, and J. W. Serene, Phys. Rev. Lett. **76**, 1312 (1996).

[92] V. J. Emery and S. A. Kivelson, Nature (London) **374**, 434 (1995).

[93] S. Doniach and M. Inui, Phys. Rev. B **41**, 6668 (1990).

[94] N. Trivedi and M. Randeria, Phys. Rev. Lett. **75**, 312 (1995).

[95] M. Imada, J. Phys. Soc. Jpn. **62**, 1105 (1993).

[96] C. T. Chen, F. Sette, Y. Ma, M. S. Hybertsen, E. B. Stechel, W. M. C. Foulkes, M. Schlutter, S-W. Cheong, A. S. Cooper, L. W. Rupp, Jr, B. Batllogg, Y. L. Soo, Z. H. Ming, A. Krol, and Y. H. Kao, Phys. Rev. Lett. **66**, 104 (1990).

[97] H. Eskes, A. M. Oleś, M. B. J. Meinders, and W. Stephan, Phys. Rev. B **50**, 17980 (1994).

[98] Z.-X. Shen and J. R. Schrieffer, Phys. Rev. Lett. **78**, 1771 (1997).

[99] D. Duffy, A. Nazarenko, S. Haas, A. Moreo, J. Riera, and E. Dagotto, Phys. Rev. B **56**, 5597 (1997).

[100] J. Jaklič and P. Prelovšek, Phys. Rev. B **52**, 6903 (1995).

[101] M. Imada, J. Phys. Soc. Jpn. **64**, 2954 (1995).

[102] J. R. Schrieffer and A. P. Kampf, J. Phys. Chem. Solids **56**, 1673 (1995).

[103] J. Schmalian, D. Pines, and B. Stojkovic, Phys. Rev. Lett. **80**, 3839 (1998).

[104] R. Preuss, W. Hanke, C. Gröber, and H. G. Evertz, Phys. Rev. Lett. **79**, 1122 (1997).

[105] J. C. Campuzano, H. Ding, M. R. Norman, M. Randeria, A. F. Bellman, T. Yokoya, T. Takahashi, H. Katayama-Yoshida, T. Mochiku, and K. Kadowaki, Phys. Rev. B **53**, 14737 (1996).

[106] K. Tamasaku, T. Ito, H. Takagi, and S. Uchida, Phys. Rev. Lett. **72**, 3088 (1994).

[107] S. Uchida, H. Takagi, Y. Tokura, N. Koshihara, and T. Arima, in *Strong Correlation and Superconductivity*, edited by H. Fukuyama, S. Maekawa, and A. P. Malozemof (Springer-Verlag, Berlin, 1989), p. 194.

[108] W. E. Pickett, Rev. Mod. Phys. **61**, 433 (1989).

[109] H. Won and K. Maki, Phys. Rev. B **49**, 1397 (1994).

[110] X. K. Chen, J. C. Irwin, H. J. Trodahl, T. Kimura, and K. Kishio, Phys. Rev. Lett. **73**, 3290 (1994).

[111] S.-C. Zhang, Science **275**, 1089 (1997).

[112] H. L. Kao, J. Kwo, H. Takagi, and B. Batlogg, Phys. Rev. B **48**, 9925 (1993).

[113] C. T. Chen, L. H. Tjeng, J. Kwo, H. L. Kao, P. Rudolf, F. Sette, and R. M. Fleming, Phys. Rev. Lett. **68**, 2543 (1992).

[114] R. B. Laughlin, Phys. Rev. Lett. **79**, 1726 (1997).

[115] T. Mizokawa, C. Kim, Z.-X. Shen, A. Ino, A. Fujimori, M. Goto, H. Eisaki, S. Uchida, M. Tagami, K. Yoshida, A. I. Rykov, Y. Siobara, and S. Tajima (unpublished).

[116] V. I. Belinicher, A. L. Chernyshev, and V. A. Shubin, Phys. Rev. B **54**, 14914 (1998).

[117] P. G. Radaelli, J. D. Jorgensen, R. Kleb, B. A. Hunter, F. C. Chou, and D. C. Johnston, Phys. Rev. B **49**, 6239 (1994).

[118] J. D. Jorgensen, B. Dabrowski, S. Pei, D. G. Hinks, L. Soderholm, B. Morosin, J. E. Schirber, E. L. Venturini, and D. S. Ginley, Phys. Rev. B **38**, 11337 (1988).

[119] J. H. Cho, F. Borsa, D. C. Johnston, and D. R. Torgeson, Phys. Rev. B **46**, 3179 (1992).



[120] P. J. White, Z.-X. Shen, D. L. Feng, C. Kim, Md-Zahid Hasan, J. M. Harris A. G. Loeser, H. Ikeda, R. Yoshizaki, G. D. Gu, and N. Koshizuka (unpublished).

[121] F. F. Assaad, M. Imada, and D. J. Scalapino, Phys. Rev. Lett. **77**, 4592 (1996).

Rosemarie Trockel